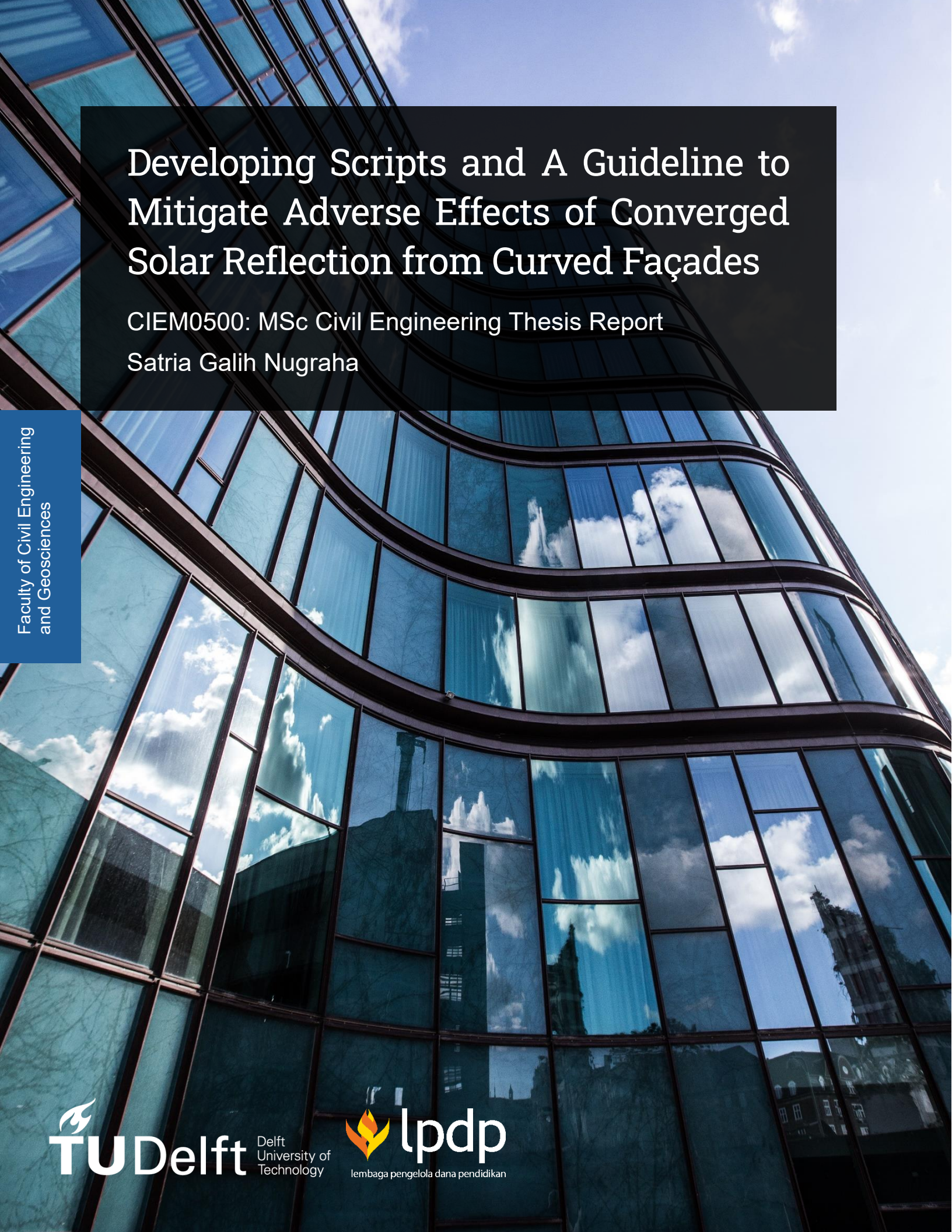

Developing Scripts and A Guideline to Mitigate Adverse Effects of Converged Solar Reflection from Curved Façades

CIEM0500: MSc Civil Engineering Thesis Report

Satria Galih Nugraha

Faculty of Civil Engineering and Geosciences

TU Delft Delft University of Technology

lpdp lembaga pengelola dana pendidikan

Developing Scripts and A Guideline to Mitigate Adverse Effects of Converged Solar Reflection from Curved Façades

Thesis Report

by

Satria Galih Nugraha

5740371

As partial fulfilment of the requirements to obtain the degree of

Master of Science in Civil Engineering

at Delft University of Technology

to be defended publicly on 8 August 2024

Thesis committee	:	Dr.ir. H.R. (Roel) Schipper
		Dr. E. (Eleonora) Brembilla
		Dr. M.A. (Mariana) Popescu
Project duration	:	February, 2024 – July, 2024
Faculty	:	Civil Engineering and Geosciences

An electronic version of this thesis is available at: https://repository.tudelft.nl/

Front cover: Freepik

Preface

All praise is due to God, who has granted me the opportunity and strength to achieve my dream of obtaining a master's degree from one of the best universities in the world for studying Civil Engineering: Delft University of Technology.

After 8,610 hours (187.5 + 120 ECTS) of studying Civil Engineering over 5 years, 11 months, and 24 days, I am honored to hold the title of "Ingenieur." The journey was challenging, especially at the beginning when I first started my master's degree at TU Delft. Learning the hard way about the significant gap between the Indonesian education system and Dutch education standards was a humbling experience. Yet, I persevered through what I often describe to my family and friends as "opening the unexplored wilderness (of science)" or, in Javanese, "Mbabat alas." This journey was particularly significant as I am the first in my family to pursue a master's degree, and doing so in the Netherlands was a monumental step.

First and foremost, I would like to thank my family who has been supporting me, believing in me, and praying for me day and night, even though we're 11,711 km apart. Thank you for not getting tired of listening to my complaints for the full 2 years, even though at the same time I was unwilling to go home because I had to study every day.

I would like to express my profound gratitude to all committee members: Dr. ir. Roel Schipper, Dr. Eleonora Brembilla, and Dr. Mariana Popescu, whose invaluable guidance and feedback were crucial in completing my master's thesis. My deepest thanks go to my Graduation Chair, Dr. ir. Roel Schipper, who has guided me from the very beginning, providing valuable counsel and direction for my thesis. He was the first person I approached for a master's thesis topic, and even though I did not stick with the initial topic he suggested, he graciously provided another (I hope this did not trouble him too much back then), which eventually led to the completion of this thesis.

I am also deeply grateful to Dr. Eleonora Brembilla, whose expertise in building physics and her lectures on daylight design sparked my curiosity and led me to pursue a master's thesis in an area I had not anticipated as a Structural Engineer. I extend my heartfelt thanks to Dr. Mariana Popescu, whose creativity and detailed, perceptive feedback, starting very early from her "Parametric Design and Digital Fabrication" lectures as well as within this thesis, profoundly influenced my work.

Lastly, I would like to express many thanks to the Ministry of Finance of the Republic of Indonesia, which has granted me the Indonesia Endowment Fund for Education (LPDP) scholarship, covering 100% of my expenses from day one of my master's degree to the very day I return to Indonesia. Without your financial help, I would have never been able to realize my dream.

Satria Galih Nugraha

Delft, August 2024

Abstract

Converged solar reflection resulting from the curved façades of mid-rise and high-rise buildings has proven to be a uniquely dangerous phenomenon, yet increasingly common. The "death ray" incident at 20 Fenchurch St (the "Walkie Talkie" Building) in London in 2013 was mirrored by a similar occurrence at the Amsterdam University Medical Center (AMC) in 2021, where parts of a car melted from the intense heat produced. This reoccurrence raises a fundamental question as to why this problem keep happening. Several factors may contribute: past studies focused on isolated instances, many building engineers and architects are unaware of the risks, and numerical reproduction of this phenomenon involves numerous parameters and complex scripting.

This thesis aims to provide an algorithm to accurately reconstruct the converged solar reflection phenomenon numerically by analyzing various input parameters, such as the geometry of a façade, the nonlinear reflection rate of glass panels, and the effect of anisotropic sky models. To ensure the validity of the model, on-site solar irradiance measurements were conducted in the parking lot of the AMC building. Additionally, the program was used to reenact the phenomenon at the Walkie Talkie building before improvements to its façade.

Results indicate that the three-dimensional problem can initially be approached with a two-dimensional model using horizontal cross-sections of the façade. The angles at which the most intense focal points occur in both the 3D and 2D models of the AMC building correspond to each other, at 15.24 and 23.04 degrees from the optical axis of the façade (solar azimuth angles of 147.34 and 139.54 degrees from the north). The study also concludes that under the same conditions, replacing a quarter-circle-shaped curved façade with a parabolic-shaped curved façade would significantly worsen the effect, potentially leading to five times higher converged solar reflection on the ground.

In the case of the AMC building, the highest recorded irradiance during measurement was 4834 W/m^2. This value differed by only 13.45% from the 3D model using the Reindl sky model, which showed 4184 W/m^2. Conversely, the conventional isotropic sky model produced a larger difference of 23.68%. For the 20 Fenchurch St building, the Reindl sky model also produced more intense results compared to the isotropic model, with the focal point intensity reaching up to 6271 W/m^2 on August 29, 2013. However, limited access to accurate three-dimensional models and details of the surrounding area may have affected the results.

The study also examined the systematic error due to mismatched curvature of the glass panels with the building's curvature. This mismatch caused irradiance variations, increasing by up to 23.52% at one time and decreasing by 13.09% at another, indicating no constant increase or decrease on the intensity of the focal point.

In conclusion, this thesis successfully captures various variable inputs to recreate an accurate converged solar reflection phenomenon in both the AMC and the "Walkie Talkie" buildings. It integrates these variables into one continuous script without the need to switch between different software, providing a comprehensive tool for assessing and mitigating this dangerous architectural flaw.

Keywords: converged solar reflection, the death ray, grasshopper scripting, solar irradiance, concave façade

Table of Contents

Table of Figures

List of Tables

Nomenclature

Abbreviation	Definition
BHI	Beam horizontal irradiance
DHI	Diffuse horizontal irradiance
REF	Reflected ground irradiance
BNI	Beam normal irradiance
GHI	Global horizontal irradiance
GTI	Global tilted irradiance

Abbreviation	Definition
DOY	Day of the year
TMY	Typical Meteorological Year
DMS	Degree, Minutes, Seconds
DD	Decimal Degrees
HOY	Hour of the year
DOY	Day of the year

Symbols	Definition	Unit
δ	Solar declination	[°]
N	Day of the year	[Day]
h	Solar height	[°]
φ	Latitude, angle of rotated surface	[°]
u	Hour angle	[°]
t	Hour	[Hours]
β	Slope angle from horizontal	[°]
F'	Clearness index	-
ρ	Reflection	[%]
α	Absorption	[%]
τ	Transmission	[%]
R_{eff}	Effective reflectance rate	-
R_s	Reflectance for s-polarized light	-
R_p	Reflectance for p-polarized light	-
n	refractive index	-
κ	Curvature	[1/m]
R	Radius	[m]
$\boldsymbol{N}$	Normal vector	-
G_t	Total radiation on a tilted plane	W/m^2
R_B	Beam radiation tilt factor	-
θ	Angle of incidence	[°]
G_B	Beam radiation on a horizontal surface	W/m^2
ρ_G	Specular reflectivity of the ground surface	-
G_{on}	Extraterrestrial radiation measured on a normal surface	W/m^2
G_{sc}	Solar constant	W/m^2
f	Focal point location from vertex	m
A	Anisotropy index	-

1 | Introduction

This chapter outlines the research motivation and the issues addressed in the thesis, which leads to the development of research questions. Additionally, it explains the research approach used to answer these questions.

1.1. Research context

In many large cities, large and tall buildings have become the norm for efficient land use and iconic city landmarks. Oftentimes, architects and engineers are eager to create irregularly shaped buildings to fulfil clients' desires, comply with regional constraints and regulations, meet other specific purposes, or simply to boast their prowess. One prominent feature in high-rise or mid-rise buildings is the presence of curved façades. Curved façades come in various sizes, shapes and made of different types of materials, such as polished metals, curved glass, or even planar glass arranged in a way that creates discretized curve shapes altogether.

In modern buildings, glass façades have become increasingly common. When installed correctly, glass can effectively provide natural light and views outside and help regulate temperatures indoors. However, even highly transparent glass can reflect light under specific conditions. Furthermore, these curved reflective façades, especially when concave, can pose a problem under direct solar radiation in some situations, as their shape enables these façades to concentrate the heat emitted by the sun and create focal points or lines with considerably higher temperatures than the surrounding areas.

One of the most well-known cases in which a curved building caused such a problem is the “Walkie Talkie” skyscraper on Fenchurch Street in Central London, where the 38-story building could melt cars, fry bike seats, scorch sidewalks, and ruin whole shelves of products in stores in the vicinity (Wainwright, 2013).

Figure 1.1 The reflected solar radiation from the 20 Fenchurch St (Ravenscroft, 2013)

Other than the case of the Walkie Talkie building, similar instances of converged solar reflection have occurred worldwide, such as at the Walt Disney Concert Hall and the Vdara Hotel in Los Angeles. The closest instance of this converged solar reflection phenomenon in the Netherlands occurred at the Amsterdam University Medical Center (Amsterdam UMC) building, where an incident in 2021 resulted in parts of a parked car melting from the intense heat.

In this thesis, on-site measurements of the converged solar reflection are conducted during the times when this effect intensifies. These measurements are used to calibrate and validate the numerical model against the real occurrence of converged solar reflection.

1.2. Research Problem

Over time, research involving various case studies has been undertaken to assess and mitigate the impact of converged solar reflection resulting from reflective curved façades. However, these studies are not extensive and are based on isolated instances, describing specific issues observed in particular cases. Additionally, the available package in Rhino software for modeling this problem requires extensive scripting capabilities from the user. Consequently, even if architects and consultants are aware of the potential problem, which is not always the case, they might still be reluctant to model the converged solar reflection phenomenon due to the complexity involved. This has led to the issue being insufficiently acknowledged and comprehensively understood within the building industry.

Wen et al. specifically examined the repercussions of glare from a highly reflective concave curved stainless-steel façade on a 9-story building in Singapore, focusing on its thermal and visual effects in tropical climates (Wen et al., 2020). Similarly, Danks et al. delved into current regulations and measurements regarding how visible light and heat affect both individuals and properties. Their work led to the development of quantitative criteria for assessing reflected sunlight from building facades, emphasizing visible glare and thermal impact. However, their analysis and schematization of the curved façade were confined to a singular model, and they noted that the non-linear reflectance rate of the glass façade worsens the effect of solar reflection (Danks et al., 2016a). They also found that the circumsolar effect from the sky plays a role in the underestimation of their outputs.

Speroni et al. conducted a sophisticated experimental assessment of solar radiation reflection from tall building façades at pedestrian levels. Their method involved fabricating three 1:100 scaled prototypes using various shapes and finishing materials. However, while their findings were extensive, they did not provide specific quantitative standards applicable to architects and engineers (Speroni et al., 2022).

Schipper and Brembilla also developed a parametric reconstruction of the solar convergence phenomenon of the Amsterdam UMC building using Rhino-Grasshopper along with the Radiance package. They found that the geometry of the façade, off which the solar rays bounce, significantly influences the intensity of the solar radiation. However, they do not draw a conclusion as to how different shapes will alter the creation of focal points (H. R. Schipper & Brembilla, 2023)

Until the last quarter of 2023, the regulations and design guidelines to avoid serious problem of solar convergence issue stemming from curved glass or reflective façades remained notably inadequate.

For example, some of the existing regulations indirectly related to the problem exist within British Standard PD7974-4 2003 but more focused on fire safety aspect within the design of buildings, and USA Federal Aviation Administration (FAA) Interim Policy but more focused on the matter regarding the risk of visual glare distracting pilots and ATC personnel within federally obligated airports (Federal Aviation Administration, 2021).

1.3. Research Objectives

This research project aims to understand relevant theories in optics, differential geometries, building physics, etc., to accurately describe the solar convergence phenomenon and create a simple guideline and numerical models. Ultimately, this will lead to the development of scripts and algorithms which will be useful to assess the solar convergence occurrence and the severity for any building which Rhino model is available. Partially and fully reflective façades will be covered, considering different shapes and materials in relation to the building's geographic location. This ensures that prior to constructing a building, the risk of dangerous effects from solar reflectance could be assessed so that it remains within safety limits. Furthermore, it should be noted that reflection under direct solar radiation is inherent or inevitable since achieving surfaces with nearly zero reflection on the Lambertian reflection scale for a façade surface is impossible, cost-ineffective, or clashes with the specific purpose of the building.

1.4. Research Scope

This research will initially approach the problem analytically to understand the behavior of light reflection as a function of the angle of incidence. Then, a simple two-dimensional model will be employed to understand the fundamental behavior of optics under light rays. The 2D approach can be used for the assessment of reflective surfaces with regular geometries that can be described in a mathematically simple way, such as surfaces with conic cross-sections (circular, elliptical, parabolic, and hyperbolic).

The next step is to model the solar convergence phenomenon in a three-dimensional domain and employ more complex parameters. The primary inputs will include measured (or mathematically modeled) sun path diagrams from specific geographical locations, as well as the reflective material properties and the geometrical shape of the façade itself. The novelty in this method is the development of scripts employing automated calculation of reflectance rate as a function of angle of incidence and the employment of anisotropic sky models. Despite this novelty, this research will be limited to specular reflection only, without considering diffusive reflection. Additionally, factors such as vapor, humidity, and particulate matter in the air will be negligible and thus neglected.

Ultimately, the primary output will be an implementable Grasshopper script that will be easy for architects and engineers with limited knowledge to utilize, compared to third-party plug-ins (e.g., DIVA, Honeybee Radiance, etc.), which require moderate ability in heavy scripting.

1.5. Research Questions

Based on the context, problem, and scope described on the previous subchapters, the following main question can be formulated as:

"What design rules can be formulated for curved façades of buildings, and how can a reliable 3D numerical script be developed to predict and prevent the unintended occurrence of concentrated bundles of excessive solar reflections on nearby surfaces?"

To achieve the research objective, the following research questions will be discussed:

- What are the parameters that cause the problem of converged solar reflection, and how can a model be developed to capture the physics behind the phenomenon?
- What constitutes the acceptable limits for both human safety (e.g., sunburn) and temperature-related problems (e.g., melting objects)? And do the simulation results reflect this concerning irradiation?
- What is the expected error of the developed model compared to the measured data?
- What is the effect of input uncertainties?

2 | Literature Review

In general, the impact of solar reflectance from building façades has been a critical area of research due to its implications for urban heat islands, pedestrian comfort, and building energy performance. However, a more specific problem of converged solar reflection has not been deeply explored. This chapter traces the evolution of research in this field, starting from the earliest occurrence and considerations to the more recent advancements.

2.1. Early Studies and Foundational Work (2010-2018)

The problem of converged solar convergence was recorded as early as 2010, when the Vdara Hotel in Las Vegas caused severe sunburn to visitors swimming in the pool and even melted plastic cups (ABC News, 2010). It was reported that within the pool area, the increase in temperature from the phenomenon could reach up to 20 degrees Fahrenheit (6.67 °C) (Garfield, 2015). Despite this massive temperature increase, the hotel only installed giant umbrellas over the pool deck. This solution proved ineffective, as it still caused discomfort from glare, increased the temperature on the pool's sidewalk, and required numerous umbrellas since the hotspot moved across the pool area as the day progressed, resulting in large area to cover.

(a) (b)

Figure 2.1(a) The reflecting concave façade of Vdara Hotel (Garfield, 2015) and (b) umbrellas to cover the death ray (booking.com, 2024)

The incident at the Vdara Hotel did not immediately trigger research related to the problem. However, in 2012, Brzezicki investigated similar phenomena due to concerns about glossy façades causing glare. He modeled various shapes of glossy façades—rectangular, convex, concave, and angular—using 3D Studio Max, which employs photo-emission ray-tracing rendering. His detailed examination of concave façades from a circular arc included mathematical analysis of caustic curve formation. However, the paper could not predict glare intensity in W/m^2 accurately; instead, it uses a new unit called the multiplicative factor (MF) to estimate luminance values of the glare compared to luminance of unaffected areas (Brzezicki, 2012).

The paper concluded that concave façades, despite having limited reflection glare area (RGA), have significantly higher MFs, vice versa. For buildings in the Northern Hemisphere, concave and convex

south façades produce the highest RGAs (thus the lowest MF) at lower solar altitudes. This condition was claimed to mostly occurs during times of low solar illumination, but the cases of Amsterdam UMC and the Walkie Talkie building are examples where this is not the case and lead to catastrophic damage.

Research on converged solar reflections began to appear sparsely after the "Death Ray" phenomenon from the Walkie Talkie building in 2013. Foundational work in this field is represented by studies such as those by Ryan Danks et al (Danks et al., 2016a) (Danks et al., 2016b). Danks and colleagues noted the lack of regulation on reflection problems due to the absence of universally accepted criteria defining acceptable limits of reflected visible light and thermal irradiance in urban areas. The paper highlights the importance of considering who or what is impacted by solar irradiance and the potential danger of sunburn. It proposes separate quantitative criteria for visual and thermal impacts of reflections, applicable only after a reliable method to measure and predict reflection irradiance has been known. Although the proposed criteria can be suitable for both design purposes and post-construction assessment, the schematization of the façade to create and propose the criteria is limited to only one model, meaning that the effect in geometry of the façade has been largely neglected. Another shortfall of the proposed criteria is that the literature on which it is based is still limited in breadth, relying on sparse research, authors' opinions, and experience.

The same group of researchers continues their work, qualitatively discussing critical decisions and design trade-offs that façade designers need to consider to avoid visual and thermal reflection issues (Danks et al., 2016b). They provided insights on preventing the converged solar reflection phenomenon by incorporating vertical discontinuities in buildings from one story to another as shown in Figure 2.2, creating multiple lower-intensity focal areas. For post-construction measures to address converged solar reflection problems, they proposed two categories of mitigation options: modifying reflecting surfaces (e.g., hand sanding to allow for diffuse reflection or installing anti-reflective coating to reduce reflection intensity) and obstructing reflections (e.g., installing *mashrabiya*, *sudare*, or *brise-soleil*). The authors noted that the tools available to model solar convergence accurately require steep learning curves, but no alternative solution was found at that time.

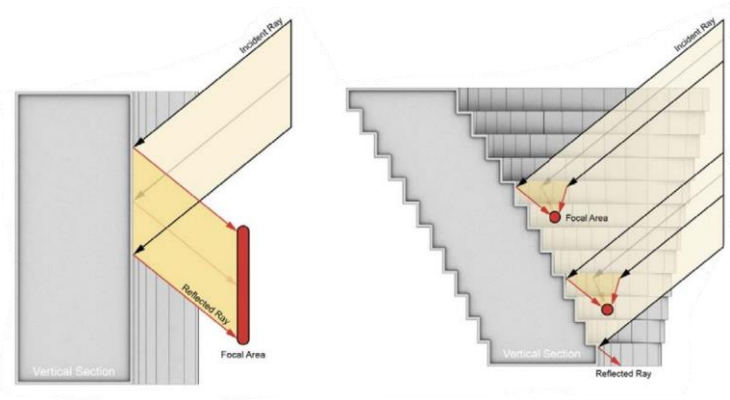

Figure 2.2 The effect of façade discontinuity to reduce the intensity of the reflection (Danks et al., 2016b)

Ruth Shilston and Ryan Danks (2018) continued this trajectory by focusing on the simulation of urban solar reflections and their impact on building performance because the phenomenon of converged solar reflection is closely related to the implementation of building physics to improve

building services. For example, while the use of high-performance façades can reduce internal heat loads, it will result in generally higher reflectance to the urban environment (Shilston & Danks, 2018). Additionally, the authors argued that the worst cases of converged solar reflection problems can only be simulated when the modeler utilizes clear-sky input data to ensure that the full extent of the potential glare impacts are accounted for and intensities at specific hours are not skewed down due to cloud cover. Therefore, it is important for the modeler to understand the necessary fundamental concepts of building physics and optics, and to know the assumptions used as input data so that the limitations of the model are known. They also mentioned that high-performance glazed façades will reflect much of the sun's thermal energy, much more than that of visible light energy. One misconception many façade engineers fail to understand is that the reflectivity of an interface between one medium and another (i.e., air to glass) is not a fixed value, which adds to the complexity of the problem.

2.2. Advancements in Simulation and Modelling (2018-2020)

Roel et al., in their paper, validated the reliability of modeling such problems with Rhino-Grasshopper effectively, which can be done during the design process of buildings, and acknowledged that extensive cases to push the limit of the worst-case scenario are yet to be done (R. Schipper et al., 2018). They focused on creating several models, including a single curve model, a double curve model, creating the vicinity from simple boxes, calculating the irradiance with DIVA, and converting it into temperature. They also used Galapagos to perform genetic algorithms, investigating the maximum intensity of focal points on reference days. However, in their model, they simplified several properties from optics, such as assuming the reflection properties of the façade to be constant, and no error in placement or randomness factor is taken into consideration.

Jiajie Zhu et al. conducted a computer simulation recreating the sunlight concentration phenomenon that occurred from the curved façade of the Walkie Talkie building on Fenchurch Street, London, in 2013 (Zhu et al., 2019). In their paper, they modeled the phenomenon using a suite of programs called Radiance and rendered the irradiance map utilizing a sub-program called Falsecolour Radiance. Although they employed different sky conditions (i.e., standard clear sky, standard intermediate sky, and standard overcast), they only used isotropic skies and had limited information regarding the accurate geometry model and surface parameters of the façade (e.g., reflectivity of double glazing, façade, etc.).

2.3. Focus on Experimental and Comparative Studies (2020-2023)

In 2022, Speroni et al. conducted an experiment where they created six 1:100 scale models mimicking typical tall buildings with three façade geometries (i.e., classic vertical, 10% tilted, and curved concave) and two finishing materials (specularly reflective and diffusely reflective) (Speroni et al., 2022). Similar to the paper by Brzezicki, the paper by Speroni et al. suggests that caustic curve formation is the source of high irradiance in both specularly and diffusely reflective façades.

Wen et al. conducted a comparative study in which they investigated the impacts of highly reflective building façade materials on the thermal and visual environment of an office building in a tropical climate context (Wen et al., 2020). In their paper, they present a case study where a 9-story building with a curved stainless steel façade in Singapore produces discomfort glare to the surrounding buildings due to direct exposure to reflected sunlight. In one of the affected buildings, they collected data on changes in four parameters (i.e., air temperature, glass temperature, wall surface

temperature, and indoor illuminance) by placing sensors in nine locations. They concluded that weather conditions play a vital role in both indoor thermal conditions and the outdoor visual impact. Even though the researchers did not make any models or prototypes, their approach of conducting on-site measurements and considering weather conditions can provide valuable insights.

2.4. Recent Development and Numerical Model Refinement (2023)

Rather than developing numerical model and doing an experiment separately, in 2023, Schipper and Brembilla built the earliest numerical model to simulate the converged solar reflection phenomenon in the Amstedam UMC building as well as checking for the real converged solar irradiance (H. R. Schipper & Brembilla, 2023). They checked the visual results using various components from the Grasshopper visual programming language and coupled it with simulation which was done in Radiance. However, the numerical model underestimated the result by 300 to 500 W/m^2 compared to the real conditions. The initial assumption is that it happens because of the change in façade geometry from the specification document for economic feasibility without advance knowledge of the risks.

2.5. Conclusion from Literature Review

From the stated literature review above, it is apparent that the main topic of creating a Grasshopper script to accurately model the adverse effects of converged solar reflection from a complex curved façade, which automatically integrates anisotropy in the sky models, non-constant reflectance rates, as well as investigates the fundamental behavior between the intensity of focal points and the geometry of the façade itself, remains unnoticed. The urgency to create one arises because, in practice, building authorities in large metropolitan cities such as Shanghai, Singapore, Hong Kong, and Sydney often do not conduct assessments related to the risk of solar convergence prior to the groundbreaking and construction of buildings, especially those with curved reflective façade materials. Instead, they implement an output-oriented ban wherein the reflection from a façade may not exceed 20% of the radiance; any reflection beyond that is considered a nuisance (Danks et al., 2016a). This approach is unwise since, for example, in the case of Amsterdam UMC, even façades with great transparency and reflection factor of 24% (of which 16% for the visible part) still cause massive overheating even though the building is relatively small enough with only two storeys (H. R. Schipper & Brembilla, 2023).

The conventional method mentioned above is also unfeasible because repairing issues after the façade and building have been erected will require additional construction costs. Additionally, the solution may possibly cause another type of nuisance other than reflected sunlight. For instance, while there was a solution proposed to put vertical mullion fins to disrupt and minimize reflection from a certain sun angle, this solution also raises other problems such as wind loadings and aeroacoustics noise (Shilston & Danks, 2018). The complete details of the paper mentioned in this chapter can be found in Appendix A.

3 | Theoretical Framework

In this chapter, relevant factors, theories, and equations that describe the solar convergence phenomenon and ways to reconstruct it will be discussed.

3.1. Relevant Factors

To identify the most relevant factors involved in this research, the variables are broken down into several groups, which are:

1. Independent (input) variables: solar declination, latitude, time of the day, optical material properties, orientations of the façade, geometry of the façade and solar radiation. These variables are expected to be the cause,
2. Dependent (outcome) variable: irradiance of the reflected sunlight on the ground, which is the expected result,
3. Mediating variables: solar height, solar azimuth, and sky anisotropy, which will link and better explain the relationship between the dependent and independent variables, and
4. Moderating variables: clearness index/cloud cover, horizon brightening, blockings, and façade imperfections, which change the relationship between the independent and dependent variables and are not affected by the independent variables.

3.2. Visualization of the relationships between the relevant factors

The abovementioned variables are presented in Figure 3.1 with their relationships to each other. The main independent variables subject to change will be those located in the bottom right corner: material properties, geometry of the façade, and the orientation of the façade. The circle represents a cumulation of input data and/or transformed data.

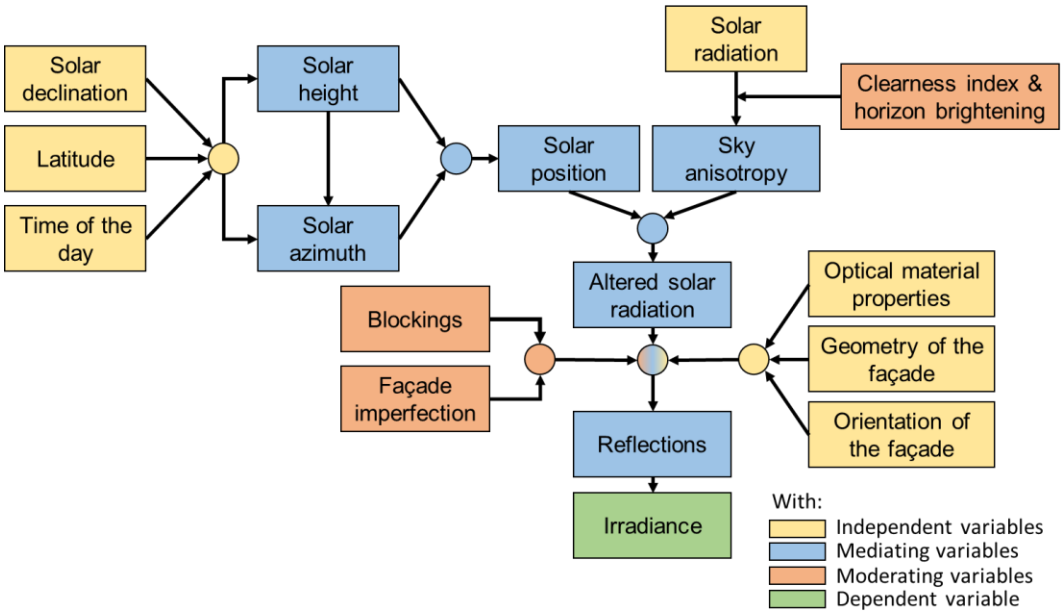

Figure 3.1 Theoretical framework and the relationship between relevant factors

In order to better explain the role of each variables, theories and equations will be explained in this chapter.

3.3. Sun Path

Sun path diagrams are one type of solar charts that represents the path that the sun appears to follow across the sky dome and projected onto a horizontal surface as the earth rotates and orbits the sun (DeKay & Brown, 2013). Sun's trajectory in the sky and the corresponding temperature is different for specific latitudes and specific location, thus resulting in, for example, different radiation, different heat gain inside a building, and different performance for solar energy systems throughout the year (Kuhn et al., 1998). The left part of Figure 3.2 is the example of sun path on a polar graph for any location at the latitude of Rotterdam drawn accordingly to the solar time, and the right part of the figure is the same sun path but drawn accordingly to the clock time, in this case Middle European Time, which has a slightly curved change of path due to analemma. Several periods of interest that the mentioned problem may rise is during:

- Equinox (March 21st and September 23rd) in which the sun shines perpendicularly to the earth axis, which will give more direct and the most perpendicular radiation to the vertical southern façade of the buildings in the Northern hemisphere.
- Summer solstice (June ~21st) in which the northern hemisphere begins the summer season and which the sun is at its maximum angle or declination (61.4° in the Netherlands) (Janssen, 2023).

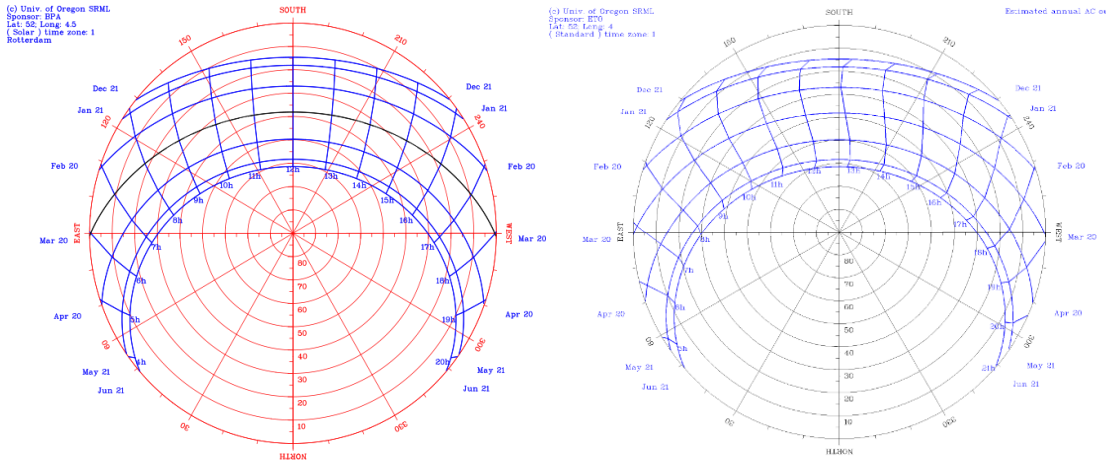

*Figure 3.2 Sun path for any location at the latitude of Rotterdam (*University of Oregon Solar Radiation Monitoring Laboratory: Sun Chart Program*, 2024)*

Some of the most basic equations to represent the position of the sun, which will be useful to recreate the model, are:

Declination (δ)

Declination represents the angle between the solar beams and the equator, as shown in the Figure 3.3 below. Declination can be conveniently approximated using the Equation 3.1 below.

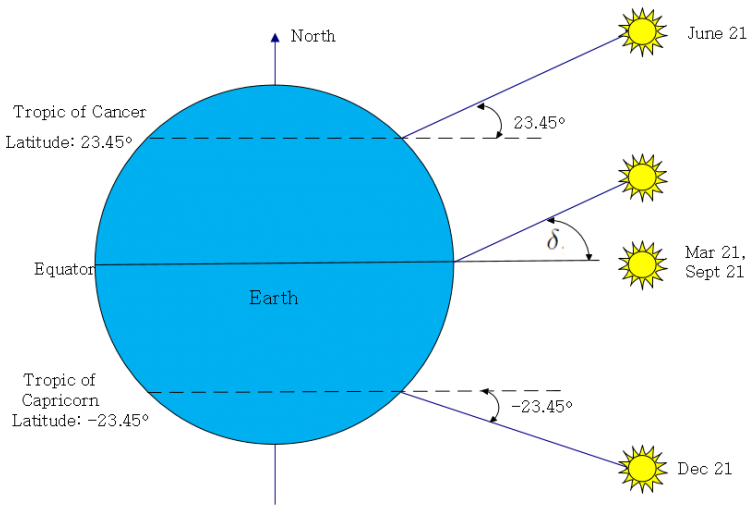

Figure 3.3 Illustration of the solar declination (δ) angle (Gurupira, 2018)

$$\delta = 23.4 \times \sin\left(\frac{360° \times (284 + N)}{365}\right) \quad 3.1$$

With,

N = day of the year (DOY)

Solar Height (h) and Solar Azimuth (a)

Solar height refers to the angle of the sun above the horizon, typically measured in degrees. Therefore, solar height can be formulated as shown in the Equation 3.2. Meanwhile, azimuth is an angle between the projection of the sun and the south-axis. Prior to noon (12:00 solar time), the azimuth has a positive value, which then will turn to a negative value after it. Azimuth can be calculated using the equation Equation 3.3. Figure 3.4 below illustrates how the position of the sun at a point on Earth is recorded using sun altitude and azimuth (Janssen, 2023).

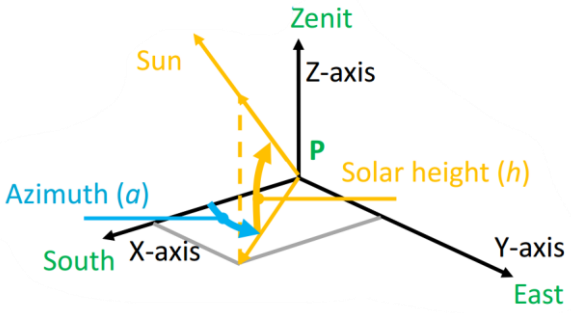

Figure 3.4 Illustration to calculate solar height (Janssen, 2023)

$$h = sin^{-1}(sin\varphi \times sind - cos\varphi \times cosu) \quad 3.2$$

$$a = \pm cos^{-1}\left(\frac{-(sin\varphi \times cos\delta \times cosu + cos\varphi \times sin\delta)}{cosh}\right) \quad 3.3$$

With,

φ = latitude

u = hour angle (t × 15°)

δ = declination

t = hour

3.4. Solar Radiation

The sun is among the natural emitters of the electromagnetic spectrum. Within that broad spectrum ranging from 200 nm to 3000 nm, there is a band of wavelengths (380 nm to 780 nm) that human eyes can perceive as visible light (NASA Science Mission Directorate, 2010). This same range of wavelengths is also where the thermal energy coming from the sun is at its highest as can be seen in Figure 3.5.

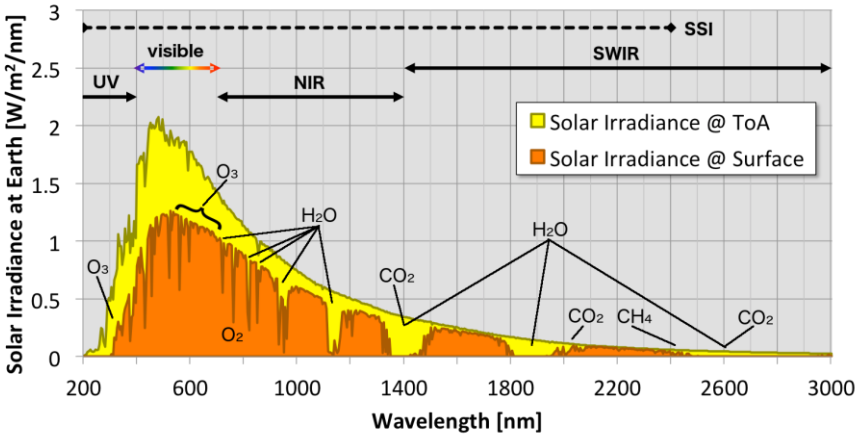

Figure 3.5 Solar Irradiance at the top of atmosphere (ToA) and at the surface (National Aeronautics and Space Administration, 2018)

The energy output (ψ_λ) from any source of emitters could be described with the terms from radiometric quantities below (Brembilla, 2023),

Radiant flux :	The quantity of radiant energy released by a specific point source uniformly in every direction at a particular rate [J/sr].
Radiant intensity :	The quantity of radiant energy released at a specific rate within a three dimensional angle [W/sr].
Radiance :	The quantity of energy released or reflected by a surface at a specific rate within a three-dimensional angle per square meter [W/sr/m^2].
Irradiance :	The quantity of radiant energy emitted by a source at a specific rate that falls on a surface (irradiates), per square meter [W/m^2].

With J, W, and Sr being Joule, Watt, and Steradian, respectively.

In the context of solar energy assessment, utilization, and engineering, radiation from the sun can be categorized into several terms (MINES ParisTech / Vaisala, 2024) as can be seen in Figure 3.6 and Figure 3.7, which include,

Beam Horizontal Irradiance (BHI)

BHI represents the intensity of the solar radiation parallel to the rays when the measuring plane is horizontal at ground level and facing upwards. This type of irradiance comes from the rays that travel in a straight line from the sun at its current position in the sky.

Diffuse Horizontal Irradiance (DHI)

DHI represents the irradiance from solar radiation that does not arrive in a straight path from the sun; rather, it has been scattered by overcast/clouds and particles in the atmosphere. In the isotropic sky model, DHI is represented as having the same intensity from any part of the sky dome and equally distributed in all directions.

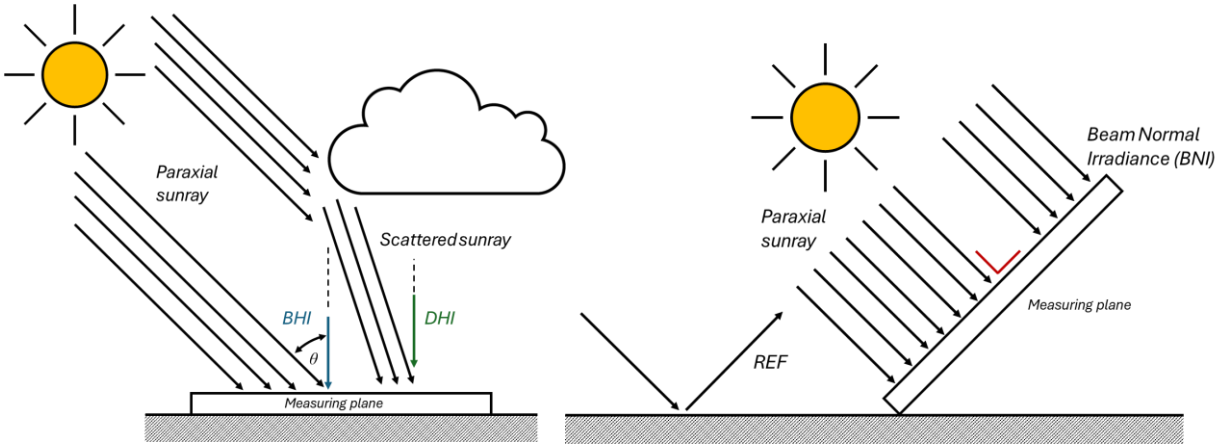

Figure 3.6 Illustration of BHI, DHI, REF, and BNI

Reflected Ground Irradiance (REF)

Reflected Ground Irradiance represents the radiation that appears due to the reflectivity of ground surfaces (also known as albedo). The value for the reflected ground irradiance varies for different types of ground surfaces. For example, the reflected ground irradiance of new concrete pavements will be higher than that of older ones or compared to soil.

Beam Normal Irradiance (BNI) or Direct Normal Irradiance (DNI)

BNI represents the intensity of solar radiation perpendicular to the measuring surface and parallel to the rays. For photovoltaic (PV) applications, the measuring plane is designed to be mobile, allowing it to tilt and rotate according to the angle of the sun. This ensures that the solar rays always hit the measuring plane at normal incidence, maximizing the solar energy input into the PV system. In this thesis, the term BNI will be used more often to avoid confusion between direct and diffuse components when using the acronym DNI.

Global Horizontal Irradiance (GHI)

GHI represents the total hemispheric irradiance incident on a horizontal surface at ground level. It is a result of the summation from the first three parameters mentioned above (Dasari et al., 2019), can be seen in the Equation 3.4.

$$GHI = BHI + DHI \qquad 3.4$$

Global Tilted Irradiance (GTI)

GTI represents the irradiance directly from the sun, irradiance scattered from the clouds, and due to the reflectivity from the ground received in a measuring plane which is tilted at a certain angle (β) from the true horizontal (Ourraoui & Ahaitouf, 2022).

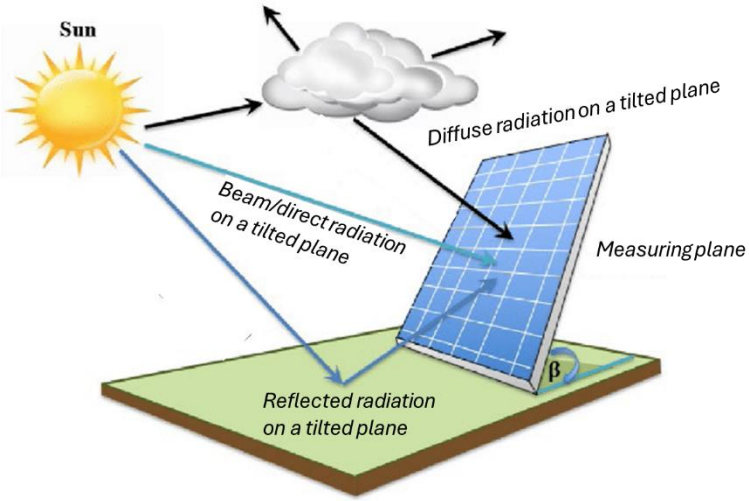

Figure 3.7 Direct, diffuse, and reflected radiations of solar irradiation (modified) (Ourraoui & Ahaitouf, 2022)

3.5. Cloud Cover

Cloud cover affect how much solar radiation from the sun will be absorbed or reflected by Earth's atmosphere (The Globe Program, 2024). Higher cloud cover indicates lower solar radiation since most of them are reflected back into space and the rest is scattered into different directions in the atmosphere, creating diffuse radiation. Even though cloud cover estimates are still relatively subjective and relies on visual inspection, the observation provides good insights in determining the clearness index of the sky (F') which will later be useful to construct sky models. For general purposes, cloud cover measurements exclude the conditions of the horizon. The categorization of cloud cover can be seen in the Figure 3.8 below.

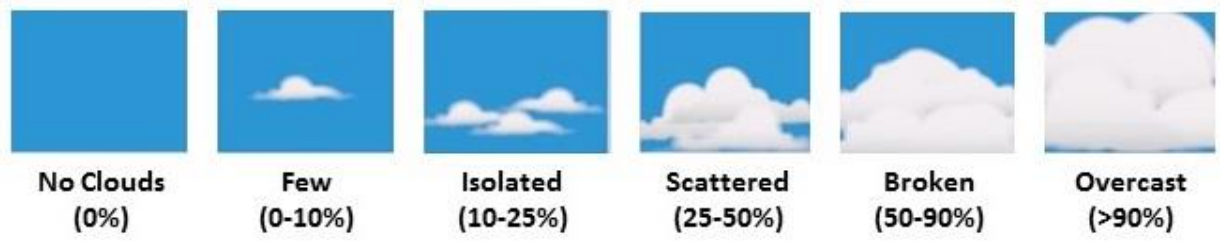

Figure 3.8 Sky and cloud cover conditions (The Globe Program, 2024)

3.6. Material Optical Properties

When light of any spectrum hits arbitrary materials, several possibilities regarding the kind of interaction that might occur between the light and the materials could be categorized into three aspects: reflection (ρ), absorption (α), and transmission (τ), which are all unitless properties and

expressed in percent [%]. In terms of how materials transmit light, they are categorized into two types:

- transparent/translucent materials with visible light transmittance (τ) > 0, and
- opaque materials with transmittance equal to zero.

One of the simplest examples of transparent materials is glass, which has varying visible light transmittance values depending on the glazing system. For instance, clear single-glazed glass has about 88% transmittance, while double-glazed glass has around 76% transmittance. As mentioned previously, low-emissivity coatings in high-performance systems are often chosen to reduce internal heat loads by allowing visible light (spectrum 380 nm to 780 nm, as shown in Figure 3.5) to pass through while blocking near-infrared (NIR) and short-wave infrared (SWIR) energy (Danks et al., 2016b), preventing heat from entering a building. This results in a transmittance of around 69%, as shown in Figure 3.9 (Brembilla, 2023).

To measure the full-spectrum reflectance of a certain glazing system, its reflectances across the full solar spectrum are weighted-averaged. Therefore, under the same intensity of sunlight, since high-performance glass reflects much of the IR energy, it also has a higher reflectance rate across the full spectrum compared to single-glazed or double-glazed façades, causing much more intense reflection irradiance.

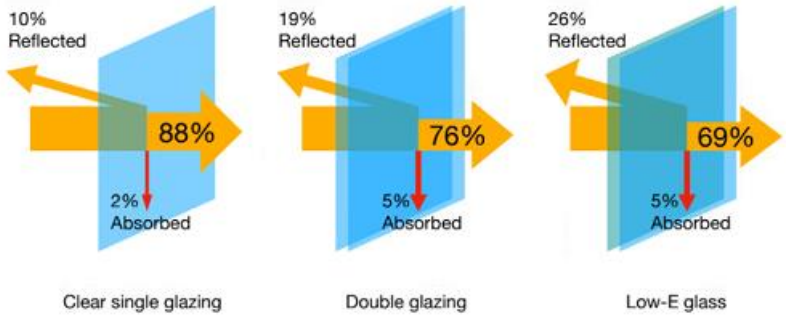

Figure 3.9 Transmittance rate in relation to the type of glazing (Brembilla, 2023)

On the other hand, most building materials fall into the category of opaque material. Opaque materials can be classified into three types of categories in terms of how they reflect light according to the Figure 3.10 below:

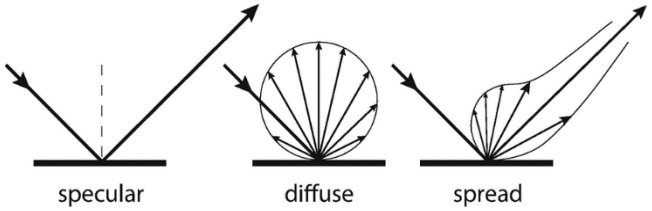

Figure 3.10 Behavior of opaque materials in reflecting incoming light (van Bommel, 2019)

From left to right,

- Perfectly specular materials, in which the materials behave like a mirror that reflect incoming light in a single direction that is specular to the normal of the surface or in other words, they reflect light back at an angle mirroring the incoming radiation angle.
- Perfectly diffusing materials (Lambertian reflectance), in which materials diffuse the incoming radiation uniformly in all directions, eliminating any highlights coming from the surface.
- Materials that lie in between perfectly specular and perfectly diffusive, which spreads the incoming light into random patterns thus hard to characterize (van Bommel, 2019).

3.7. Effective Reflectance Rate

According to Danks, et al. (2016), reflectance rate of a glass is not a fixed value. This fact is also strengthened with the simulation conducted via WINDOW software developed by Lawrence Berkeley National Laboratory which will be shown on the next chapter.

This phenomenon happens due to the effective Fresnel equation (R_{eff}) as can be seen in Equation 3.5, which stated that despite the refractive indices the materials involved, the proportion of the reflected light approaches 100% as incident light rays strike the interface/surface at more glancing angles. The illustration for the position of the angle of incidence itself can be found in Figure 3.11.

$$R_{eff} = \frac{R_s + R_p}{2} \tag{3.5}$$

With,

R_s = reflectance for s-polarized light,

$$R_s = \left| \frac{n_1 cos\theta_i - n_2 \sqrt{1 - \left(\frac{n_1}{n_2} sin\theta_i\right)^2}}{n_1 cos\theta_i + n_2 \sqrt{1 - \left(\frac{n_1}{n_2} sin\theta_i\right)^2}} \right|^2 \tag{3.6}$$

R_p = reflectance for p-polarized light,

$$R_p = \left| \frac{n_1 \sqrt{1 - \left(\frac{n_1}{n_2} sin\theta_i\right)^2} - n_2 cos\theta_i}{n_1 \sqrt{1 - \left(\frac{n_1}{n_2} sin\theta_i\right)^2} + n_2 cos\theta_i} \right|^2 \tag{3.7}$$

n_1 = the refractive index of the medium from which the light is coming

n_2 = the refractive index of the medium into which the light is entering

If n_1 = 1.0 (refractive index of air) and n_2 = 1.5 (typical value for glass) are used, then the value of R_{eff} for angles of incidence 30°, 45°, 60°, 80°, and 90° are 4.15%, 5%, 8.9%, 38.7%, and 100%, respectively, indicating a non-linear and non-constant behavior of reflectance rate.

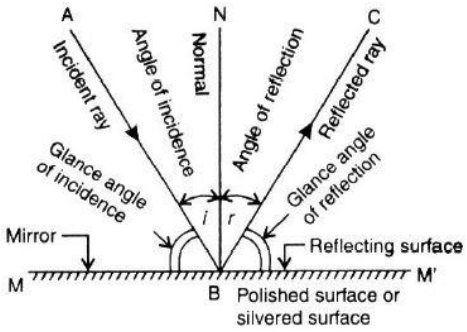

Figure 3.11 General Terms to the Reflection (3rdFlix, 2021)

3.8. Curvature and Normal Vector

For a curved façade, curvature and normal vector of the surface are two of the most important aspects in this assessment. Curvature itself is referred to as local or intrinsic property that measures how sharply a curve bends at each individual point without considering the surface location or orientation in space. It depends only on the geometrical changes of infinitesimally small neighbourhood around the measured point (Stewart, 2012). For a straight line, curvature can be found with Equation 3.8 below.

$$\kappa = \frac{(\varphi + d\varphi)}{dx} = \frac{d^2z}{dx^2} \qquad 3.8$$

With, φ being the difference in angle between the tangent of the point on a surface with the global horizontal axis. In numerical modelling, often time finite difference scheme is utilized to approximate the curvature of a surface based on two adjacent discrete points. The approximation can be achieved using Equation 3.9.

$$\frac{d^2z}{dx^2} = \frac{d}{dx}\left(\frac{dz}{dx}\right) \approx \frac{\left(\frac{\Delta z}{\Delta x}\right)_b - \left(\frac{\Delta z}{\Delta x}\right)_a}{a} \qquad 3.9$$

With *a* and *b* being the two reference points for calculation.

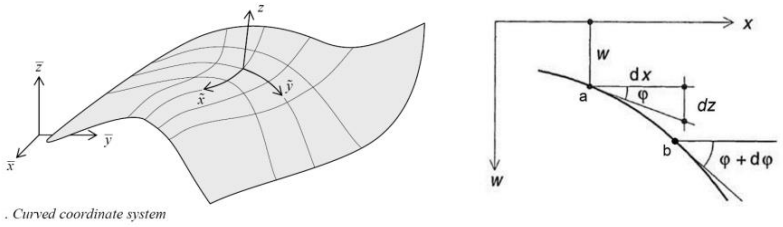

Figure 3.12 Curved shape illustration (Borgart, 2023)

In the simplest form, curvature can also be expressed as the inverse of radius (*R*) as can be seen in Equation 3.10.

$$\kappa_i = \frac{1}{R_i} \qquad 3.10$$

In a surface, the shape of a surface is primarily characterized by two principal curvatures which are perpendicular to each other. They describe how the surface curves in different directions at a specific point. Together, these two parameters indicate the maximum and minimum curvatures at that point. The product of the two principal curvatures are called as Gaussian curvature (*K*) in which the formula can be found in Equation 3.11. It indicates the overall shape of the surface, the result is either mono curvature, synclastic, or anticlastic, as shown in Figure 3.13 below.

$$\mathrm{K} = \kappa_1 \kappa_2 = \frac{1}{R_1}\frac{1}{R_2} \qquad 3.11$$

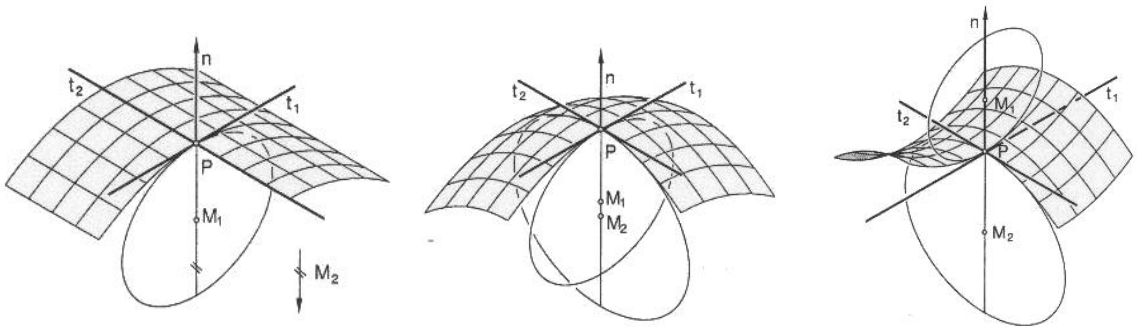

Figure 3.13 Visualization of mono (k = 0), synclastic (k>0), and anticlastic (k<0) curvature on a surface (Ferreol, 2017)

On the other hand, normal vector of a curved surface is also important to calculate since the angle of reflection pivot around the normal vector in relation to the angle of incidence. Normal vector of an arbitrary surface can be found with Equation 3.12.

$$\mathbf{N} = \left(-\frac{\partial f(x,y)}{\partial x}, -\frac{\partial f(x,y)}{\partial y}, 1\right) \qquad 3.12$$

3.9. Sky Models

Researchers have been trying to accurately simulate the solar convergence problem from reflective façades, but there has been a gap in considering different sky models. Therefore, in this thesis, different isotropic and anisotropic sky models, which actually come from the solar energy engineering branch of science, have been scrutinized.

There are several different sky model equations that have been developed since 1960, following the formulation of isotropic sky model which was initially presented by Hottel and Woertz in 1942 and refined by Liu and Jordan in 1960 (B. Y. H. Liu & Jordan, 1960).

3.9.1. Isotropic Sky Model

The first sky model that will be discussed here assumes that diffuse radiation from sun is uniformly distributed over the sky dome with the same intensity in all directions. Thus, the isotropic sky model gives good results for overcast sky conditions (Dincer et al., 2015). The isotropic sky model also

assume that the ground-reflected radiation will be uniformly distributed. According to the model, the total radiation on a tilted plane can be calculated using Equation 3.13 as follows (Kalogirou, 2009).

$$G_t = R_B G_B + G_D \left[\frac{1+\cos(\beta)}{2}\right] + (G_B + G_D)\rho_G \left[\frac{1-\cos(\beta)}{2}\right] \qquad 3.13$$

With,

R_B = beam radiation tilt factor

$$R_B = \frac{cos(\theta)}{cos(\phi)}$$

θ = angle of incidence

φ = solar zenith angle

G_B = beam radiation on a horizontal surface (W/m^2)

$$G_B = G_{Bn} cos(\phi)$$

β = façade slope angle

ρ_G = specular reflectivity of the ground surface/ground albedo

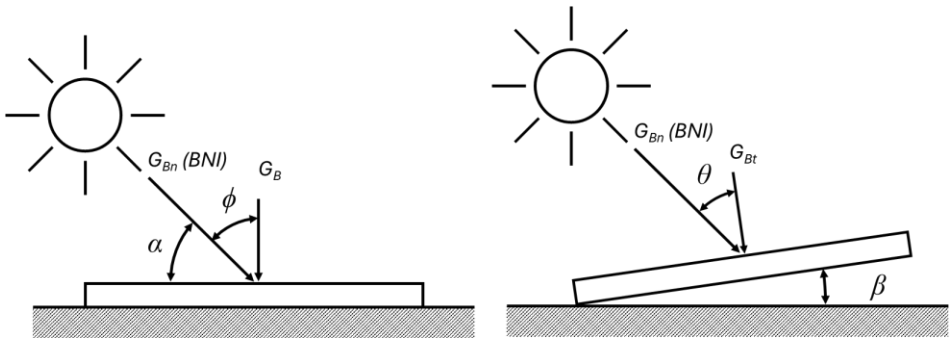

Figure 3.14 Beam normal irradiance resolved on horizontal and tilted surfaces

3.9.2. Anisotropic Sky Models

Other than the isotropic sky model, which assumes all diffuse radiation is uniformly distributed, there are several sky models that take more parameters into account. To make things less complicated, in this research, only three other sky models will be used, which will be described below.

Klucher Model

Klucher found that the isotropic-sky insolation model fits empirical data well under low-intensity conditions during overcast skies (Klucher, 1978). However, it underestimates the amount of solar radiation on tilted surfaces at intensity levels above approximately 50 W/m^2.

The Klucher model complements the isotropic model by taking into account two factors: horizon brightening,

$$\left[1 + F' sin^3\left(\frac{\beta}{2}\right)\right]$$

and circumsolar diffuse radiation,

$$[1 + F' cos^2(\beta) sin^3(\phi)]$$

Notice that the model considers the clearness index of the sky (F'), which approaches 1 on very sunny days and decreases to 0 on completely overcast days, effectively reducing the model to an isotropic model in the latter case. The clearness index can be calculated with the Equation 3.14, and the complete equation for the Klucher model can be seen in the Equation 3.15 (Kalogirou, 2009).

$$F' = 1 - \left(\frac{G_D}{G_B + G_D}\right)^2 \tag{3.14}$$

$$G_t = R_B G_B + G_D \left[\frac{1 + cos(\beta)}{2}\right]\left[1 + F' sin^3\left(\frac{\beta}{2}\right)\right][1 + F' cos^2(\beta) sin^3(\phi)] + (G_B + G_D)\rho_G \left[\frac{1 - cos\,(\beta)}{2}\right] \tag{3.15}$$

Hay-Davies Model

Unlike Klucher, Hay and Davies created a model that takes into account isotropic diffuse radiation and circumsolar diffuse radiation but neglects horizon brightening, replacing it with an anisotropy index. The anisotropy index represents the portion of the diffuse radiation constituting circumsolar region, with the remaining portion is assumed to be isotropic. The equation for anisotropy index and for the total irradiance on a tilted surface according to Hay-Davies model can be seen in the Equation 3.16 and Equation 3.17, respectively (Kalogirou, 2009).

$$A = \frac{G_{Bn}}{G_{on}} \tag{3.16}$$

With,

G_{on} = extraterrestrial radiation measured on a normal surface (W/m^2)

$$G_{on} = G_{sc}\left[1 + 0.033 \times cos\left(\frac{360N}{365}\right)\right]$$

N = day of the year

G_{sc} = solar constant (1366.1 W/m^2)

$$G_t = R_B(G_B + G_D A) + G_D(1 - A)\left[\frac{1 + cos(\beta)}{2}\right] + (G_B + G_D)\rho_G\left[\frac{1 - cos\,(\beta)}{2}\right] \tag{3.17}$$

Reindl Model

In essence, the Reindl model is a combination of the Hay-Davies and Klucher sky models, as shown in Figure 3.15, but with slight adjustments and additional considerations. Therefore, compared to the isotropic sky model, the Reindl model takes into account three additional parameters: isotropic diffuse radiation, circumsolar radiation, and horizon brightening. The full equation for Reindl sky insolation model can be seen in Equation 3.18.

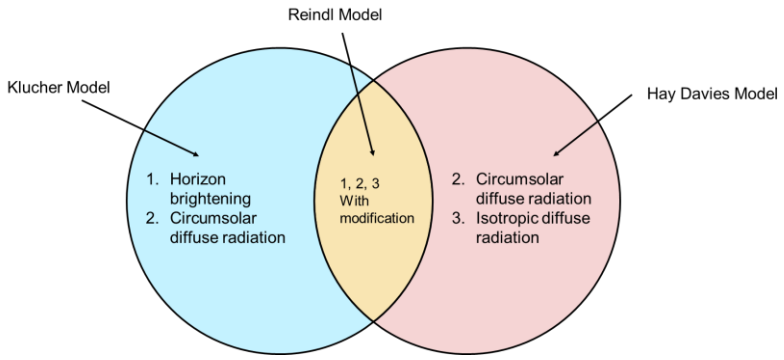

Figure 3.15 Considered factors in Hay-Davies-Klucher-Reindl models

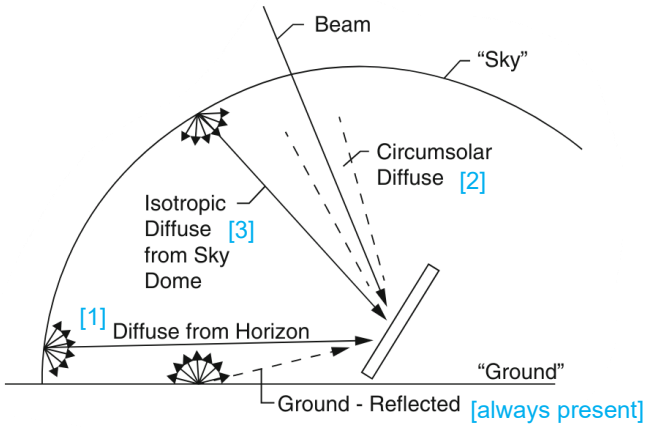

Figure 3.16 Illustration of the considered factors in Hay-Davies-Klucher-Reindl models (Martínez-Rubio et al., 2016)

$$G_t = R_B(G_B + G_D A) + G_D(1 - A)\left[\frac{1 + cos(\beta)}{2}\right]\left[1 + \sqrt{\frac{G_B}{G_B + G_D}}sin^3\left(\frac{\beta}{2}\right)\right] + (G_B + G_D)\rho_G\left[\frac{1 - cos\ (\beta)}{2}\right] \quad 3.18$$

3.10. Irradiation Tolerance

To know the extent to which irradiation will cause a harmful effect, it is necessary to compile the tolerance of many objects to heat flux before they begin to show signs of damage. According to British Standard PD7974-7, the National Fire Protection Agency (NFPA), and the Society of Fire Protection Engineers (SFPE), it is known that human skin may tolerate irradiance up to approximately 2500 W/m^2 during egress from a fire for a maximum duration of 30 seconds before the onset of pain (National Service Center for Environmental Publications (NSCEP), 2008; The British Standard Institution, 2021).

The tolerance value above can be used as an upper limit before damage occurs to human skin and should not be taken at face value. This is because there is a neglected factor: the expectation of high exposure to thermal radiation differs between a person escaping in the event of a fire and a person traversing an urban environment without the expectation of danger (Danks et al., 2016a). Therefore, Danks et al. argued that the short-term exposure limit for human skin unexpecting converged solar reflection should be around 1500 W/m^2.

Inanimate material, such as wood, on the other hand, has higher resistance; generally, it requires a minimum heat flux of 12000 W/m^2 for 1 minute before ignition occurs (Ågren, 2024). However, the ignition and charring of wood differ depending on the species, moisture content, grain orientation, etc. (Spearpoint & Quintiere, 2000). Another type of material to be considered is glass, which will experience cracks under a heat flux of around 2000 W/m^2 and 5000 W/m^2 for wired glass and float glass, respectively. Generally, glass needs 9000 W/m^2 before experiencing fallout and melting (Enomoto et al., 1999).

3.11. Summary from Theoretical Framework

This chapter elaborated on the critical factors influencing converged solar reflection phenomenon, including independent variables such as solar declination, solar radiation and optical material properties, as well as mediating and moderating variables such as solar height and clearness index. Various sky models, and equations essential for analyzing the converged solar reflection phenomenon and its impact on human skin and several objects have also been laid out. The parameters detailed in this chapter are used to create the 3D numerical modelling described in Chapter 4 | while the tolerance values are used as a threshold to determine to what extent the converged solar reflection phenomenon can cause damage in Chapter 5 | .

4 | Methodology

This chapter provides detailed insights into the methodologies used in on-site solar convergence observation and measurement, as well as in 2D and 3D numerical modelling.

4.1. Converged Solar Reflection Measurements

As mentioned in the previous chapters, there has been a case where the southern concave glass façade of the Amsterdam UMC building resulted in high-intensity converged solar reflections, which land in its parking lot one floor below. This is an interesting phenomenon because, compared to the Walkie Talkie building, which is a 38-story building and 160 m high, the Amsterdam UMC building is relatively small with only 2 stories and around 10.6 m high. Unlike the Walkie Talkie building, which has a curtain wall façade across all floors, the Amsterdam UMC building only has glass panels in its corridors located on the second floor.

Therefore, an on-site measurement to check for the irradiance of converged solar reflection was carried out in the parking lot of the Amsterdam UMC building to provide a reliable basis for comparison when building the Grasshopper and 3D Rhino model, which is explained later in this chapter, as well as to validate the irradiance value from the model. A specific time for the on-site measurement was chosen: Friday, 8 March 2024, as the phenomenon of convergence was expected to occur on this date in case of non-overcast sky conditions, based on earlier calculation results (H. R. Schipper & Brembilla, 2023). The measurement was effectively conducted from 10:46:45 to 16:08:00 local time.

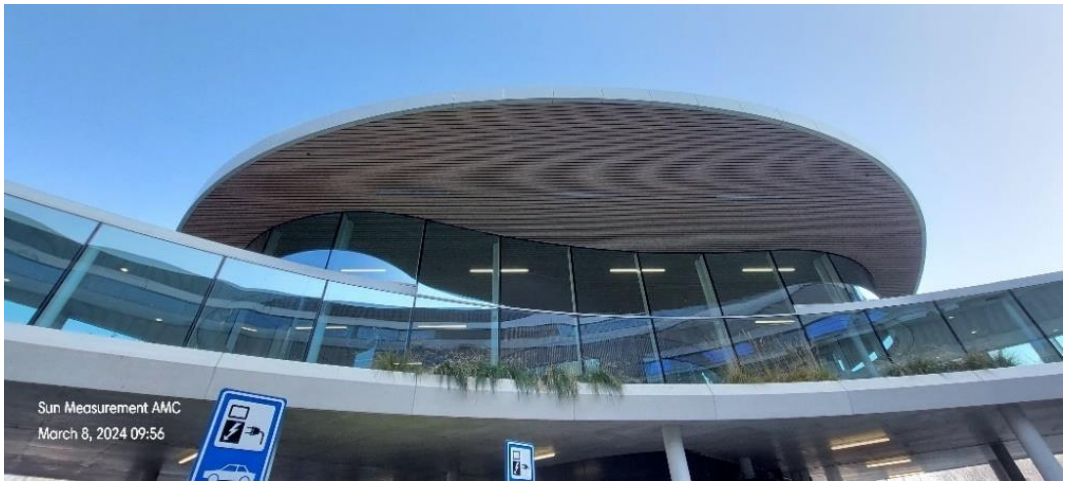

Figure 4.1 Southern façade of the Amsterdam UMC building

Figure 4.2 Test set up

4.1.1. Instruments

Several instruments were used to measure and document the occurrence, which included:

Two LSI Class B Pyranometer DPA154

To measure global solar irradiance in a hemispherical field of view, two pyranometers were employed, as depicted in Figure 4.3, with specifications detailed in Figure 4.4. These instruments are particularly suitable for assessing heat gain from solar radiation, as they measure a broad range of wavelengths from 285 to 3000 nanometers. This range significantly exceeds the visible light spectrum, which typically extends from 380 to 700 nanometers, as illustrated in Figure 3.5 (NASA Science Mission Directorate, 2010). Consequently, the pyranometers encompass not only visible light but also ultraviolet and infrared radiation.

Based on an earlier measurement conducted by Schipper and Brembilla, it was anticipated that the maximum irradiance during the on-site measurement at a specific location (focal point) can easily surpass 3000 W/m^2 (H. R. Schipper & Brembilla, 2023). Therefore, the measuring range of 0 to 4000 W/m^2 was deemed sufficient. However, as a precaution, to account for instances where the irradiance exceeded 4000 W/m^2, a light filter was used to tone down the readings. This filter was only applied when the irradiance surpassed 4000 W/m^2 to prevent errors in the pyranometer readings.

Figure 4.3 Class B Pyranometer DPA154 (LSI LASTEM, 2024b)

PN	DPA154
Output	µV
Protocol	-
Programmable output	-
RS485 protection	-
RS485 speed	-
Power supply	-
Max. Load	-
Power consumption	-
EMC	-
Thermopile sensitivity	10...15 µV/W/m^2
Measuring range	0...4000 W/m^2
Impedance	40 ± 3 Ω
Calibration certificate	Not included (see Accessories)
Cable	Not included (see Accessories)
Data logger compatibility	• Alpha-Log (using ALIEM module) • E-Log

Class B pyranometer	ISO 9060 2018 classification	Spectrally flat Class B (First Class)
	IEC 61724-1: 2017 classification	Class B (except for heating)
	WMO performance level	Good quality pyranometer
	WMO estimate on achievable accuracy for daily sums	±5%
	Spectral range	285...3000 nm
	Non-stability	<± 1% change per year
	Response time	20 s
	Non linearity	<± 1% (100...1000 W/m^2)
	Directional response (0...180°C field of view)	<±20 W/m^2
	Tilt response	<± 2%
	Temperature response	<2% (-15...35°C)
	Zero offset a (response to 200 W/m^2 net thermal radiation)	<12W/ m^2
	Zero offset b (response to 5K/h change in ambient temperature)	<±3 W/m^2
	Built-in bubble level	YES
	Operative temperature	-40...80°C
	Calibration traceability	To WRR
General Information	Housing	Anodized aluminum
	Recalibration	Every 2 years
	Mounting (pole Ø 45...65 mm)	Using DYA034 (horizontal) or DYA035 (tilting) arms + DYA049 collar
	Protection rate	IP66
	Anti-radiation shield	Included

Figure 4.4 Specifications of LSI Class B Pyranometer DPA154 (LSI LASTEM, 2024b)

Two white t-shirts for filters

As explained earlier, prior to conducting the measurements, a filter was employed to tone down the readings. The actual irradiance was subsequently calculated by scaling up the filtered readings in accordance with the known filter rate. Although the exact impact of the filter on the spectrum received by the sensor is unknown, it is likely that the filtering percentage of the textile is not constant across the full spectrum. However, for the purpose of this measurement, the following procedure was followed to establish the gross filter factor of the textile.

A white t-shirt consisting of two layers of cloth (front and back) was chosen as the filtering medium because UV transmission through white fabrics is significantly higher than through black fabrics (J. Liu & Zhang, 2015). Black fabrics tend to absorb a substantial portion of light (including infrared) and convert it into heat. The high transmission of light through white fabric results in more energy input retrieved by the pyranometers, thus providing more accurate readings.

Initially, the option to choose between one or two layers of highly transmissive white cloth during the experimental setup was considered advantageous, offering flexibility in adjusting the filtration level as needed.

Figure 4.5 A white t-shirt for filter

Two black paper boards as the pedestals for the pyranometers

The black paper boards were used to ensure that the pyranometers remained stable and faced the true vertical direction by observing the bubble/spirit level embedded in the equipment. Black paper boards were chosen to avoid increasing the readings of solar global irradiance, since darker color has a lower albedo, which reduces the reflected radiation (REF).

Figure 4.6 A black board for pedestal

E-log data logger for meteorological monitoring (EL03305.1)

To record and store data from the pyranometers as mentioned above, the E-log data logger for meteorological monitoring (EL03305.1), which can be seen in the Figure 4.7, was utilized.

Figure 4.7 EL03305.1 Data logger for meteorological monitoring instrument (LSI LASTEM, 2024a)

Samsung Galaxy A72 Camera

To identify which reflected irradiance corresponds to focal points and which to focal lines, pictures of the pyranometer placement location were taken, accompanied by detailed timestamps (including hours, minutes, and seconds). The description of the cameras used for capturing these images is provided below.

Figure 4.8 Mobile phone camera for documentation (SAMSUNG, 2021)

a. 64 MP AF, F1.8 OIS main camera
b. 12 MP FF 123°, F2.2 ultra wide-angle camera
c. 5 MP FF, F2.4 depth sensor
d. 5 MP FF, F2.4 macro

4.2. 2D Numerical Modelling Process

To understand the behavior of light convergence, which bounces off a mirror with a certain 2D geometrical shape, a simplified ray tracing approach on a 2D model was first discussed. In this approach, a collection of rays parallel to each other, coming from infinity, is used to approximate the convergence factor of perfectly specular concave spherical and aspherical mirrors.

This method comes from geometrical optics, where light is assumed to travel in straight lines from a point source. This behavior is also known as rectilinear propagation. As simple as it might sound, this method has several shortcomings, one of which is the complexity to accurately discretize the intensity of light from a specific source point into rays, because light is not a vector but an energy distributed in a continuous medium. If light or energy occupying a 3D space is discretized into extremely thin rays or vectors, which essentially are 1D elements, it implies the theoretical need for an infinite number of rays to accurately model it.

Therefore, in this approach, the density of paraxial rays and marginal rays is kept constant but limited to a specific value to ensure that the comparison of the reflection convergence behavior from one mirror to another remains reliable. Paraxial rays are light rays originating from infinity that are parallel to and in close proximity to the optical axis, while marginal rays are those that are further away from it. These rays, originating from infinity, are also referred to as a collimated beam.

For the 2D model, the Amsterdam UMC building will be used as one of the examples since the horizontal cross section of the southern façade of the Amsterdam UMC building can be assumed as a perfectly continuous concave spherical mirror without imperfection from one panel to the next. As we know from Figure 4.9b, it is shaped as a quarter circle. It is also assumed that the reflectance rate of the façade is 100%, as we only want to understand the behavior from the geometry, omitting any optical properties. Additionally, it is assumed that the rays hitting the façade are coplanar (in one plane) with the cross-section of the spherical mirror, ensuring that the formation of the focal points will also be in the same plane as the other two objects.

Lastly, in this 2D model, primary reflection (the reflected rays from incoming rays) will only be considered, or in other words, any reflection ray that gets reflected again is neglected, assuming it does not carry enough power. This is done to avoid complications in the model and is based on the understanding that, in a 3D situation, secondary reflections are not likely to occur due to the solar altitude causing the reflection to be directed downwards and therefore not reaching the façade again after reflection.

This method is similar to that of basic optics, in which from paraxial rays hitting a spherical in a direction parallel to the optical axis, the focal point will be located halfway between the center of the sphere and the surface mirror, as can be seen in Equation 4.1 and Figure 4.9a.

$$f = \frac{R}{2} \tag{4.1}$$

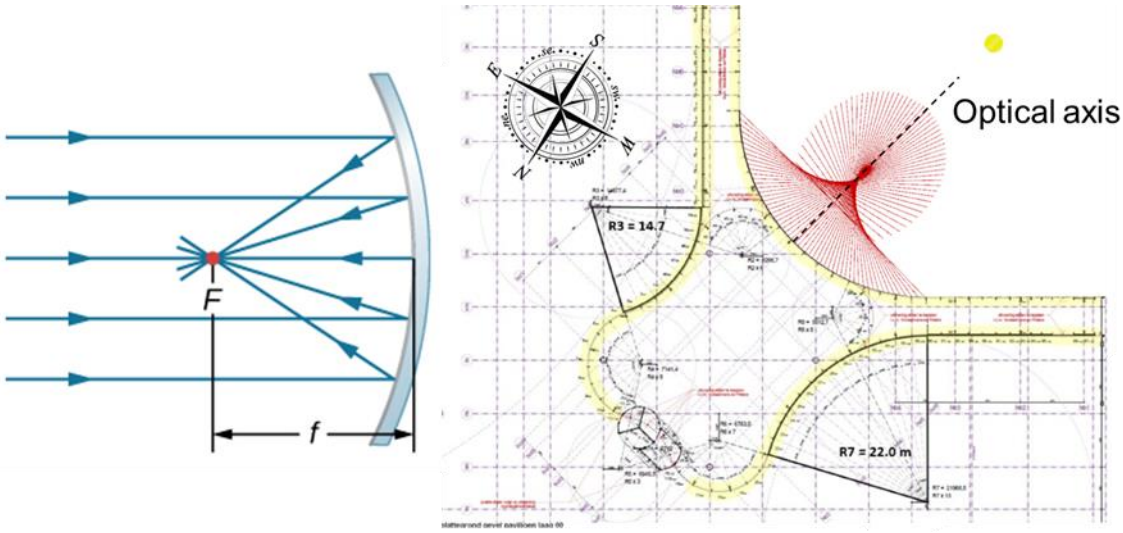

(a) (b)

Figure 4.9 (a) focal point location of a spherical mirror (Ling et al., 2016)(b) focal point of the Amsterdam UMC façade

In this 2D model, the angle of the collimated beam from the optical axis of the 2D mirror will be varied, as can be imagined in Figure 4.10a. Then, to measure the intensity at the focal point, a mesh with an area of 4 square meters, as seen in Figure 4.10b and constrained by green lines, will be used to count the dots formed by the intersections of two crossing reflection rays. To simplify the model, all 2D mirrors (quarter-spherical mirror as seen above, half-spherical mirror, half-elliptical mirror, etc.) will have the same arc length of 100π meters.

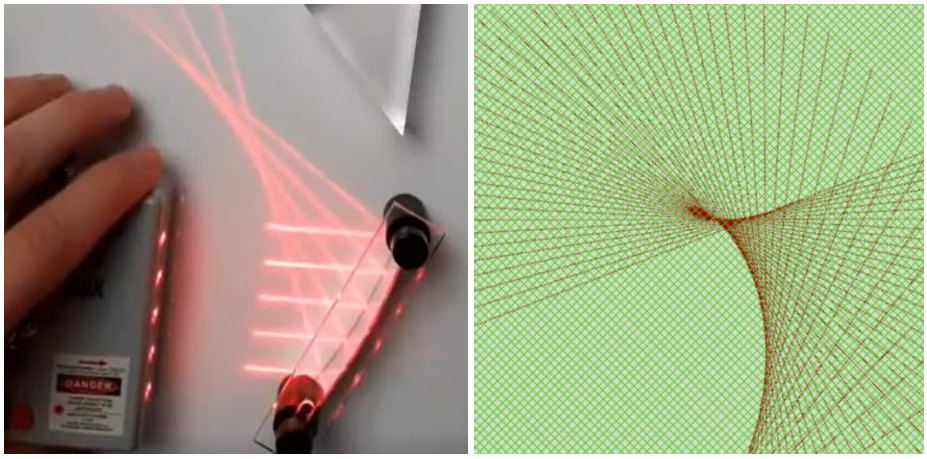

(a) (b)

Figure 4.10 (a) Collimated beam attacking from arbitrary angle from optical axis (The Grimes Teacher, 2023) and (b) calculating the number of intersection between two reflection rays or more

4.3. 3D Numerical Modelling Process

After obtaining the measurement data as a means of calibration and validation for the numerical model, the numerical model itself can be created. The model is initially created to reenact the phenomenon of solar convergence on Friday, 8 March 2024, that occurred in the parking lot of Amsterdam University Medical Center. In short, the numerical model follows the steps outlined in this chapter.

4.3.1. Determining the Location

In order to reconstruct the phenomenon correctly, the exact geographic position of the building has to be determined. By simply right-clicking on the location of interest within the Google Earth website and choose "Get info", data such as the coordinates (latitude, longitude, and altitude/elevation) can be obtained, as shown in Figure 4.11.

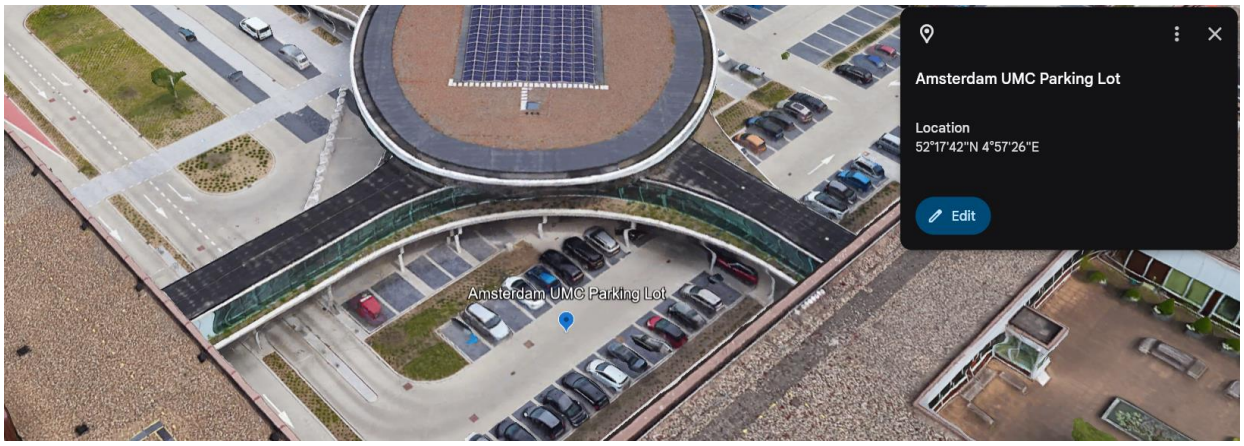

*Figure 4.11 Geographical information of the Amsterdam UMC from Google Earth (*Google Earth*, 2022)*

4.3.2. Adjustment of the Sunpath Diagram

To obtain the correct sunpath representative to the location of the building, adjustment is necessary. Adjustment is made by utilizing the coordinates (latitude, longitude, and altitude) of the building we obtained earlier. However, conversion of both latitude and longitude from degrees, minutes, and seconds (DMS) into decimal degrees (DD) using the Equation 4.2 is needed.

$$decimal\ degrees = degrees + \frac{minutes}{60} + \frac{seconds}{3600} \qquad 4.2$$

In this case, the latitude and longitude of the Amsterdam UMC's parking lot will be 52.2952 and 4.9572, respectively, with the elevation remains -3.59 m. Write down the coordinates that have been converted to DD into the "DF Create EPW" component, as seen in Figure 4.12.

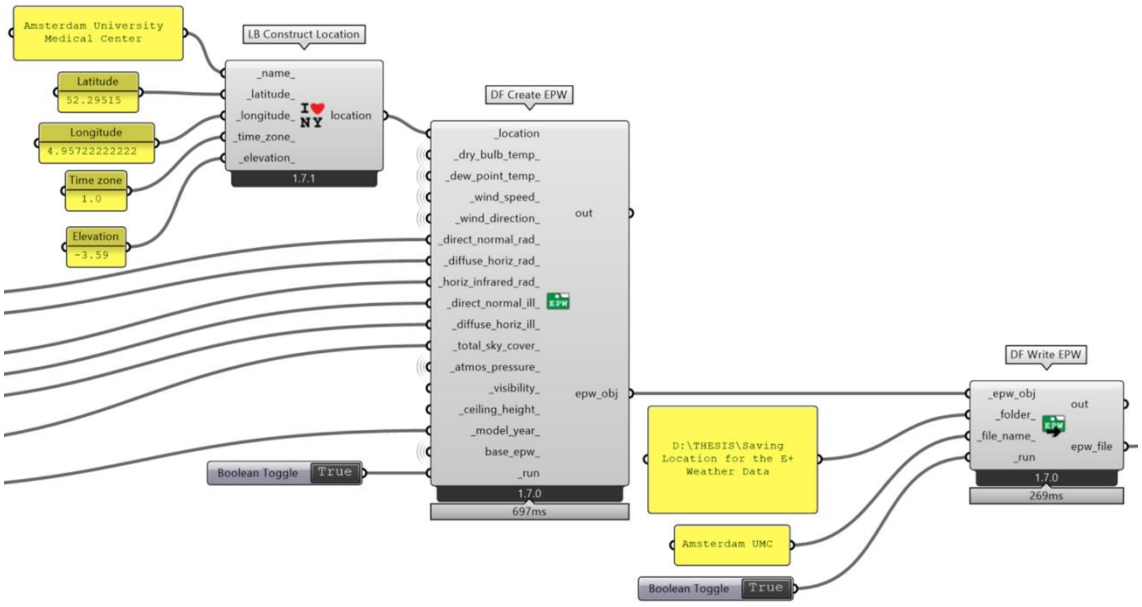

Figure 4.12 Newly adjusted data

As a side note, make sure to write the time zone of the location when daylight saving time is not applied.

4.3.3. Downloading the Weather Data

Since the developed script should be useful for the assessment of any arbitrary building, meteorological data is needed to correctly combine the building's geometry and the solar radiation at its particular location on Earth. In case independent measurements have not been done, which is most likely the case, we can obtain the weather data by downloading weather data for a specific location and specific times, days, and years from the Copernicus Atmosphere Monitoring service.

Specific Year Meteorological Data

Specific Year Meteorological Data can be obtained from the Copernicus Atmosphere Monitoring Service (CAMS) website. Make sure to download the data in CSV format with a time step of every 1 minute. From CAMS website, estimated values of BHI, BNI, DHI, and GHI during under cloud-free conditions (clear sky) can be obtained (CAMS Radiation Service, 2020). These data can show the true potential of converged solar reflection effects for any building. However, in this thesis, the actual values of radiation that occurred on 8 March 2024 were used since it was necessary to reconstruct the phenomenon exactly as it happened during the on-site measurement rather than looking for the worst effect possible.

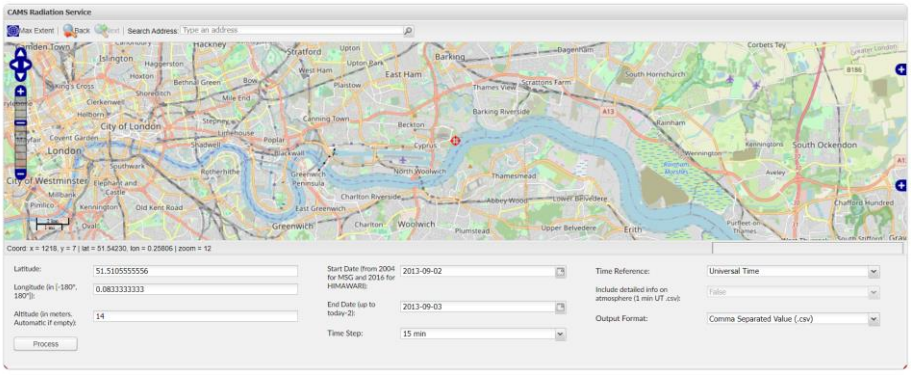

Figure 4.13 The interface of CAMS Radiation Service website (CAMS Radiation Service, 2024)

The csv data from the CAMS radiation service has to be saved as an Excel file in which the sequence of the columns is formated exactly as can be seen in the Figure 4.15 as an example. From left to right, the columns are:

1. Time

   Time indicated in this table follows the standard time (civil time) in a certain day of interest which are formatted in a 24-hour format.

2. Hour of the year (HOY)

   HOY corresponds to the hours and days of interest within a year. In a common year, there are 8759 hours, while a leap year has 8760 hours. However, the Ladybug package standardizes its components so that the last Day of the Year (DOY) and Hour of the Year (HOY) are set to 365 and 8759.98333 (31 December 23:59:00), respectively, for every year. The equation to calculate HOY is provided in Equation 5.2.

$$HOY = (DOY - 1) \times 24 + hour\ of\ the\ day + \frac{minute\ of\ the\ day}{60} \qquad 4.3$$

   With DOY being the day of the year which the calendar could be easily found on the internet.

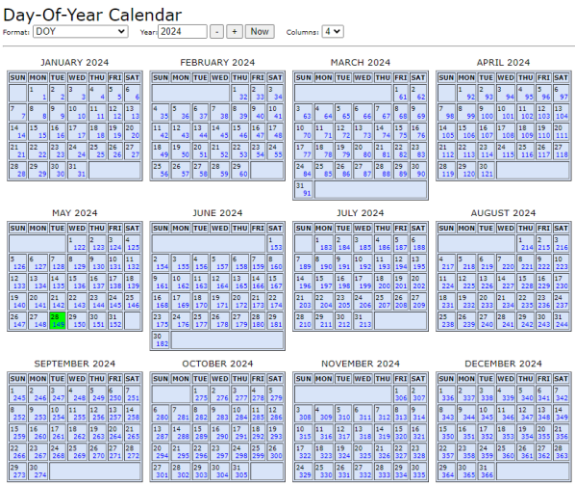

Figure 4.14 Day of the year calendar (NOAA Earth System Research Laboratories, 2024)

For example, the HOY of 8 March at 10:47:00, 15:00:00 are,

$$HOY = (67 - 1) \times 24 + 10 + \frac{47}{60} = 1594.783$$

$$HOY = (67 - 1) \times 24 + 15 + \frac{0}{60} = 1599$$

3. Solar irradiance data

Columns B to F list the data for global horizontal irradiance (GHI), beam horizontal irradiance (BHI), diffuse horizontal irradiance (DHI), and beam normal irradiance (BNI). Note that the data obtained from CAMS radiation is provided in Wh/m^2. To convert this to W/m^2, it is necessary to multiply the values by 60, only if the data is collected every minute.

4. Solar irradiance data

If the reflection is predicted to land on a shadowed ground level , where direct sunlight is blocked by nearby objects (such as buildings, trees, etc.), the irradiance under the shadow in column G will be used to measure the actual irradiance received at the ground level, in addition to the irradiance from the reflection of the façade. Conversely, if the converged reflection lands outside of the shadowed area, then GHI will be added during the measurement of the solar reflection.

From the Amsterdam UMC measurement, irradiance deep inside the shadowed area was observed to be approximately 16% of the GHI on a clear day. However, Hess and Koepke discussed that the influence of sky obstructions, caused by blockages in the immediate area such as mountains, trees, umbrellas, and street canyons, can reduce UV irradiance to 30%, while it increases by 10% if there are reflections from the snow present (Hess & Koepke, 2008). Essentially, the extent to which the reflection penetrates a shadowed area and the amount of diffuse light reaching the same location results in varying irradiance levels under the shadow. A range of 16% to 30% of the GHI is considered reasonable.

	A	B	C	D	E	F	G
1	Time	HOY	GHI	BHI	DHI	BNI	Irradiance under the shadow
2	10:45:00	1594.750000	534.24	416.862	117.378	800.544	#N/A
3	10:46:00	1594.766667	535.194	417.744	117.45	801.078	#N/A
4	10:47:00	1594.783333	536.136	418.614	117.522	801.6	36.79257473
5	10:48:00	1594.800000	537.066	419.472	117.594	802.116	36.79257473
6	10:49:00	1594.816667	537.984	420.318	117.66	802.626	37.52388705
7	10:50:00	1594.833333	538.884	421.152	117.732	803.124	36.79257473
8	10:51:00	1594.850000	539.772	421.98	117.798	803.616	37.14562206
9	10:52:00	1594.866667	540.648	422.79	117.858	804.102	44.9
10	10:53:00	1594.883333	541.506	423.588	117.924	804.582	46.46098579
11	10:54:00	1594.900000	542.352	424.368	117.984	805.05	46.81029256
12	10:55:00	1594.916667	543.186	425.142	118.044	805.518	47.08453468
13	10:56:00	1594.933333	544.008	425.904	118.098	805.974	47.54160488
14	10:57:00	1594.950000	544.812	426.654	118.158	806.418	47.90726103
15	10:58:00	1594.966667	545.604	427.392	118.212	806.862	45.89615217
16	10:59:00	1594.983333	546.378	428.112	118.266	807.3	43.3491679
17	11:00:00	1595.000000	547.146	428.826	118.32	807.726	42.61785558
18	11:01:00	1595.016667	547.89	429.522	118.368	808.146	41.58
19	11:02:00	1595.033333	548.628	430.212	118.416	808.554	50.97
20	11:03:00	1595.050000	549.348	430.884	118.464	808.962	52.45274533
21	11:04:00	1595.066667	550.056	431.544	118.512	809.358	45.51788718
22	11:05:00	1595.083333	550.752	432.192	118.554	809.754	42.97090291
23	11:06:00	1595.100000	551.43	432.834	118.602	810.138	42.61785558
24	11:07:00	1595.116667	552.096	433.452	118.644	810.516	43.3491679
25	11:08:00	1595.133333	552.75	434.064	118.68	810.882	42.61785558
26	11:09:00	1595.150000	553.386	434.664	118.722	811.248	42.61785558
27	11:10:00	1595.166667	554.01	435.252	118.758	811.602	42.61785558

Figure 4.15 Specific year weather data input

For the reenactment of the solar convergence occurrence that happens on Amsterdam UMC on Friday, 8 March 2024, the graph showing the changes of GHI, BHI, DHI, and BNI can be seen in Figure 4.16.

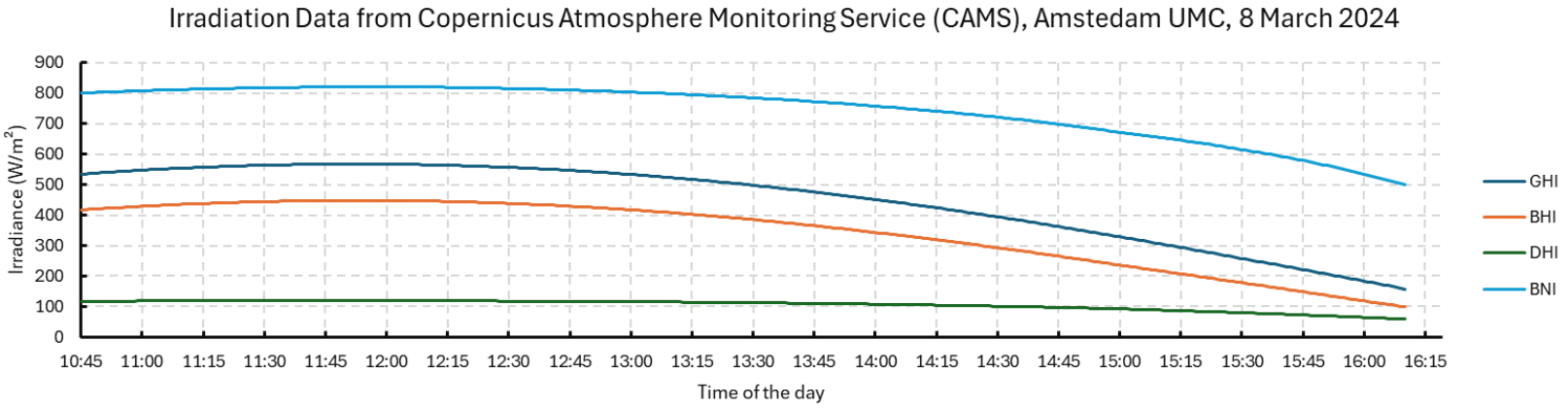

Figure 4.16 Irradiance Data of Amstedam UMC Building, 8 March 2024

4.3.4. Generating the Source Points of Solar Rays

In order to simulate the reflected solar rays from the façade, which carry a certain amount of energy, generating a sufficient number of source points in the sky to “shoot” solar rays is one of the most important aspects to consider. Both the number of source points and their density will affect the simulation time of the program. Determining the sufficient density of the source points will be discussed in Chapter 5 | . In Figure 4.17 and Figure 4.18, the sufficient number of source points is shown, in which the source points attributed to the solar rays that hit the façade, indicated by the blue dots, are all present and not cropped out of the plane of the source points. The white dots represent the solar rays that directly hit the ground, while the red dots represent solar rays that are blocked by objects before reaching the façade.

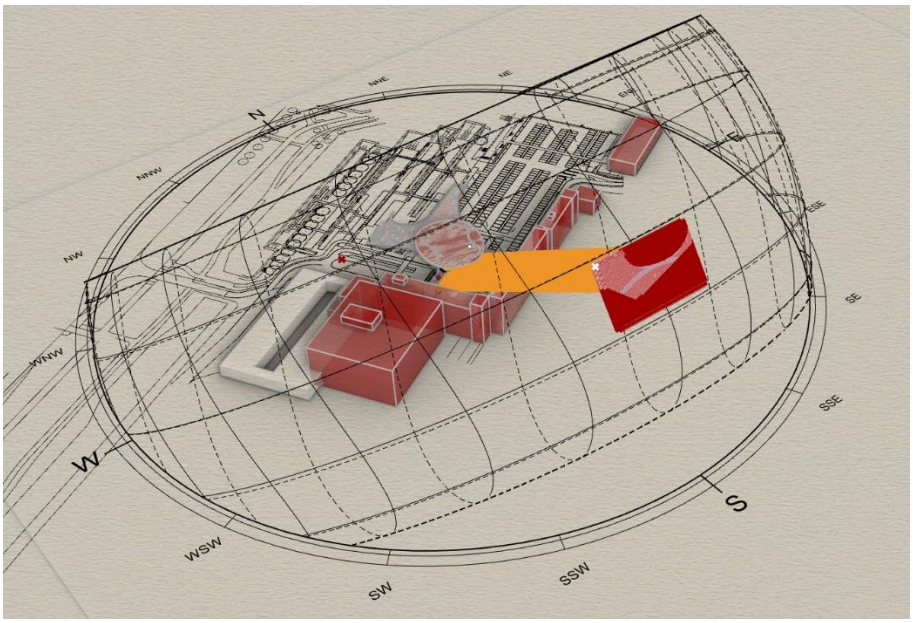

Figure 4.17 Sunrays from the source points

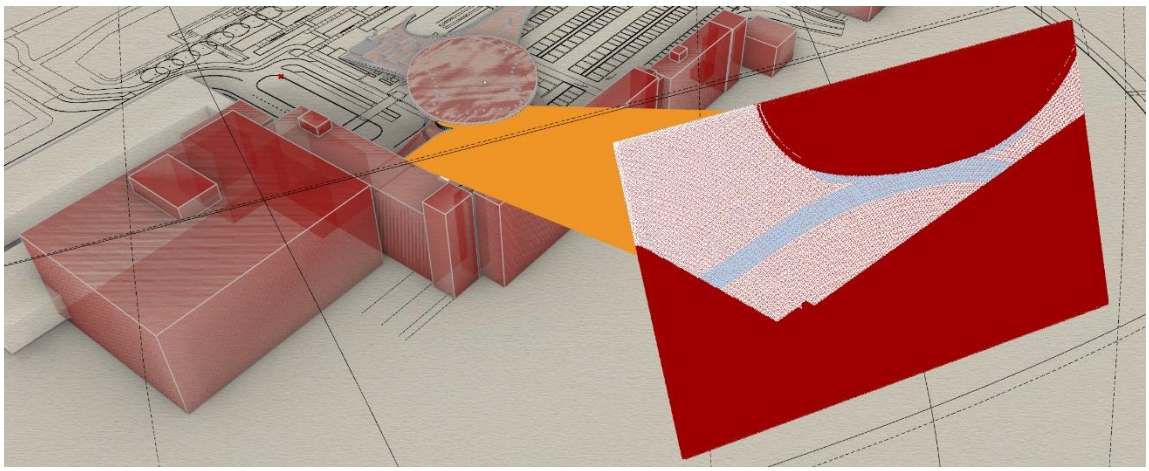

Figure 4.18 Example of a sufficient number of source points

The number of source points corresponds to the discretization size of the sky. Each source point represents a patch of a sky with a finite area (A_i). As can be seen in Figure 4.20, more source points within the same total area ($\sum_{i=1}^{n} A_i$) mean a more refined mesh size of the sky. One solar ray carries a certain amount of solar power (P_i) obtained from the beam normal irradiance (G_{Bn}) and several other factors such as the circumsolar diffuse radiation and horizon brightening, multiplied by the finite area its source point represents. In this algorithm, the discretization size of the sky ($a \times a$) will have a positive linear correlation with the size of the mesh on ground level ($(na)^2\ with\ n > 1$).

The finer the sky is discretized, the more intensive computational resources must be reserved. At some point, it will not be worth refining the mesh of the sky if the result does not change significantly while the computing time increases unreasonably. Therefore, sufficient number of source points and solar rays will help make the code run faster. The mesh size and the amount of them can be set up in the algorithm numbered 4 as can be seen in Figure 4.19.

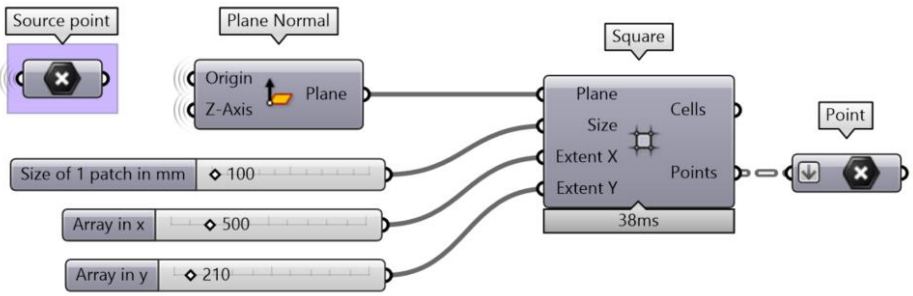

Figure 4.19 Algorithm to adjust the size and the amount of the mesh in the sky

However, when assessing the case of converged solar reflection of the Amsterdam UMC building, the use of a larger mesh proved to be very helpful for quickly and qualitatively assessing the situation without the immediate need to know the accurate value of the irradiance. This approach also facilitated explanations and discussions during meetings, as the fast calculations and visualizations provided significant advantages.

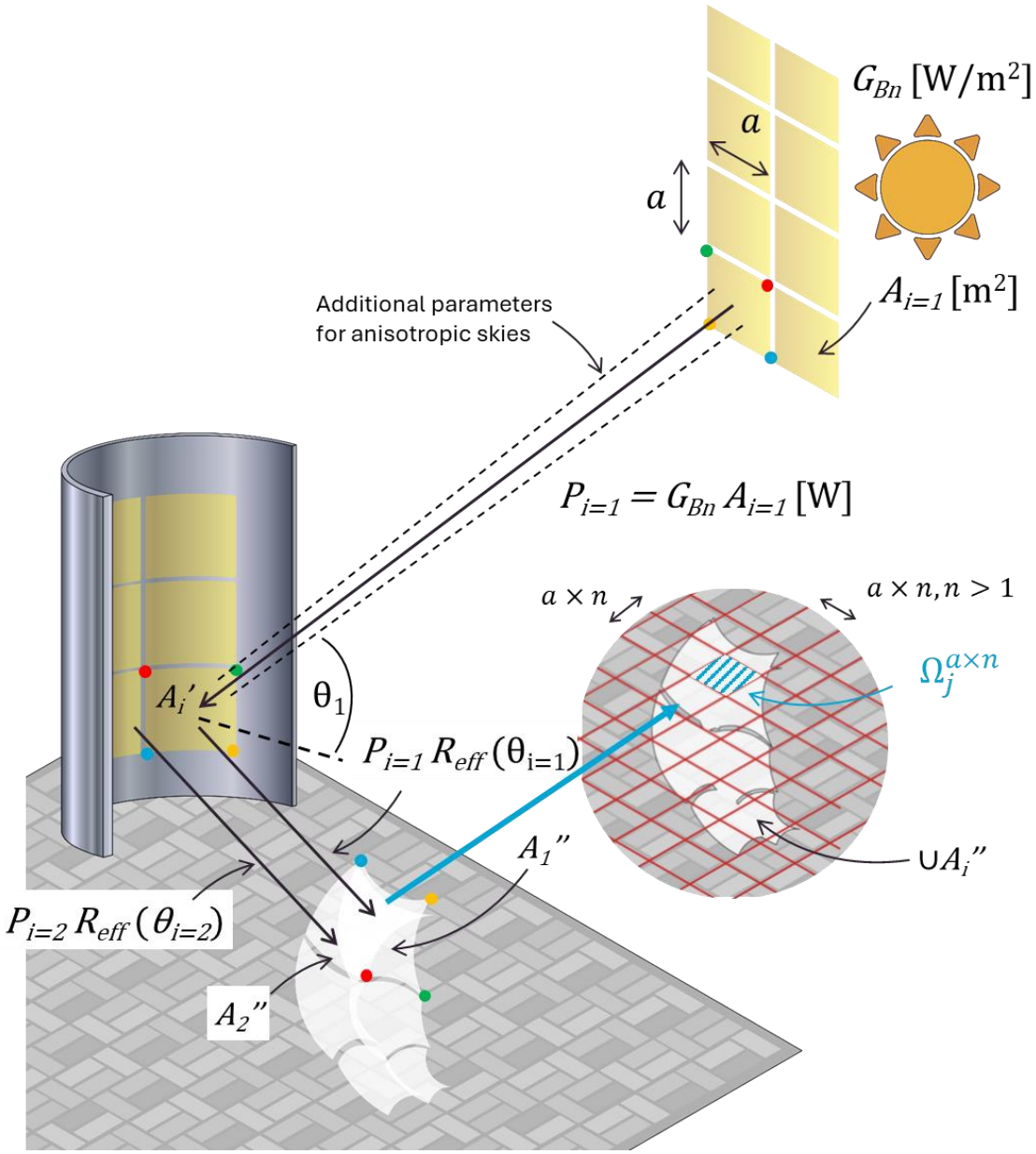

Figure 4.20 Algorithm scheme of the program

4.3.5. Replication of the Reflectance Rate Function

The algorithm below replicates the reflectance rate as a function of the angle of incidence ($R_{eff}(\theta_i)$). The user only needs to input the value of the reflectance rate perpendicular to the glasses, after which the function will calculate the reflectance rates for other angles of incidence. The complete derivation of the function will be discussed in the Results and Discussion Chapter.

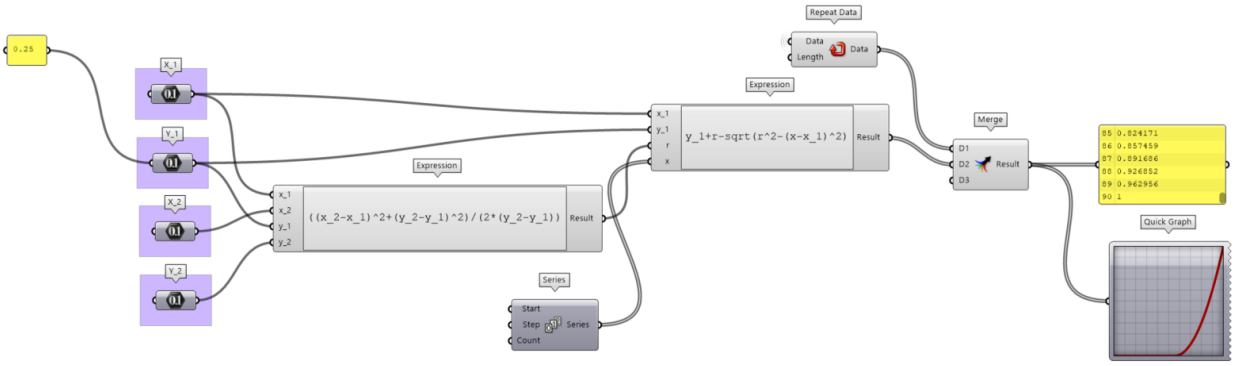

Figure 4.21 Reflectance Rate of Circular Arc Function

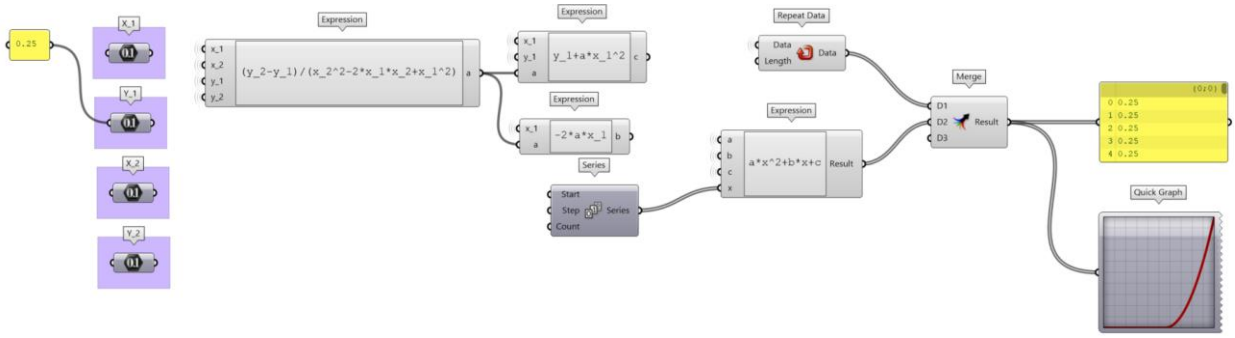

Figure 4.22 Reflectance rate of parabolic and circular arc function

4.3.6. Blockage of the Solar Ray

The script provides a way in which solar rays could be blocked by buildings or objects in general before reaching the façade and blocked again if there are obstacles preventing the solar rays reflected into the ground level. User needs to put inside the mesh that will block the solar rays in the algorithm group number 7 and number 13 for the first case and the latter case, respectively.

4.3.7. GHPython Script to Create Angle of Reflection

In this algorithm, a code to obtain the direction (unitized vector) of reflection after bouncing off of a façade in a 3 dimensional space is created, as can be seen in Listing 4.1. The code is provided below and the illustration to the code can be seen in Figure 4.23.

```
"""Provides a scripting component.
    Inputs:
        x: The x script variable
        y: The y script variable
    Output:
        a: The a output variable"""

__author__ = "satri"
__version__ = "2024.03.21"

import rhinoscriptsyntax as rs
import Rhino.Geometry as rg

def RunScript(sunVec, normVec):
    # Check if either of the vectors is null
    if sunVec is None or normVec is None:
        return None

    # Normalize the vectors
    sunVec.Unitize()
    normVec.Unitize()

    # Calculate the dot product
    dot = rg.Vector3d.Multiply(sunVec, normVec)

    # Calculate the reflection vector
    reflVec = sunVec - (2 * dot * normVec)

    return reflVec

reflection_vector = RunScript(sunVec, normVec)

reflVec = reflection_vector
```

Listing 4.1 GHPython script code snippet to recreate a reflection vector on a 3D space

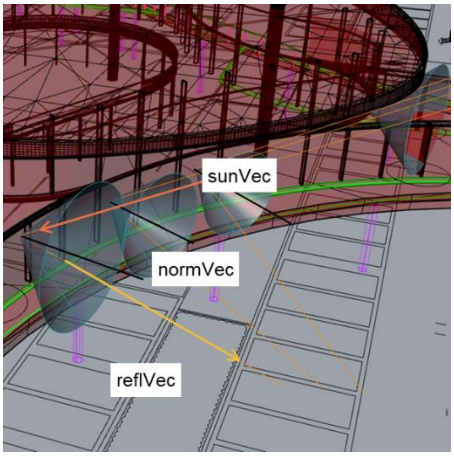

Figure 4.23 Illustration between the vectors hitting the façade

4.3.8. Setting the Mesh Sizes of the Façade

For the simulation, the continuous curved surface of the façade first needs to be discretized into finite planar mesh elements. The setting of these mesh sizes of the façade is important since the reflection vector relies heavily on the normal vector of a certain part of the façade. In order for the algorithm to work, the surface of the façade is turned into mesh, which basically is the approximation to a surface which was constructed from lofting a set of Bezier curve. Bezier curve

itself creates a continuous curve by means of storing the formula to construct the curve. However, improper approximation during meshing process will lead to discrepancies between the actual normal vector from the model. Setting the mesh of the façade to be sufficiently fine will not directly require heavy computational power, therefore it is recommended.

4.3.9. Setting the Mesh Size of the Measuring Plane

As illustrated in Figure 4.20, the mesh size of the measuring plane is designed to exhibits a positive linear correlation with the mesh size of the sky, in which the reason for that will be discussed in the uncertainty from the setting of the measuring mesh size. Essentially, to obtain the shape of the final reflection that falls onto the ground level, each mesh from the sky dome (A_i) is projected twice. First, the mesh is projected onto the façade surface along the direction of incidence vector, resulting in the first distorted shape ($A_i{}'$). Then, this distorted shape is projected again onto the ground level to obtain the individual reflection shapes ($A_i{}''$). All the individual reflection shapes are merged using the "Region Union" component to obtain the final reflection shape on the ground ($\cup A_i{}''$). The final reflection shape on the ground is then rectangularly discretized ($\Omega_j^{a\times n}$) with a total area of $(na)^2$ or less $(with\ n > 1)$. Finally, to obtain the irradiance of the reflection that falls and converge onto a certain location on the ground (G_j^{rc}), the cumulation of solar power that hit the ground after reduced by the reflectance rate of the façade ($\sum_{i=1}^{n} P_i \times R_{eff}(\theta_i)$) will be divided by its corresponding surface area of the measuring plane, as can be seen in Equation 4.4. The explanation above are illustrated in Figure 4.24.

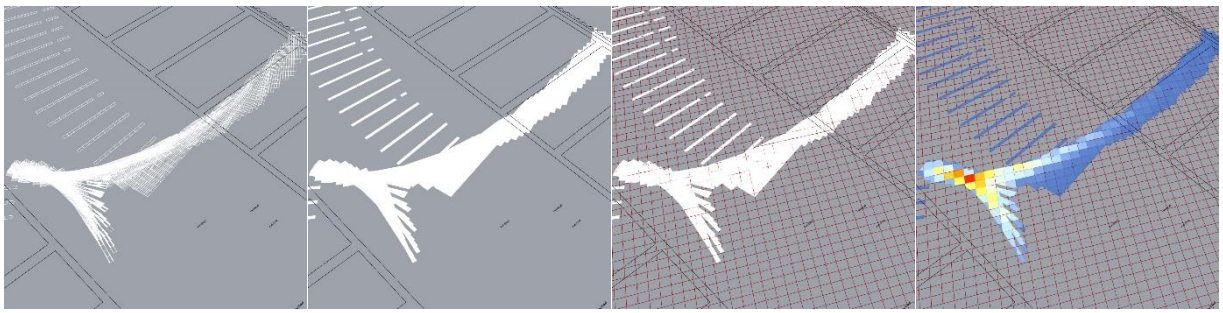

(a) (b) (c) (d)

Figure 4.24 The irradiance measurement process: (a) individual reflection shapes projected onto the ground (b) unionized reflection shape (c) discretization of the clumped reflection shape (d) irradiance measurement based on the area of discretized shape

$$G_j^{rc} = \frac{\sum_{i=1}^{n} P_i \times R_{eff}(\theta_i)}{\Omega_j^{a\times n}(\cup A_i{}'')} \qquad 4.4$$

4.3.10. Visual Check Prior to Calculating the Measurement

Prior to measure the solar convergence irradiance on the ground, it is wise to do visual check comparing the shape of the reflection from the model to the real reflection, if such figures exist. Figure 4.25 to Figure 4.29 illustrate the similarity in shapes between the model to the real reflection.

Figure 4.25 Similarity of the shape Amsterdam UMC Solar Convergence 12:25 CEST

Figure 4.26 Similarity of the shape Amsterdam UMC Solar Convergence 13:58 CEST

Figure 4.27 Similarity of the shape Amsterdam UMC Solar Convergence 14:53 CEST

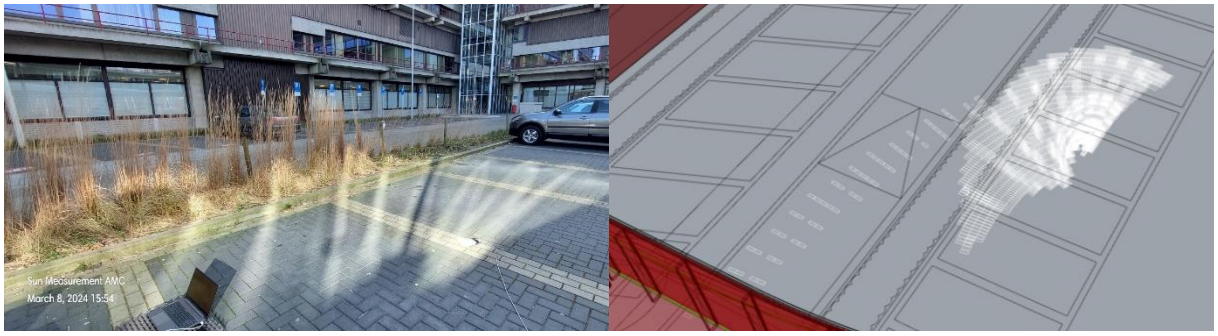

Figure 4.28 Similarity of the shape Amsterdam UMC Solar Convergence 15:54 CEST

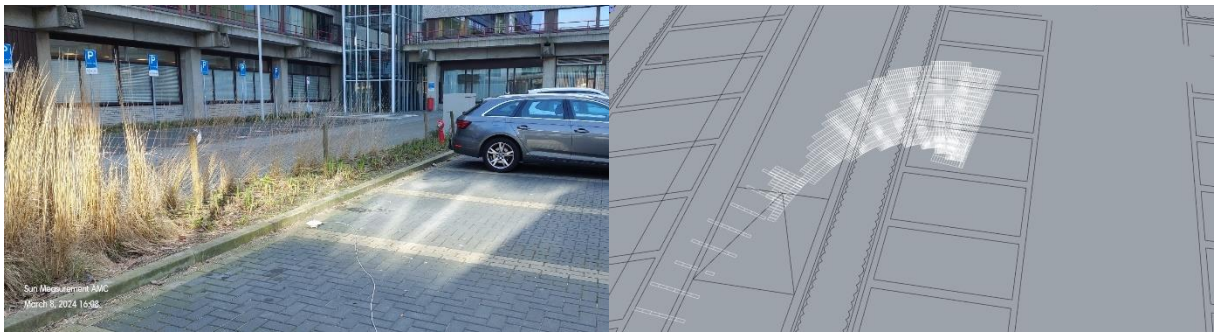

Figure 4.29 Similarity of the shape Amsterdam UMC Solar Convergence 16:08 CEST

4.3.11. GHPython Script to Measure the Irradiance on the Ground

To measure the solar convergence irradiance at the ground level, a component from GHPython script was developed to calculate the power from several solar rays ($\sum_{i=1}^{n} P_i \times R_{eff}(\theta_i)$) that land on a discretized measuring surface on the ground, located with index j ($\Omega_j^{a\times n}(\cup A_i'')$). The complete script for this purpose can be seen in Appendix B and the algorithm can be seen in Figure 4.31.

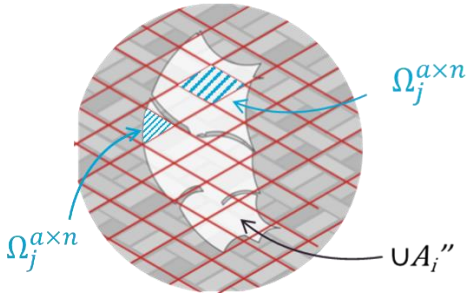

Figure 4.30 Illustration of the discretized measuring surface (Ω_j) with an area of (a×n)² or smaller

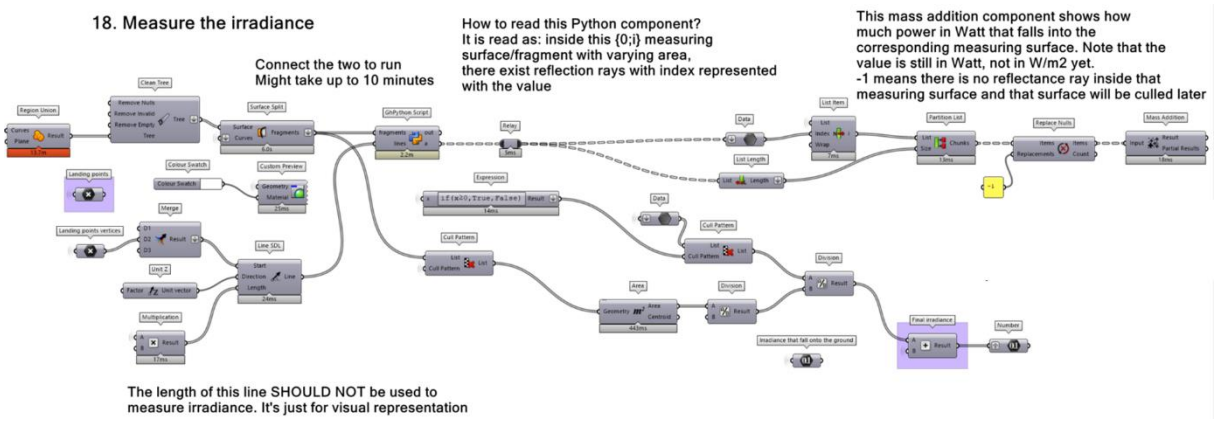

Figure 4.31 The algorithm to measure the irradiance

4.3.12. GHPython Script to Check for the Irradiance At Arbitrary Locations

Other than observing the maximum irradiance at which the focal point is located, user can also check for the irradiance at any location with the algorithm presented in Figure 4.32 and the script is provided in Appendix C.

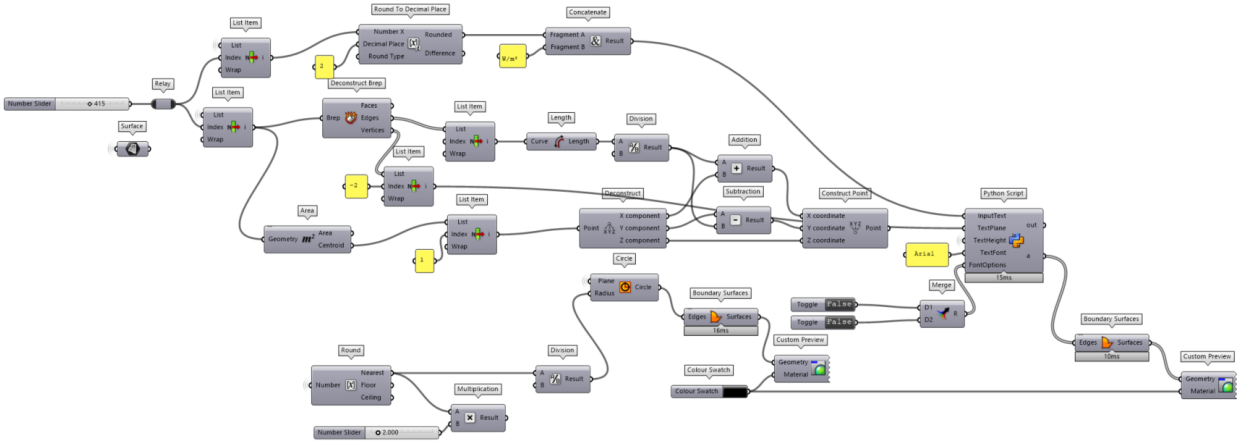

Figure 4.32 Algorithm to check irradiance at arbitrary location

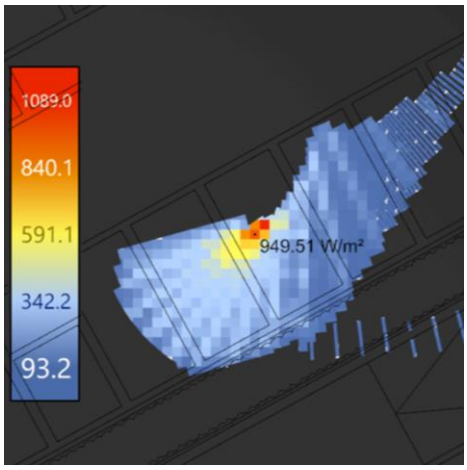

Figure 4.33 Irradiance measured at arbitrary location

5 | Results and Discussion

5.1. Replication of the Fresnel's law of Effective Reflectance Rate Function

As stated in Chapter 3.7 above, the effective reflectance rate for semi-transparent non-magnetic media varies with 3 parameters, which are the refractive index of the medium from which the light is coming (n_1), the refractive index of the medium into which the light is entering (n_2), and the angle of incidence. Even though the formula seems to be straightforward to employ, usually a glass façade is not made out of a single glass layer, especially for buildings that are located in the four seasons countries, as they need to adjust the indoor temperature according to the outdoor temperature fluctuations due to seasonal changes. This also holds true for buildings located in extremely cold conditions, such as in higher latitudes, or in extremely hot conditions, such as in arid or desert regions.

In addition to regional constraints, safety concerns also play a role in how the materials for glass façades are chosen and stacked. Laminated glass façades, which are typically made from two or more layers of glass bonded with interlayers such as polyvinyl butyral (PVB) or ethylene-vinyl acetate (EVA), are the most common choice.

This multilayer glass façade produces various refractive indices, which are not easy for engineers and architects to calculate analytically. Several software programs, including the WINDOW software from the Lawrence Berkeley National Laboratory (LBNL), provide a way to obtain the graph of the effective reflectance rate of multiple layers of glass by numerically calculating the refractive indices of different configurations of glass panels.

However, WINDOW software requires users to know how to operate another software called OPTICS in order to construct laminated glass, which adds a steep learning curve. The inability to learn both software programs could result in fatal mistakes in the replication of the glass façades and their properties.

For example, looking at the specification document from Saint-Gobain as the façade manufacturer and supplier of the Amsterm University Medical Center, as shown in Figure 5.1, we could seemingly reconstruct the glass façade easily via WINDOW software. Prior to doing so, to ensure that the material properties of the glass façade are correct according to the specification document, another simulation via the Calumen website was conducted. In this simulation, the outdoor reflectance (REE) value listed under the energy factors was found to be of a similar magnitude (25%) only differs 1% from the specification document, as shown in Appendix D.

However, when using the WINDOW software on its own, as seen in Figure 5.2, it is not possible to construct a laminated glass of two PLANICLEAR (6 mm) glasses, one of which is coated with COOL-LITE SKN 165 II and both bonded with PVB Standard (2 × 0.38 mm) without the help of OPTICS software. Essentially, WINDOW software can only be used to set up glass panes separated by different kinds of gaps filled with different gases. The release notes on LBNL's website related to the issuance of different versions of their WINDOW software specifically explain that laminates can only be designed using OPTICS software (Lawrence Berkeley National Laboratory, 2023).

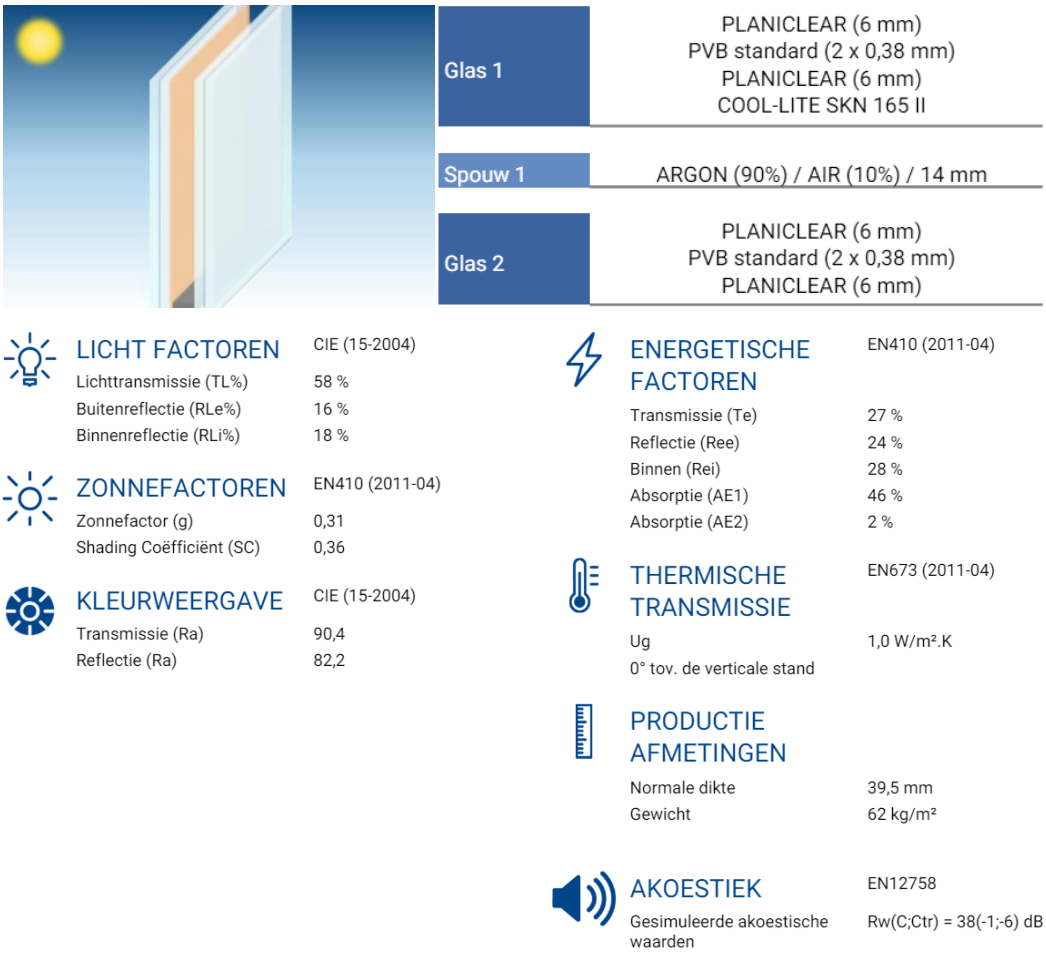

Figure 5.1 The specification document of the AMC south façade

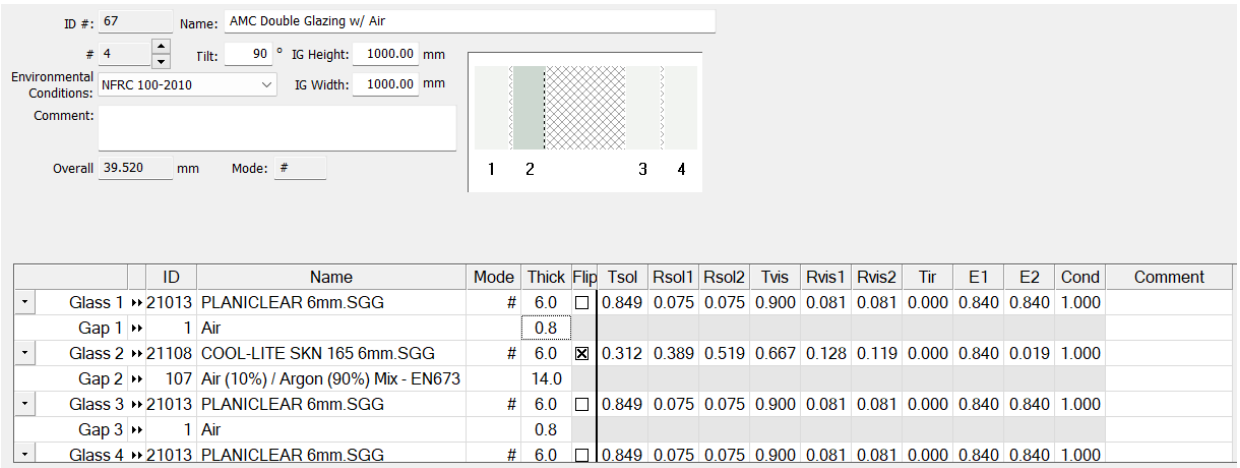

	ID	Name	Mode	Thick	Flip	Tsol	Rsol1	Rsol2	Tvis	Rvis1	Rvis2	Tir	E1	E2	Cond	Comment
Glass 1	21013	PLANICLEAR 6mm.SGG	#	6.0	☐	0.849	0.075	0.075	0.900	0.081	0.081	0.000	0.840	0.840	1.000	
Gap 1	1	Air		0.8												
Glass 2	21108	COOL-LITE SKN 165 6mm.SGG	#	6.0	☒	0.312	0.389	0.519	0.667	0.128	0.119	0.000	0.840	0.019	1.000	
Gap 2	107	Air (10%) / Argon (90%) Mix - EN673		14.0												
Glass 3	21013	PLANICLEAR 6mm.SGG	#	6.0	☐	0.849	0.075	0.075	0.900	0.081	0.081	0.000	0.840	0.840	1.000	
Gap 3	1	Air		0.8												
Glass 4	21013	PLANICLEAR 6mm.SGG	#	6.0	☐	0.849	0.075	0.075	0.900	0.081	0.081	0.000	0.840	0.840	1.000	

Figure 5.2 Reconstruction of the AMC's Southern Façade with WINDOW software

Since it is not possible to create laminated glass in WINDOW software, a model was created in which the PVB that bonds the glasses was replaced with air. However, the REE result from the

software for the southern façade of the AMC building differs significantly from the specification document, where the normal reflection is 37.6%, whereas it should be 24% to 25%, as seen in Figure 5.3. Despite this discrepancy, it correctly captures the behavior described by Fresnel's equation by progressively increasing the reflection rate sinusoidally with the increase in the angle of incidence as seen in Figure 5.4. Changing the gas infills inside the cavity does not affect the refractive index, the reflectance rate, or other optical properties in general because it only changes the thermal properties of the glass façades, such as the U-values.

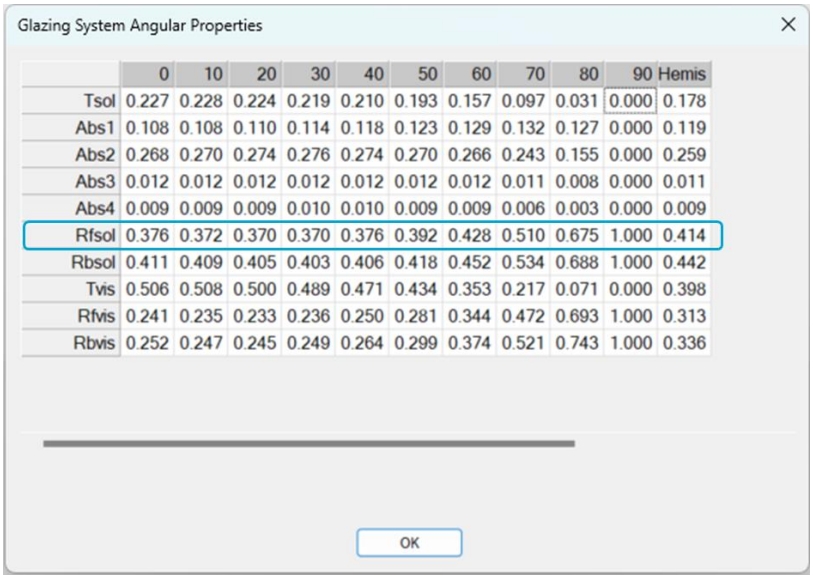

	0	10	20	30	40	50	60	70	80	90	Hemis
Tsol	0.227	0.228	0.224	0.219	0.210	0.193	0.157	0.097	0.031	0.000	0.178
Abs1	0.108	0.108	0.110	0.114	0.118	0.123	0.129	0.132	0.127	0.000	0.119
Abs2	0.268	0.270	0.274	0.276	0.274	0.270	0.266	0.243	0.155	0.000	0.259
Abs3	0.012	0.012	0.012	0.012	0.012	0.012	0.012	0.011	0.008	0.000	0.011
Abs4	0.009	0.009	0.009	0.010	0.010	0.009	0.009	0.006	0.003	0.000	0.009
Rfsol	0.376	0.372	0.370	0.370	0.376	0.392	0.428	0.510	0.675	1.000	0.414
Rbsol	0.411	0.409	0.405	0.403	0.406	0.418	0.452	0.534	0.688	1.000	0.442
Tvis	0.506	0.508	0.500	0.489	0.471	0.434	0.353	0.217	0.071	0.000	0.398
Rfvis	0.241	0.235	0.233	0.236	0.250	0.281	0.344	0.472	0.693	1.000	0.313
Rbvis	0.252	0.247	0.245	0.249	0.264	0.299	0.374	0.521	0.743	1.000	0.336

Figure 5.3 Angular Properties of Southern Façade of AMC Building

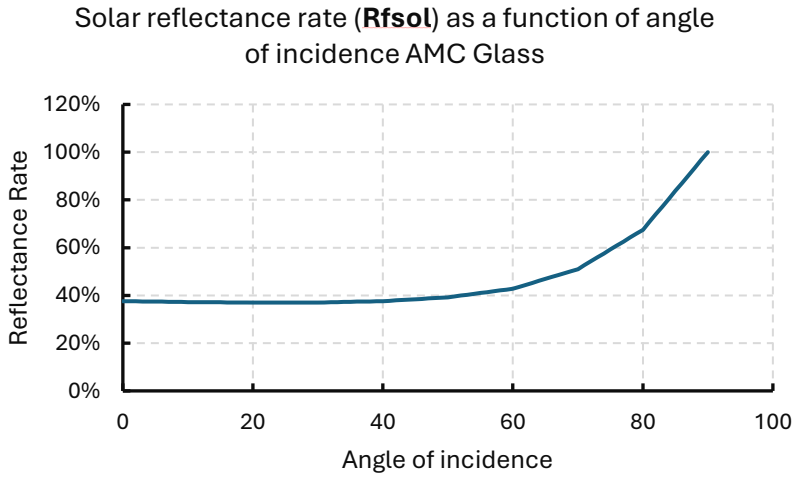

Figure 5.4 Solar reflectance rate hitting from the front side (Rfsol) of the Southern Façade of AMC Building

Simulation of non-laminated glasses, clear glass 6 mm without coating and with coating of SOLARBAN 70XL in WINDOW software result in the same graph as was drawn by Danks et al. as

seen in Figure 5.5. Note that the results from WINDOW software yield graphs that exhibit the same behavior as can be seen in Figure 5.6 and Figure 5.7.

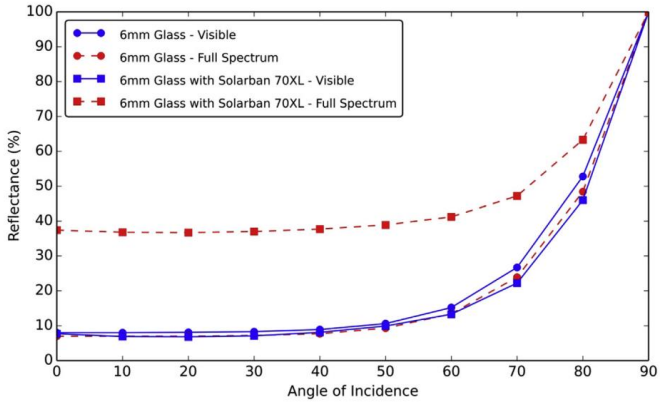

Figure 5.5 Reflectance of a single plane glass for visible light and for full spectrum (Danks et al., 2016a)

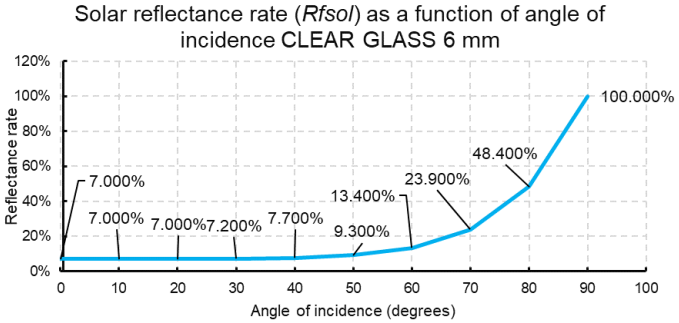

Figure 5.6 Rfsol Clear Glass 6 mm Full Spectrum

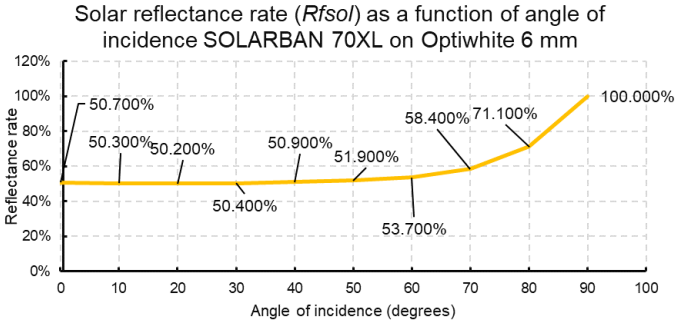

Figure 5.7 Rfsol Clear Glass 6 mm Full Spectrum Coated with SOLARBAN 70XL

The similarity in the shapes of the reflectance rate, despite the differences in the value of the normal reflection, suggests the possibility of creating an approximation function within the Grasshopper script. It is important that the engineers or architects using the script do not need to know the refractive index of the glass façades, which are comprised of different layers of materials stacked

together, and only need to input the normal REE of the glass façade, which is always listed by glass manufacturers in their specification documents based on NEN-EN 410:2011.

After trial and error, the best type of function to replicate the REE is either a parabolic arc function or a circular arc function, both of which only yield slightly different values.

For both functions, the boundary conditions that were used to replicate the REE were:

1. The curve passes through point (x_1, y_1) = (50°, normal REE),
2. The curve passes through point (x_2, y_2) = (90°, 100% REE),
3. The slope at (x_1, y_1) must be zero, as illusrated in Figure 5.8.

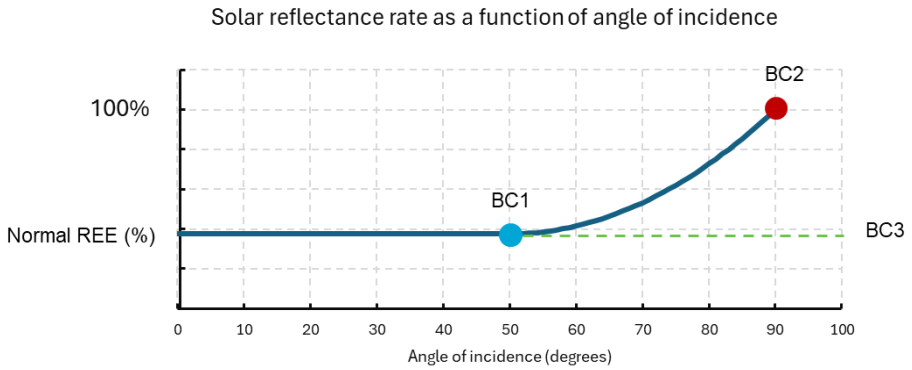

Figure 5.8 Method to approximate the reflectance rate of glass façade

Parabolic Arc

The general equation of parabolic arc is,

$$y = ax^2 + bx + c \tag{5.1}$$

Substituting the boundary conditions, we obtained 3 new equations,

$$\Leftrightarrow y_1 = a{x_1}^2 + bx_1 + c \tag{5.2}$$

$$\Leftrightarrow y_2 = a{x_2}^2 + bx_2 + c \tag{5.3}$$

$$0 = -2ax_1 + b \Leftrightarrow b = -2ax_1 \tag{5.4}$$

Substituting Equation 5.4 into Equations 5.2 and 5.3, coefficients of a, b, and c can be obtained in terms of (x_1, y_1) and (x_2, y_2), which are:

$$a = \frac{y_2 - y_1}{{x_2}^2 - 2x_1x_2 + {x_1}^2} \tag{5.5}$$

$$b = -2ax_1 \tag{5.6}$$

$$c = y_1 + a{x_1}^2 \tag{5.7}$$

The parabolic function to recreate the reflectance rate then would be,

$$\therefore y = \left(\frac{y_2 - y_1}{{x_2}^2 - 2x_1x_2 + {x_1}^2}\right)x^2 + \left[-2\left(\frac{y_2 - y_1}{{x_2}^2 - 2x_1x_2 + {x_1}^2}\right)x_1\right]x + y_1 + \left(\frac{y_2 - y_1}{{x_2}^2 - 2x_1x_2 + {x_1}^2}\right){x_1}^2 \tag{5.8}$$

Circular Arc

The same boundary conditions are used to replicate the REE function of circular arc, except that now the general equation changes, and the interpretation of the boundary conditions defines other parameters. The general equation to a circle with a center of origin in (*h,k*) is:

$$(x - h)^2 + (y - k)^2 = r^2 \tag{5.9}$$

From the first boundary condition, the general equation becomes

$$\Leftrightarrow (x_1 - h)^2 + (y_1 - k)^2 = r^2 \tag{5.10}$$

And from the second boundary condition, the general equation becomes

$$\Leftrightarrow (x_2 - h)^2 + (y_2 - k)^2 = r^2 \tag{5.11}$$

The third boundary condition reveals a valuable information in which the line from point (x_1, y_1) to the center of origin is vertical, in other words, $h=x_1$ and $k=y_1-r$. Plugging in those conditions into Equations 5.10 and 5.11 result in the equation to define the radius,

$$r = \frac{(x_2 - x_1)^2 + (y_2 - y_1)^2}{2(y_2 - y_1)} \tag{5.12}$$

After expressing the equation of the circular arc in terms of y and making sure that the arc always sag downwards, the final equation is obtained,

$$y = y_1 + r - \sqrt{r^2 - (x - x_1)^2} \tag{5.13}$$

$$\therefore y = y_1 + \frac{(x_2 - x_1)^2 + (y_2 - y_1)^2}{2(y_2 - y_1)} - \sqrt{\left(\frac{(x_2 - x_1)^2 + (y_2 - y_1)^2}{2(y_2 - y_1)}\right)^2 - (x - x_1)^2} \tag{5.14}$$

The differences between the two are negligible, therefore, only the replicated graphs from the circular arc are compared with the original reflectance rate function from the WINDOW software, as seen in Figure 5.9.

To check the appropriateness of the function compared to the observed values, the coefficient of determination (R^2) between the two is calculated using Equation below. The full calculation can be found in Appendix E, but in short, the function can represent the observed data with high accuracy, as the coefficient of determination of the graph above, from the upper left to the lower right, is **0.989**, **0.977**, **0.961**, and **0.986**, respectively.

$$R^2 = 1 - \frac{SS_{res}}{SS_{tot}} \qquad 5.15$$

With,

SS_{res} = sum of squares of residuals

$$SS_{res} = \sum_{i=1}^{n} \left(\hat{Y}_i - \bar{Y}\right)^2$$

SS_{tot} = total sum of squares

$$SS_{tot} = \sum_{i=1}^{n} (Y_i - \bar{Y})^2$$

Since the observed data originally follow a sinusoidal function stemming from the Fresnel equation, the approximation from the circular arc function will not be exactly the same. However, it is ensured that the approximation values will be slightly higher than the observed values to prevent underestimation of the solar reflectance. Additionally, the discrepancies between the two will not be excessive, as evidenced by the coefficient of determination from four samples, which consistently have values above 0.95.

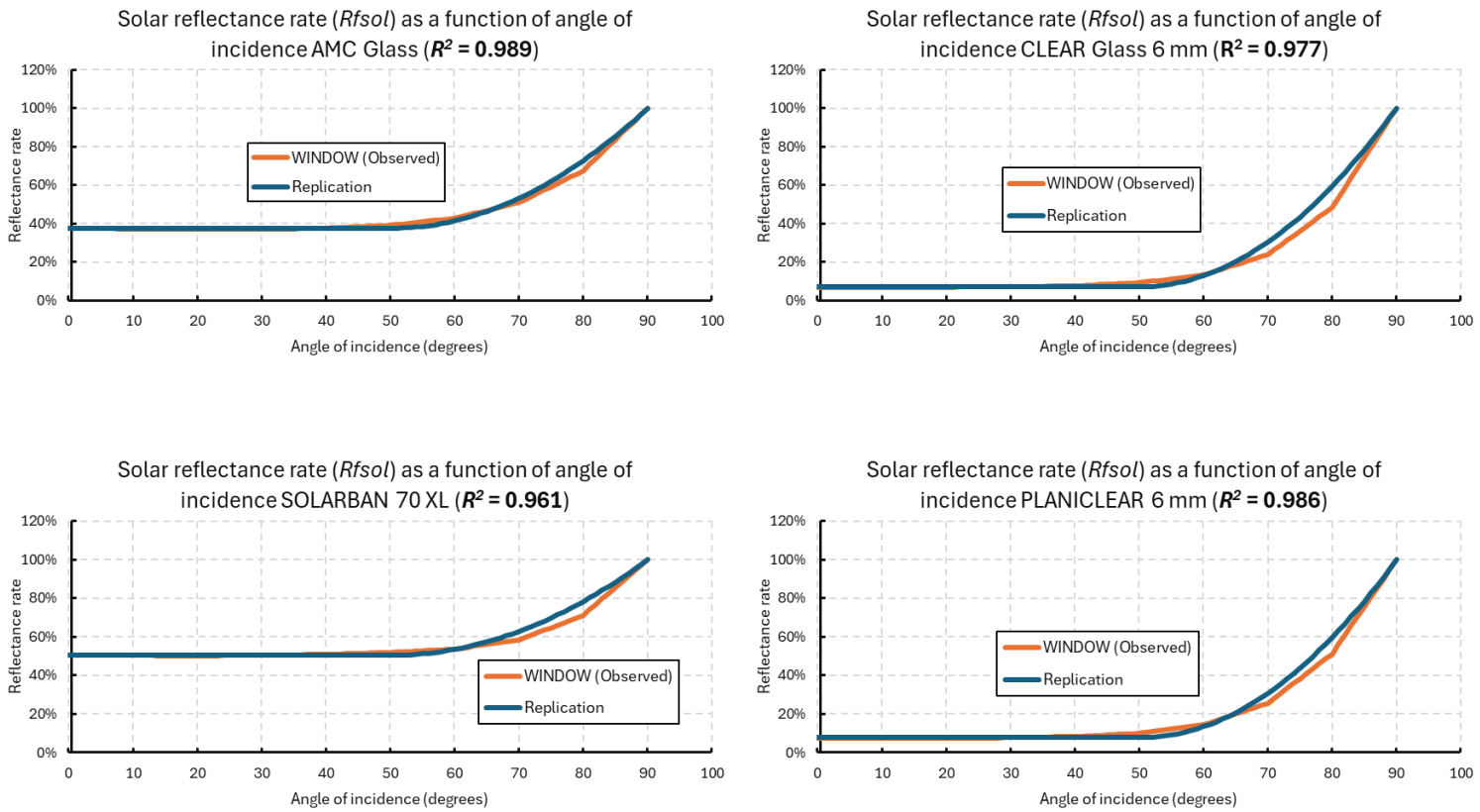

Figure 5.9 Comparison between the value of observed reflectance rates vs. the replications (modelled)

5.2. Solar Convergence Measurement Results and Discussion

After previously discussing the methodology for conducting the solar convergence measurements in Chapter 4, the outcome of the measurement is discussed below.

5.2.1. Weather Conditions

The sky condition during the day of measurement was sunny without any visible overcast nor any precipitation throughout the day. From visual inspection, the clearness index of the sky should be nearing 1. The temperature recorded at 10:25 was 41°F (5°C) and progressively rising but stabilized between 14:25 and 16:25 at 50°F (10°C), as can be seen in the Figure 5.10 below.

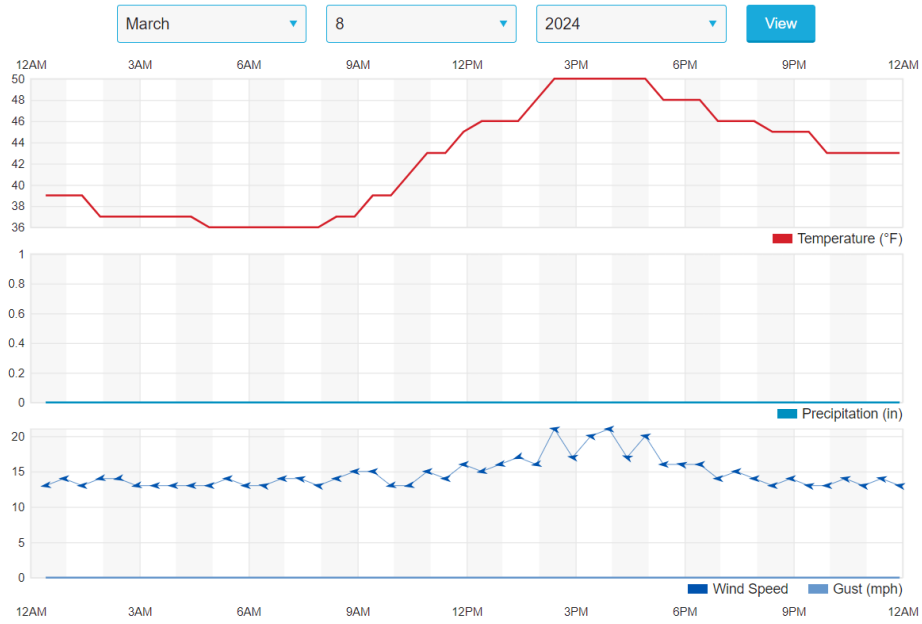

Figure 5.10 Weather conditions measured in Amsterdam Airport Schiphol Station (Weather Underground, 2024)

5.2.2. Technicalities of the Measurements

Values of global horizontal irradiance (GHI) in several locations at different times were measured in SI Units (W/m^2) with two pyranometers. The first pyranometer (to be called the measuring sensor) was used to alternately measure from what are seemingly the focal points (an accumulation of focal lines) to the constituting focal lines of the converged reflections. An example of focal line and a focal point can be seen in the Figure 5.11 and Figure 5.12, respectively. The measuring sensor was moved every time the highest irradiance at a certain point was obtained and no higher irradiance in the readings was seen. The second pyranometer (to be called the benchmark sensor) was used to measure the irradiance in the immediate vicinity of the focal points or focal lines (which most of the time fell on a part of the pavement that was shaded by the nearby main building of the hospital). Both pyranometers recorded the GHI every 15 seconds.

Figure 5.11 Irradiance measurement of one focal line without filter on

Figure 5.12 Irradiance measurement of a focal point with filter on

The specifications of the pyranometers enable them to record a maximum irradiance of 4000 W/m^2. As mentioned earlier, to measure irradiance above the maximum range, a white T-shirt consisting of 2 layers of cloth with a filter of 39.65% was used to filter the incoming solar radiation (total broad-spectrum solar radiation, including visible light, near-ultraviolet, near-infrared radiation, and short-wave infrared radiation). The filter rate was obtained through multiple data collections, as can be seen in Table 5.1. To measure the solar convergence factors, time series GHI data from the Copernicus Atmosphere Monitoring Service (CAMS) were used as the denominator, and the data from the measuring sensor were used as the numerator.

Table 5.1 Filter rate from the white t-shirts

Unfiltered irradiance (W/m^2)	Filtered irradiance (W/m^2)	Filter	Log	Note
70	30	42.86%	From 10:14 to 11:13	Benchmark sensor
50.97	16.47	32.31%		
928.69	358.44	38.60%		Measuring sensor
37.83	16.47	43.54%		
41.58	17.48	42.04%		Benchmark sensor
49.81	18.05	36.24%		
42	18	42.86%	At 11:37:00	
761.62	295.51	38.80%	At 11:25:15	Measuring Sensor
Average		**39.65%**		

The measured irradiances from two sensors are shown in the Figure 5.13 and Figure 5.14 below.

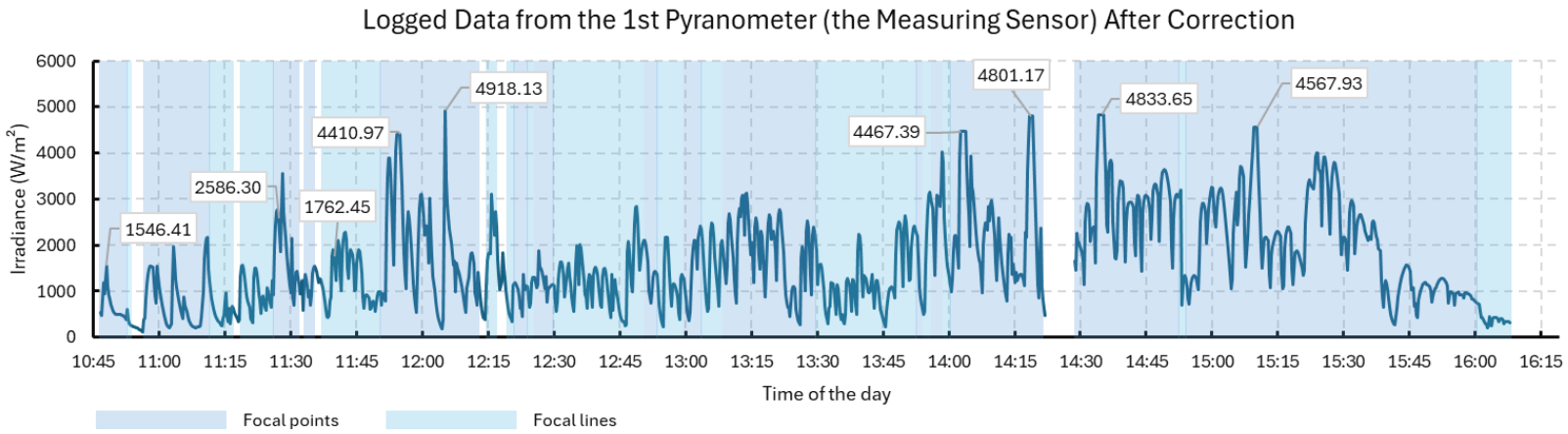

Figure 5.13 Logged data from the 1st pyranometer (the measuring sensor) after correction from the use of filter cloth

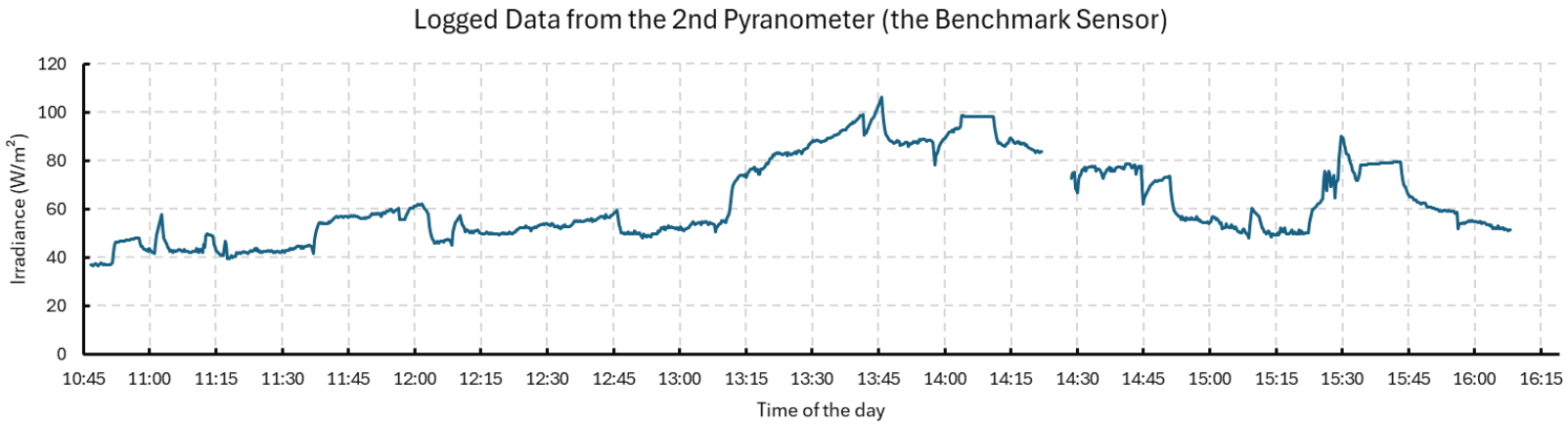

Figure 5.14 Logged data from the 2nd pyranometer (the benchmark sensor, under shadowed building)

The GHI data as denominator to calculate the convergence factors, and the convergence factors are shown in Figure 5.15 and Figure 5.16.

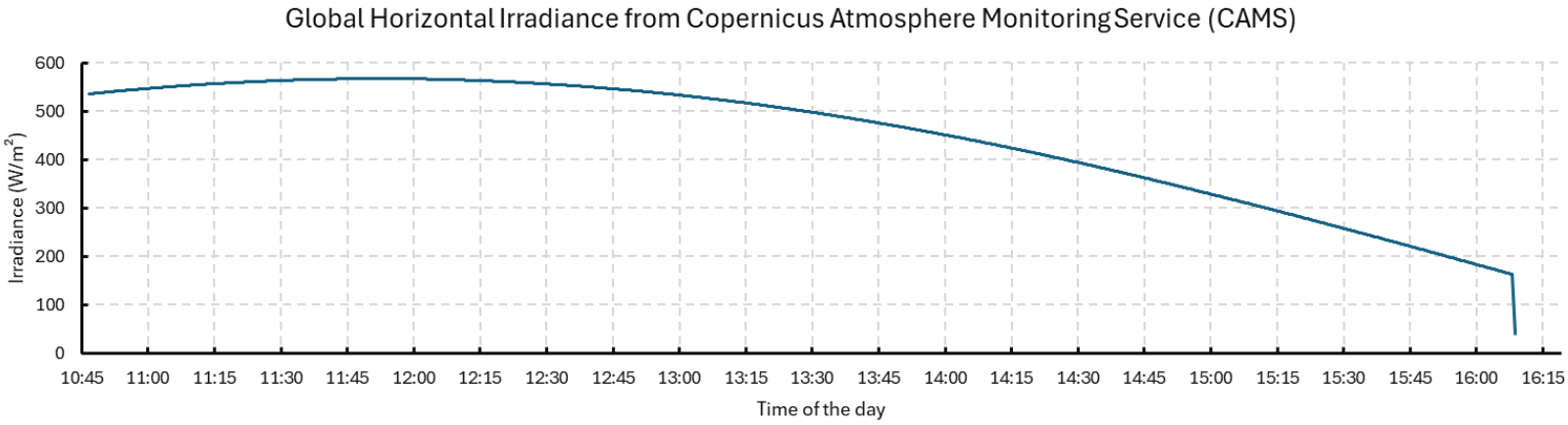

Figure 5.15 Global horizontal irradiance data from CAMS for Amsterdam UMC and vicinity

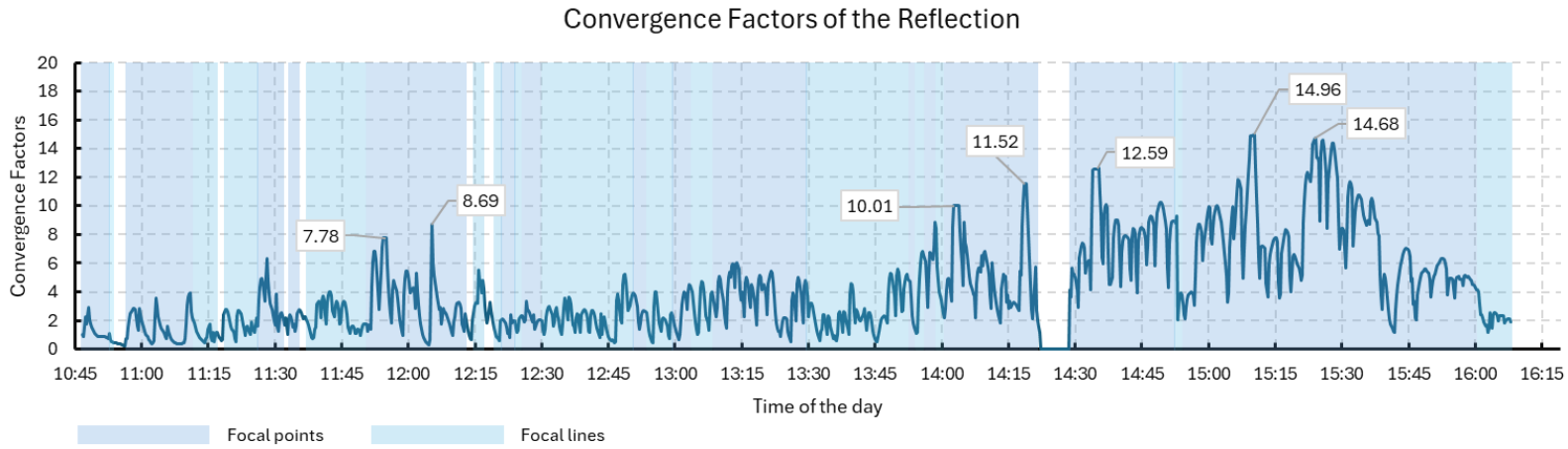

Figure 5.16 Convergence factors of the solar reflection

5.2.3. Conclusion from the Solar Convergence Measurement

Behavior of the focal points

According to the inspection, six focal points with irradiance levels exceeding 4000 W/m^2 were observed throughout the day. These peaks may have been due to the difficulty in accurately tracking the focal points' movements. If the inspector had been able to follow the focal points precisely, the high irradiance levels could have been more evenly distributed throughout the day. Therefore, it is safer to cluster these 6 occurrences into 2 time-wise, most probable continuous occurrences.The focal points that produced irradiance well above 4000 W/m^2 could be determined to have occurred from 11:54:15 to 12:05:15 (just around 10 minutes) and again from 14:02:45 to 15:10:15 (around 1 hour and 10 minutes). The first cluster reached peak irradiance up to 4918.13 W/m^2, while the second cluster reached peak irradiance up to 4833.65 W/m^2. The highes value of convergence factors happened at 15:07 CEST, which is nowhere near the time when peak GHI occurs, this will be further explained in the Chapter of 3D Numerical Modelling Results.

For some of the earliest readings including the first cluster of focal points reaching 4918.13 W/m^2, the magnitude of the irradiances should be taken with careful interpretation, because of:

1. The unstandardized filter rate itself may change with temperature, and since the pyranometers work by calculating the temperature around them, it could alter the approximation.
2. The measurements was conducted mainly without the filter to precisely measure the irradiance of the focal lines. However, when moving to measure the irradiance of the focal points without the filter, most of the time, the peak irradiance from the focal points is indicated by "Error" in the reading due to the peaks being above 4000 W/m^2. Only then that the filter was put on to tone down the readings so that the peak irradiance could be recorded. And then, the recorded irradiance was scaled accordingly to the filter rate to obtain the approximately real peak irradiance. However, the change in reading from "Error" to a calculable and converged/steady value takes some time because the pyranometers have a 20-second response time according to Figure 4.4. But also, the time taken to obtain the steady values of irradiance should not be long enough such that the focal points already move quite far from the location of the pyranometer. It could be that, due to this, under-scaling or over-scaling of the values obtained from the filtered irradiance might have happened. For example, at 11:54:15, an "Error" value (indicated with a value of -999999) was obtained. After putting on the filter, the readings progressively showed values of 3761, 2351, and 1749 W/m^2 which, if scaled accordingly to the filter rate of 39.65%, the real irradiance should be 9484, 5929, and 4411 W/m^2 respectively. The converged filtered irradiances that are closest to the measuring range were always taken, to not exaggerate the result and to allow room for more precise measurements in the future. In this case, the value of 4411 W/m^2 was taken.

Behavior of the focal lines

Characterizing the magnitude of irradiance over time and at different locations for the focal lines is challenging, as there is no constant average value that represents a strip of the focal line at any given time or location. However, the irradiance magnitude of the focal lines fluctuates over time, following the variations in the GHI obtained from CAMS, as shown in Figure 5.17.

Table 5.2 Irradiance of the focal lines

Duration			Irradiance of 1 focal line	Minimum	Maximum	Average
10:53:00	to	11:26:00	378 675 1567 1509 896 1225	378.37	1566.75	1041.80
11:37:00	to	11:50:15	1895 2105 2277 1894 924 791 995	790.77	2277.23	1554.28
12:14:30	to	13:08:30	1686 1182 1311 1646 1991 2024 1371 1528 1496 1258 349 2091 2851 2112 2162 1165 1377 2494 2096	349.49	2851.15	1694.15

Duration			Irradiance of 1 focal line	Minimum	Maximum	Average
13:29:45	to	14:00:45	1584 1177 1062 1280 1264 2235 1344 1229 1090 2464 2633 2424 3146 1287	1061.73	3145.84	1730.03
14:52:30	to	14:54:00	1338	1337.70	1337.70	1337.70
16:00:30	to	16:08:00	434 435 397 348 342	342.03	342.03	342.03

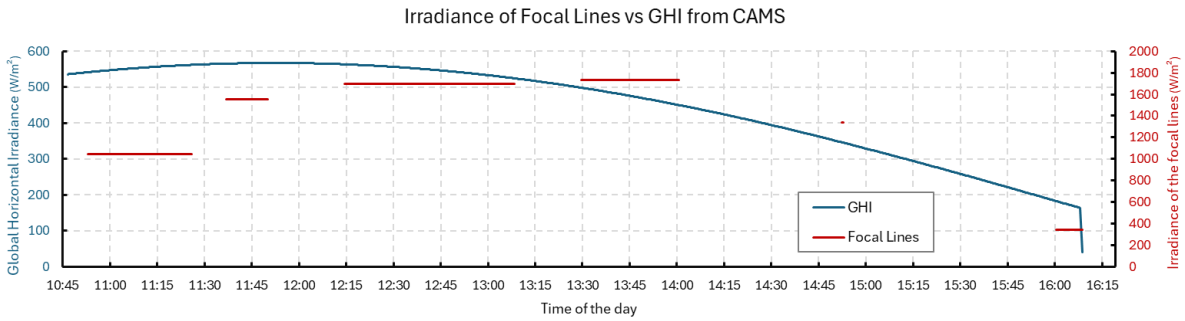

Figure 5.17 Irradiance of focal lines vs. GHI from CAMS for 8th March 2024 in Amsterdam UMC building

5.3. Simplified Two-Dimensional Model Results and Discussion

After previously discussing the methodology to calculate the intensity of the focal point from a 2D spherical and aspherical fully reflective specular mirrors in Chapter 4, the outcome of the simplified 2D model is discussed below.

5.3.1. Convergence of the Cross-Section of the Amsterdam UMC South Façade (Concave Quarter-Circle Spherical Mirror)

At first, a quarter-spherical mirror similar to the horizontal cross section of the south façade of the Amsterdam UMC building will be inspected, as shown in Figure 5.18. From Figure 5.19b, we can see that the optical axis of the south façade has a solar azimuth of 17.426 degrees from south. At a 0-degree angle, note that in Figure 5.19b, there is a red triangular area where the reflected rays from the sun do not coincide at a single location but instead converge closer to the vertex of the mirror, creating a crossing pattern. This phenomenon is known as spherical aberration, where rays further from the optical axis tend to be reflected closer to the surface of the mirror. In lenses, this effect is avoided because it causes blurred images. On the other hand, in the solar convergence phenomenon, strong convergence from minimal aberration can cause significant damage. The simulation is then run with paraxial rays hitting the mirror from a 0-degree angle towards the optical axis and gradually increasing to a 90-degree angle from the optical axis, as shown in Figure 5.20.

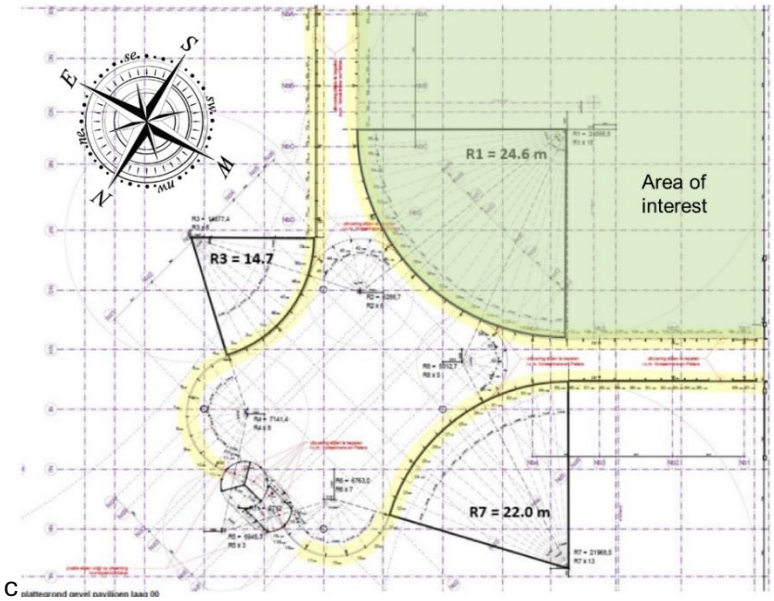

Figure 5.18 Site plan of the Amstedam UMC building with the corresponding radii in each curved façade

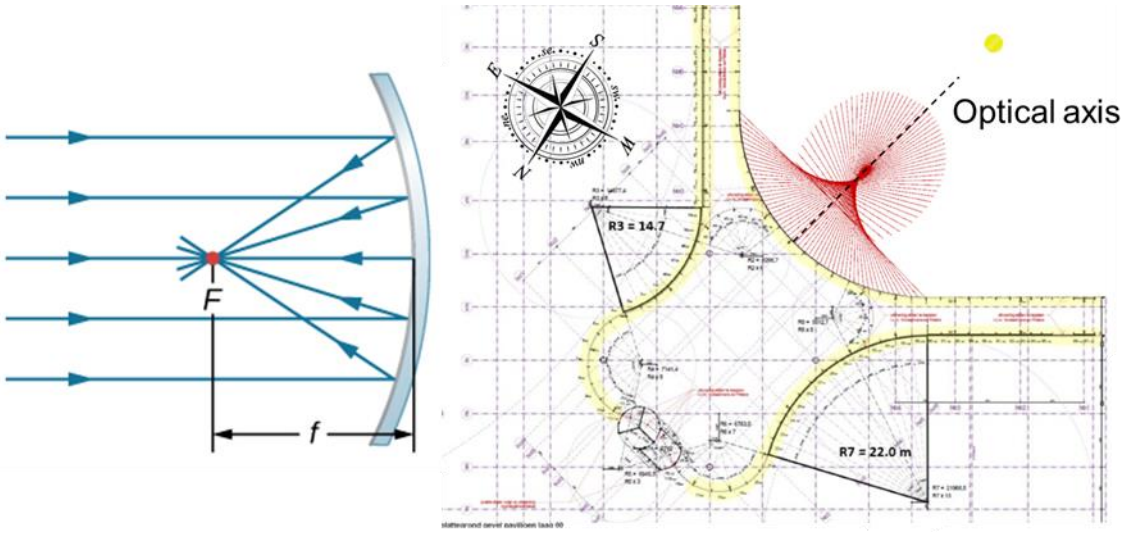

(a) (b)

Figure 5.19 (a) focal point location of a spherical mirror (Ling et al., 2016)(b) focal point of the Amsterdam UMC façade

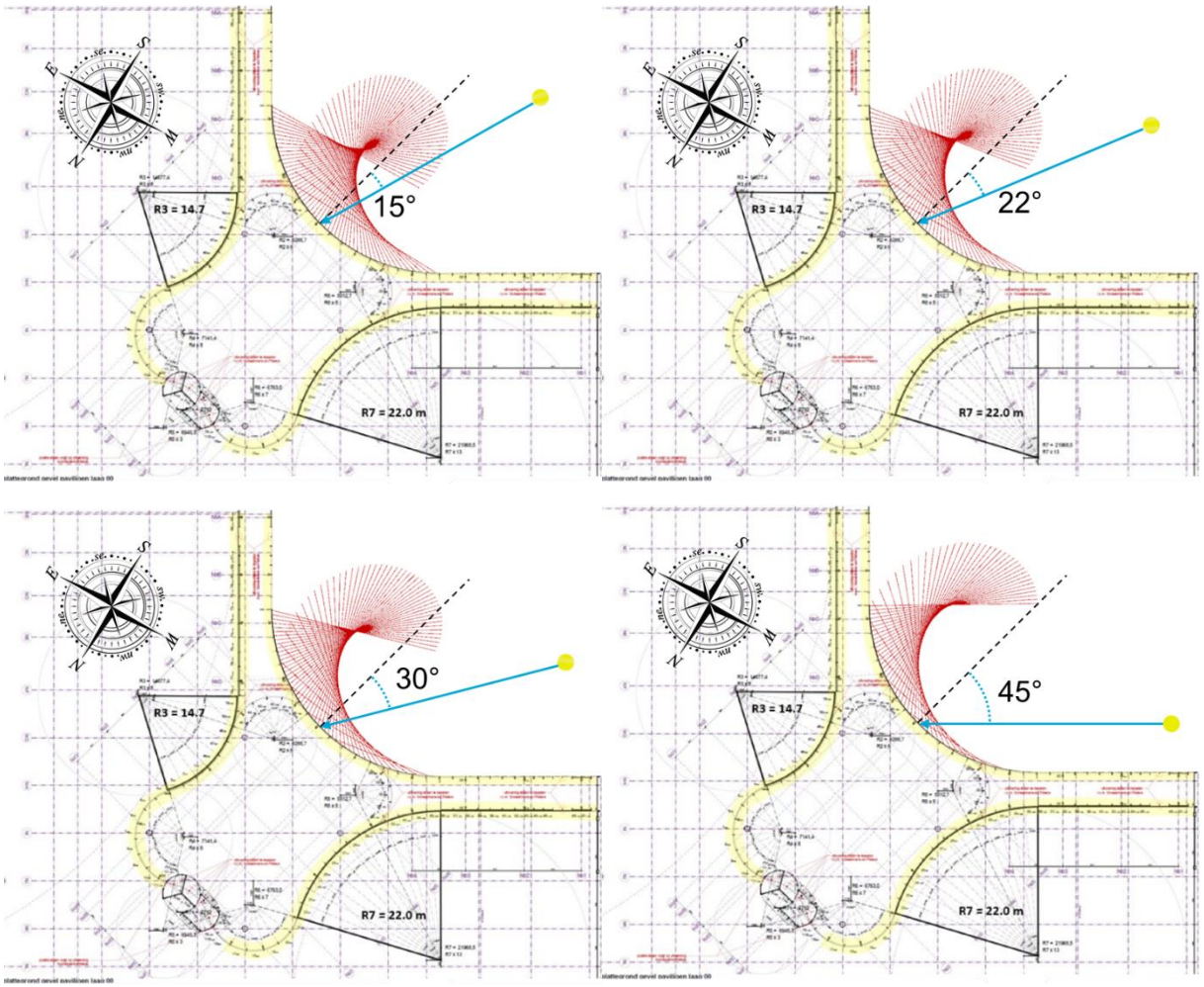

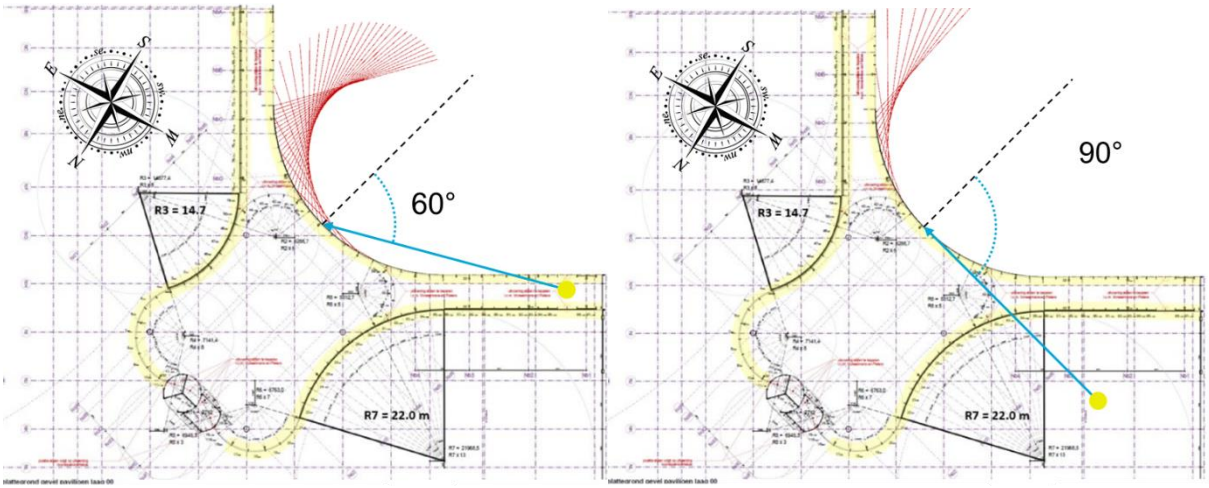

Figure 5.20 Reflected rays of a quarter-circle mirror

To simplify the approximation, the quarter-circle mirror described above was made with a radius of 200 m (arc length 100 π m) and a density of collimated rays per 5 m. The relationship between the number of intersections of reflected rays with the angle from the optical axis for a quarter-circle mirror is shown in Figure 5.21. Initially, it is found that the number of intersections between two reflected rays inside one mesh under a 0° angle from the optical axis is 94. However, this could be misleading if the reflections under different angles are not plotted such that the behavior is clearly shown. Therefore, the focal point intensity under a 0° angle is normalized to be equal to 1.0 as a benchmark to observe the fluctuation under different angles. With this normalization, the behavior is captured, and it will also be useful to compare one type of mirror to another.

When the collimated rays hit the mirror at an angle of 5° from the optical axis, the intensity increases to 1.20 times and plateaus steadily until it reaches a 25° angle from the optical axis, at which point the peak intensity is reached (1.245 times the solar convergence that occurs parallel to the optical axis). For any angle above 25°, the convergence factor decreases sharply until it reaches a 90° angle.

Thus, from the 2D model, the minimal aberration/maximum convergence of a quarter-circle mirror does not occur when the collimated beam hits the mirror parallel to the optical axis. Instead, it happens when they are shifted around 5 to 25 degrees from the optical axis. This effect will reappear when the 3D model is discussed in the next subchapter.

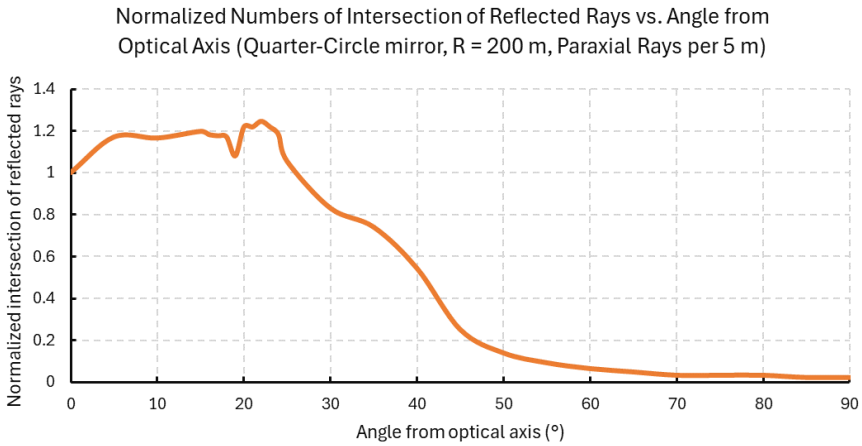

Figure 5.21 Number of intersection of reflected rays vs. Angle from optical axis (quarter-circle mirror)

5.3.2. Convergence of Concave Half-Circle Spherical Mirror

A concave half-circle spherical mirror will be used to create the next graph of the normalized intersections of reflected rays as a function of the angle from the optical axis. In this model, the arc length is set to be the same as in the previous model to provide a basis for comparison. Therefore, a radius of 100 meters is used, maintaining the same paraxial ray density and the same meshing size to count the number of intersections within the same plane. The visualization can be seen in Figure 5.22.

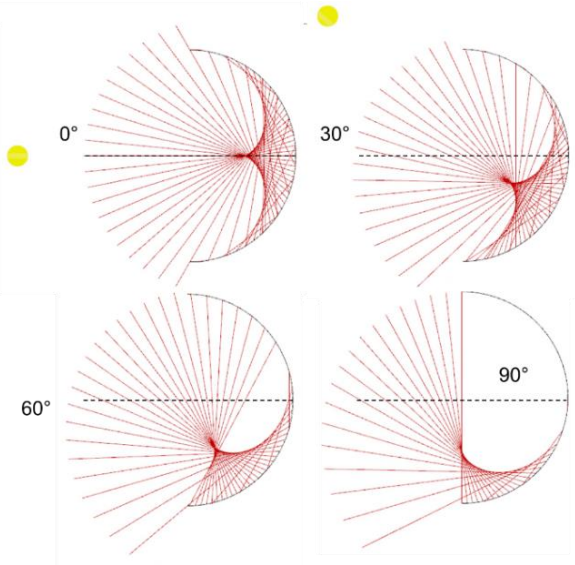

Figure 5.22 Reflected rays of a half-circle mirror

The relationship between the normalized number of intersections as a function of the angle from the optical axis is depicted in Figure 5.23. It is shown that the number of intersections is halved (53%) compared to the intersection of quarter-circle mirro at 0-degree angle, as more rays further

from the optical axis hit the curved mirror at shallower angles, resulting in more aberrations and even a small number of intersections landing behind the curved mirror. This indicates that a half-circle mirror with the same arc length will not converge solar rays as effectively as a quarter-circle mirror. However, its convergence remains constant throughout a larger span of angles from the optical axis. After reaching a 70-degree angle, the number of intersections drops sharply. The fluctuations shown in the graph are primarily due to the common instability of numerical models; however, the actual magnitude of convergence should not deviate significantly from this value. It is evident that in this shape, the focal point will always land halfway between the center and the surface of the spherical mirrors, similar to a quarter-circle mirror.

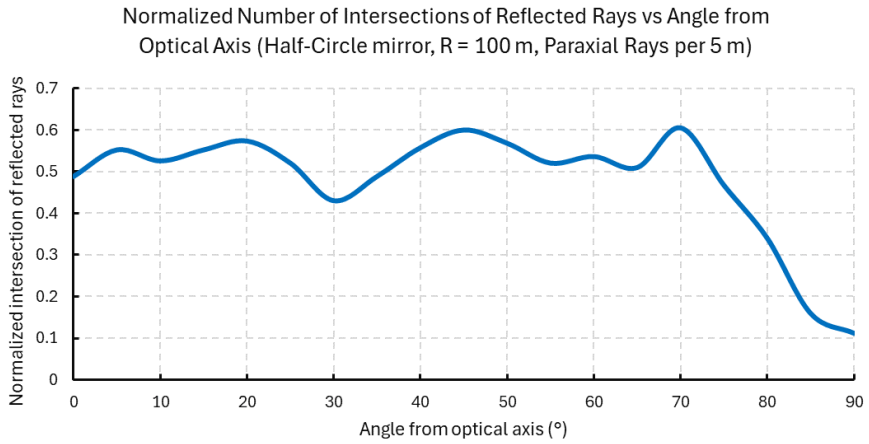

Figure 5.23 Number of intersection of reflected rays vs angle from optical axis (half-circle mirror)

5.3.3. Convergence of Aspherical Mirrors

Beside spherical mirrors, curved surfaces can be made into aspherical forms. These types of surfaces can also pose a danger of solar convergence from façades because, in objective optics, aspherical forms are typically used to focus light rays, including marginal rays, into a single point. This principle, while beneficial in objective optics, poses risks when occurs from building façade. Most engineered aspherical mirrors have surface curvature that varies across the surface. As a result, the reflection of marginal rays can be manipulated so that their intersections with other rays remain clustered with the reflections of paraxial rays, leading to a more focused reflection (Dereniak & Dereniak, 2008). However, it is important to note that this rule applies if the aspherical mirrors have the same width as the spherical mirrors. In this subchapter, five aspherical two-dimensional mirrors which have the same arc length will be reviewed.

1. A concave half elliptical mirror symmetric to the minor axis,
2. A concave half elliptical mirror symmetric the major axis,
3. A concave quarter elliptical mirror,
4. A concave parabolic mirror,
5. A concave one sided hyperbolic mirror.

5.3.3.1. Concave Half-Elliptical Mirror Symmetric to the Minor Axis

The first aspheric mirror to be discussed is the half-elliptical mirror symmetric to the minor axis, which can be seen in Figure 5.24. In this model, the length of the semi-major axis is twice the length

of the semi-minor axis. Collimated rays are then projected towards the mirror gradually from a 0-degree angle to a 90-degree angle with respect to the optical axis. As can be seen in the figure below, as the angle from the optical axis changes, the location of the focal point also changes, but it is located close to the circumference of the other half of the ellipse which has been removed. At a 90-degree angle from the optical axis, the focal point is located at one of the two foci to create the geometry of the ellipse itself. The resulting normalized intersection of the reflected rays can be seen in Figure 5.25, where, on average, the intensity of the convergence is around 37.4% compared to the convergence of a quarter-circle mirror at a 0-degree angle from the optical axis, and it peaks at 44% when the angle reaches 75 degrees from the optical axis.

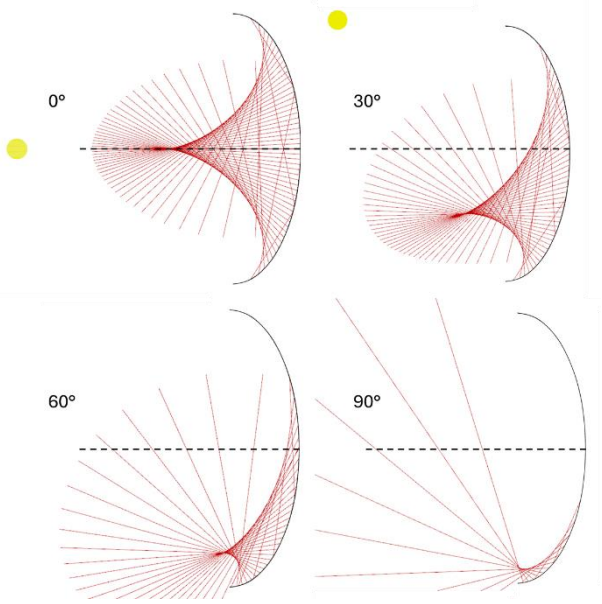

Figure 5.24 Reflected rays of a half-elliptical mirror symmetric to the minor axis

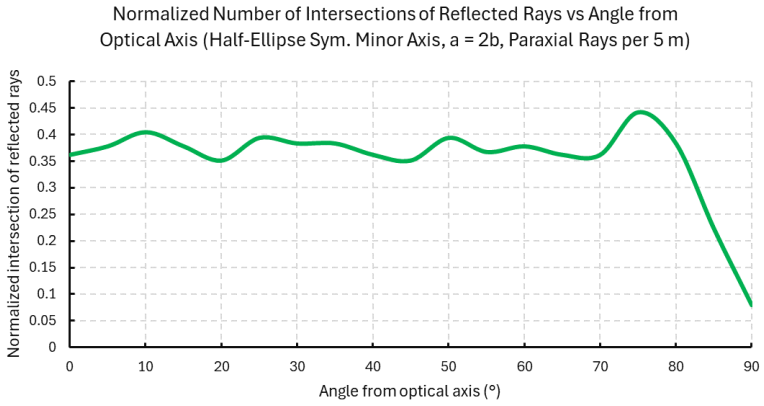

Figure 5.25 Number of intersections of reflected rays vs angle from optical axis (half-elliptical mirror symmetric to minor axis)

5.3.3.2. *Concave Half-Elliptical Mirror Symmetric to the Major Axis*

From the same elliptical geometry, another cut is made to form a half-elliptical mirror symmetrical to the major axis, as illustrated in Figure 5.26. The figure shows that, in most instances, the focal points land near the actual surface of the mirror. However, the convergence behavior differs considerably from the previous model, as depicted in Figure 5.27. The convergence exhibits bigger fluctuations than the previous model, with a peak value of 43.6% compared to the quarter-circle mirror at a 0-degree angle. On average, the convergence value is 36.4% when the angle of the collimated rays varies from 0 degrees to 60 degrees. Beyond this angle, the convergence sharply diminishes.

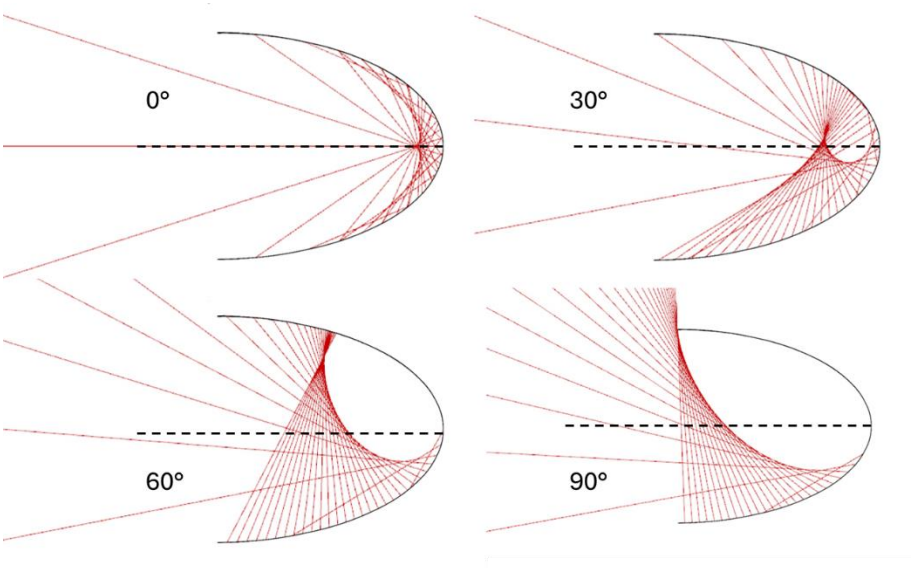

Figure 5.26 Reflected rays of a half-elliptical mirror symmetric to the major axis

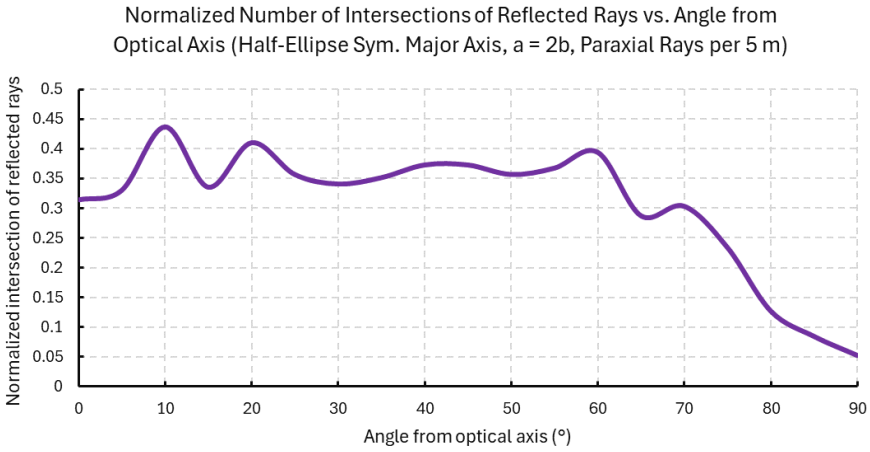

Figure 5.27 Number of intersections of reflected rays vs angle from optical axis (half-elliptical mirror symmetric to major axis)

5.3.3.3. Concave Quarter-Elliptical Mirror

The final elliptical mirror to be examined is the concave quarter-elliptical mirror, which has the same arc length as the previous models. Since this mirror lacks symmetry, defining the optical axis becomes less straightforward. However, assuming the optical axis is represented by the black dashed line in Figure 5.28, the location of the focal points resembles those of the elliptical models, where they land at one of the foci of the ellipse's geometry at 0-degree and 90-degree angles from the optical axis. For angles between these two, the movement of the focal point is more complex to characterize but is depicted in Figure 5.28, showing an elliptical trajectory.

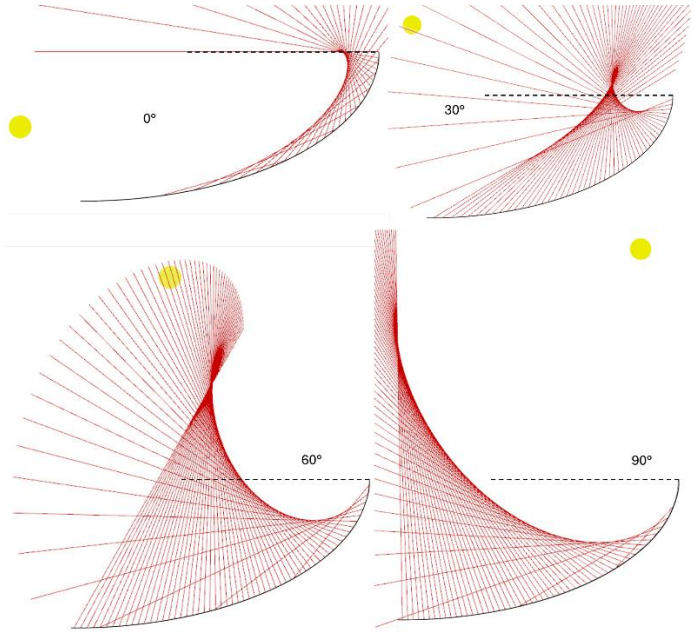

Figure 5.28 Reflected rays of a quarter-elliptical mirror

From Figure 5.29, at a 0-degree angle from the optical axis, the normalized convergence is only 25% in magnitude compared to the quarter-circle mirror under the same angle. The peak convergence occurs at an angle of 10 degrees from the optical axis, with an intensity around 98%. On average, the convergence is only 76% for angles ranging from 25 degrees to 70 degrees, after which it diminishes sharply for any angle greater than 70 degrees.

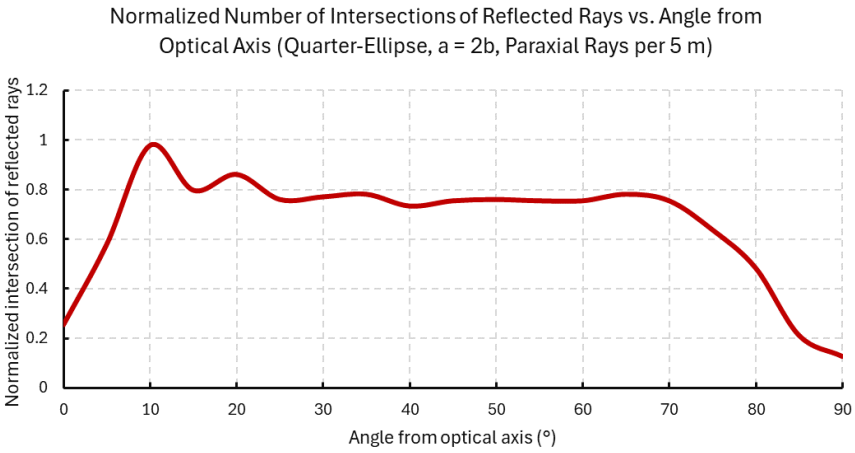

Figure 5.29 Number of intersection of reflected rays vs angle from optical axis (quarter-elliptical mirror)

5.3.3.4. *Concave Parabolic Mirror*

Another aspheric concave mirror to be observed is the parabolic mirror. In this case, a parabolic mirror with the formula $y = {}^{1}/_{8}\,x^{2}$ is modeled, with the arc length kept the same as in the other models. The ray tracing results are shown in Figure 5.30. At a 0-degree angle from the optical axis, all of the reflected rays from any point on the surface converge to a single point, indicating that the parabolic mirror provides the highest intensity of convergence compared to the previous models. However, beyond a 30-degree angle, no focal points are formed. These observations are supported by the fact that the convergence at a 0-degree angle is 476% greater than that of a quarter-circle mirror at the same angle. However, it quickly reduces to below 10% after reaching a 25-degree angle as can be seen in Figure 5.31.

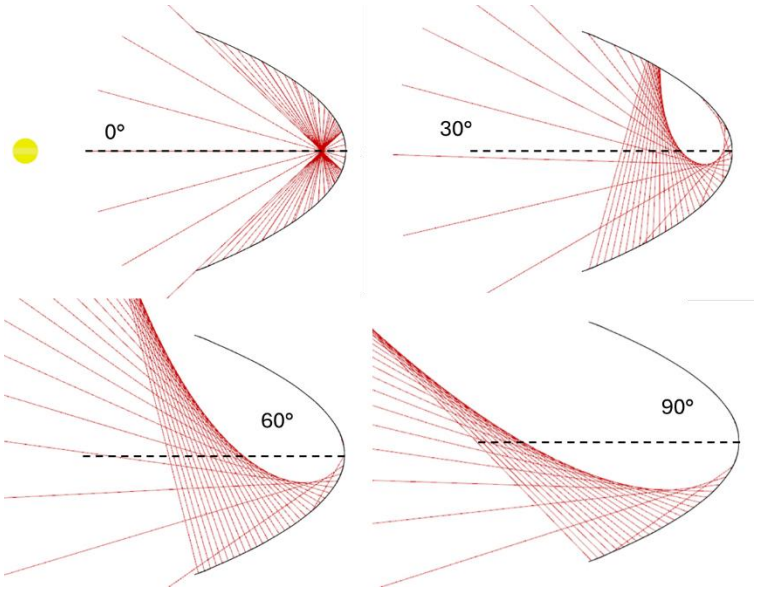

Figure 5.30 Reflected rays of a parabolic mirror

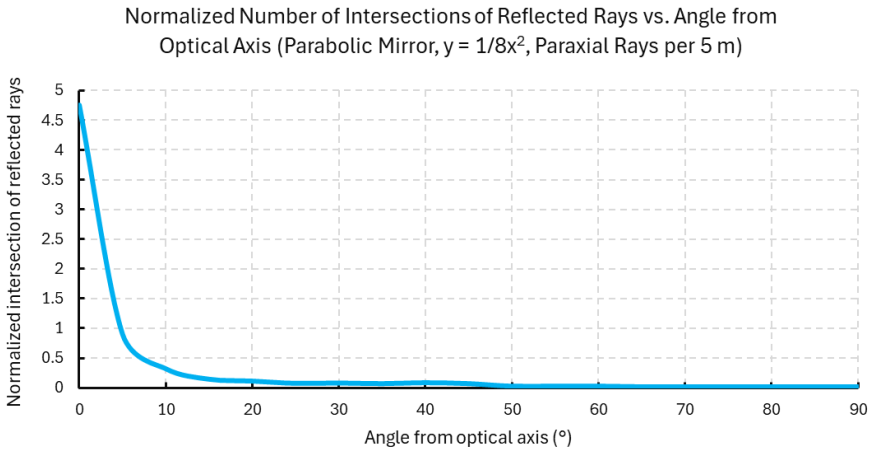

Figure 5.31 Number of intersection of reflected rays vs angle from optical axis (parabolic mirror)

5.3.3.5. Concave Hyperbolic Mirror

The final aspheric mirror to be observed is a concave mirror derived from one side of a hyperbola with equal lengths of the semi-major and semi-minor axes (a = b in the hyperbola equation), while maintaining a constant arc length consistent with the previous models. As shown in Figure 5.32, at a 0-degree angle, typical hyperbolic mirror produces the most aberration compared to the previous types of mirrors, particularly for the reflected marginal rays, which intersect farther from the surface of the mirror as the distance perpendicular to the optical axis increases. Similar to the parabolic mirror, the convergence is at its highest at a 0-degree angle from the optical axis, as the reflected rays constituting the focal points diverge further as the angle to the optical axis increases. Therefore, it is unsurprising that, as shown in Figure 5.33, the convergence decreases linearly from 40% to 2% as the angle from the optical axis increases from 0 degrees to 40 degrees.

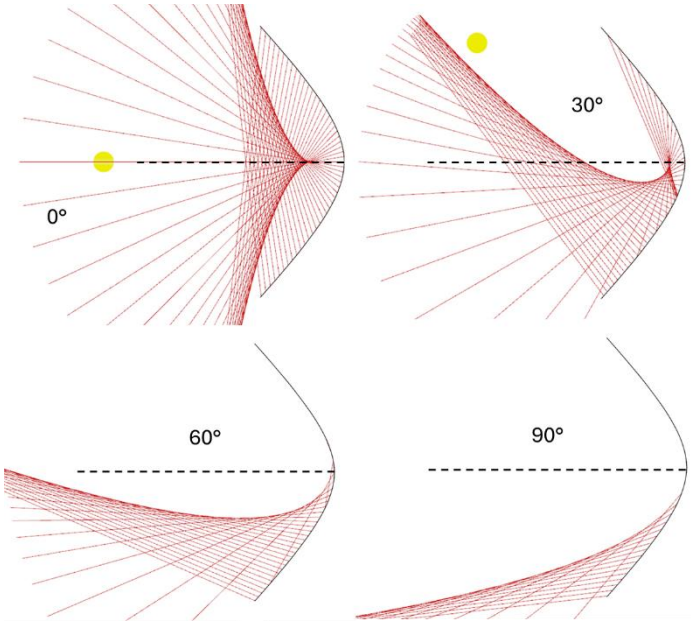

Figure 5.32 Reflected rays of a hyperbolic mirror

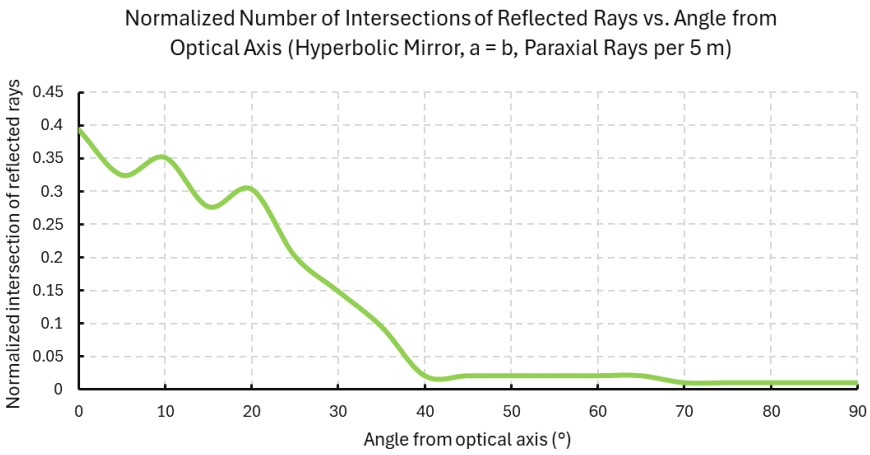

Figure 5.33 Number of intersections of reflected rays vs angle from optical axis (hyperbolic mirror)

5.3.4. Conclusion from 2D Models

From the simple 2D models, it is found that different types of geometries acting as concave mirrors result in different behaviors of convergence, both in terms of the locations of the focal points and the magnitude of convergence, despite having the same arc length and being subjected to the same density of light rays. The shape that provides the most intense effect of solar convergence is a concave parabolic mirror when all the collimated rays are parallel to the optical axis. With the same arc length as a quarter-circle spherical mirror, its intensity is 4.7 times higher under a 0-degree angle from the optical axis. Luckily, it diminishes quickly so that only under 0 to 5 degrees from the optical axis are the focal points more concentrated than those of a quarter-circle mirror.

Under any angle from the optical axis, concave mirrors with cross-sections being a half-circle, a half ellipse symmetrical to the major axis, a half ellipse symmetrical to the minor axis, and a symmetrical hyperbola will not have equal or exceeding concentration of focal points compared to a quarter-circle concave mirror with the same arc length as can be seen in the top part of Figure 5.34. Most of which will only have around 0.2 to 0.6 of the intensity of the focal point of a quarter-circle mirror.

A quarter ellipse, however, with the same arc length as a quarter circle, can have similar concentrations of light rays under a 10-degree angle. Unlike a quarter circle, in which the concentration of the focal point dissolves quickly after 25 degrees from the optical axis, the concentration of the focal point of a quarter ellipse remains roughly the same even after the light rays reach a 70-degree angle from the optical axis.

Even though not all of the 2D models above will be further expanded and simulated in 3D models, they provide insights into the behavior of focal points in relation to the geometric shapes. It is also important to note that for a single-curved façade in a 3D realm, focal points can occur at different heights perpendicular to the cross-section, which depend on the solar height, thus reducing the effect of convergence. However, at the same time, a 3D object, in this case a façade, which has double-curvature (one in the horizontal cross-section and the other in the vertical cross-section), can also lead to a further increase in converged reflection. Thus, insights from these 2D models should be imagined acting in three-dimensional space to avoid underestimation.

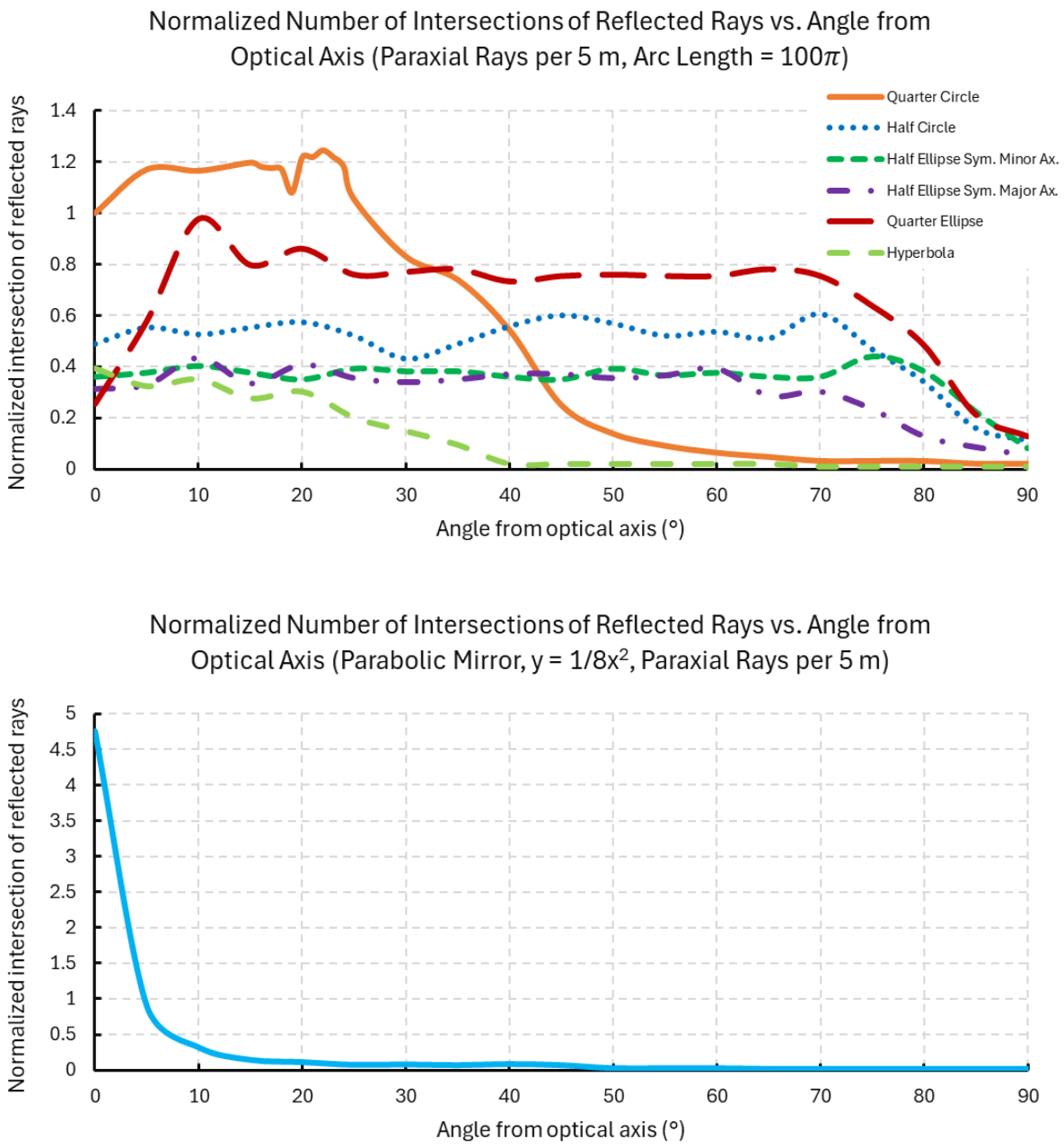

Figure 5.34 Graph of Normalized Number of Intersections from Concave Conic Mirrors

5.4. Three-Dimensional Model Results & Discussion

In addition to the 2D model to understand the influence of geometry on the solar convergence phenomenon, a 3D numerical model was developed to more accurately predict the results. In this 3D model, the nonlinear reflectance rate as a function of the angle of incidence is implemented alongside four different anisotropic sky models. The program was used to simulate the solar convergence phenomenon of the Amsterdam UMC building, for the same day the measurement took place: Friday, 8 March 2024. The part of the building used to re-enact the phenomenon was the south façade of the Amsterdam UMC receptionist building, and the solar reflectance is predicted to fall on the green area as noted in left side of Figure 5.35. The other sides of the building (east and west façades) have not been studied in this thesis, and the northern part of the building receives direct sunlight only in the middle of summer, early in the morning or late in the evening.

As shown in the same figure, the radius of the façade facing south is 24.6 meters. However, the glass panels on the southern façade do not share the same curvature as the shape of the building. Instead, the curvature of the glass panels on the southern façade is the same as that of the glass panels on the west façade, which is 22.0 meters. This mismatch (incompatibility) of curvatures is categorized as a systematic error. The effect of the systematic error will be further discussed by matching the shape and intensity of the reflections on the ground between the model and reality. The illustration of this occurence in the façade can be seen on the right side of Figure 5.35.

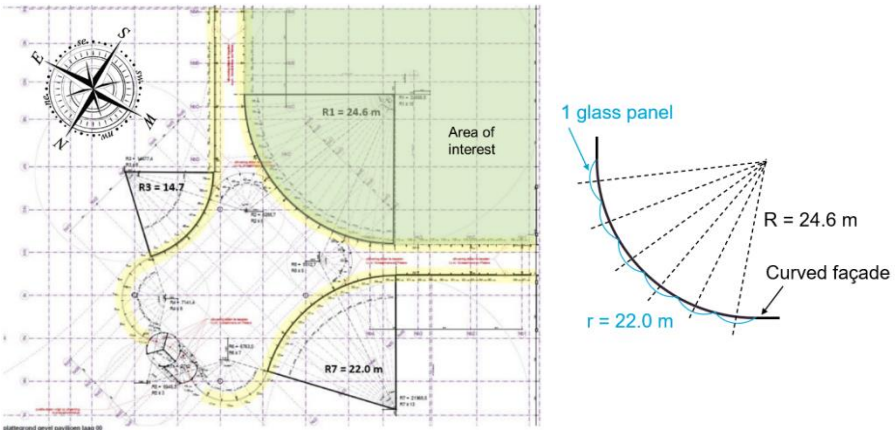

(a) (b)

Figure 5.35 (a) Site plan of the Amstedam UMC building with (b) curvature mismatch (incompatibility) of glass panels

As mentioned earlier, all façades in the receptionist area are made from stacked laminated glass of two PLANICLEAR (6 mm) glasses, one of which is coated with COOL-LITE SKN 165 II, and the two are bonded with PVB Standard (2 × 0.38 mm). The glass that is coated is located outside, but the coating itself is the inside layer of the glass as can be seen in Figure 5.36. The outdoor reflectance rate for the complete spectrum of light is calculated to be 25% at a 90-degrees angle of incidence.

Figure 5.36 Configuration of the laminated glass

5.4.1. The Effect Curvatures Mismatch (Incompatibility)

As discussed in the previous chapter, the geometrical shape of the façade, acting as a partially reflective mirror, significantly affects the concentration and the location of focal points. By comparing the visual inspection with the 3D model, it can be seen that mismatch in the curvature of the glass panels with the façade alter the overall shape of the converged reflection as can be seen in Figure 5.37 and Figure 5.38. When using the same radius for both the façade and the glass panels, the reflection shapes in the Figure 5.37c and Figure 5.38c are more uniform. However, when a mismatch exists, the reflection shapes in Figure 5.37b and Figure 5.38b show similarity between the shapes between the reality and the 3D numerical model.

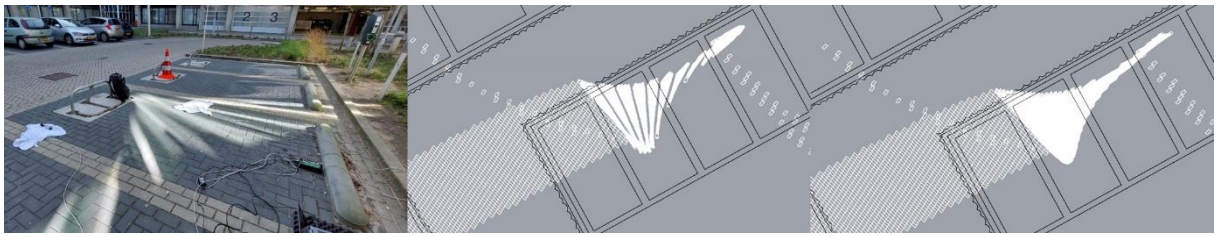

(a) (b) (c)

Figure 5.37 Difference in the reflection shape between (a) reality, (b) R = 22.0 m (b) R = 24.6 m at 12:25 CEST

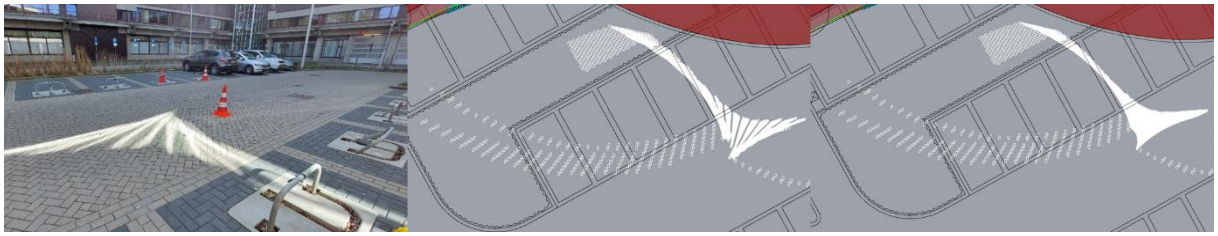

(a) (b) (c)

Figure 5.38 Difference in the reflection shape between (a) reality, (b) R = 22.0 m (b) R = 24.6 m at 13:58 CEST

Although this curvature mismatch may seem insignificant, in reality, it causes discrepancy in the effect of the converged solar reflection. With the same base length for placing the glass panels, a smaller radius results in bigger sagitta in the cross section of the façade which also results in different angle of incidence and different angle of reflection, thus causing the behavior of convergence to be more complex to analyze. It can, at some point, causes greater light concentration and less aberration, but at another time causes the opposite. This incompatibility also displays reflection shapes that have jaggier edges and more concentration in some parts, creating focal lines, while other parts are not illuminated by the reflection rays. Comparing the irradiance occurring between the models with different radii, it is found that the curvature mismatch causes the focal points to increase to 23.52% at some point, and decrease 13.09% at another time, depending on the time of the day observed, as can be seen in Figure 5.39.

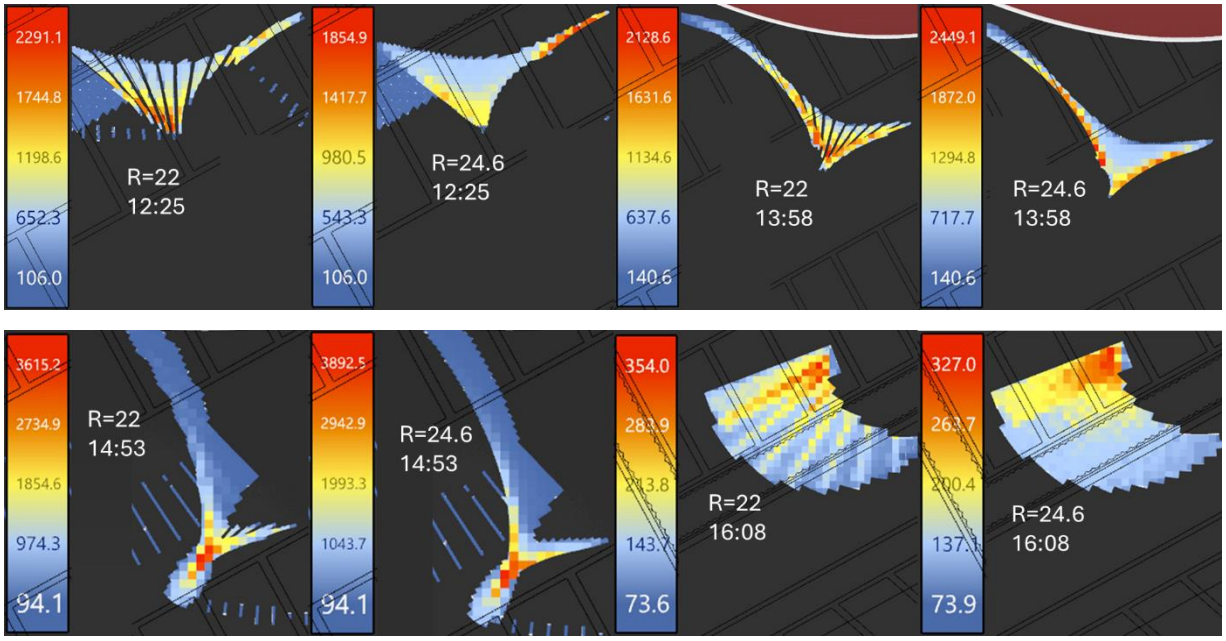

Figure 5.39 Difference in irradiance due to incompatibility of curvatures

5.4.2. Irradiance Map and The Relation to 2D Model

After ensuring the correct curvature of the façade, the 3D model was run to reenact the solar convergence phenomenon. Four sky models (isotropic, Klucher, Hay-Davies, Reindl) were used and compared. Since the anisotropic models consider ground reflection, the albedo value was set at 0.3, though values from 0.3 to 0.75 are reasonable for new concrete pavement (Acharya et al., 2021). A small value of 0.3 was chosen to avoid false positive overestimation in converged solar reflection, which happens not because of the anisotropy in the sky but because of the reflected ground irradiance.

Since the sky was clear on the day of measurement, and there were no signs of overcast, the Reindl model, which in theory produces the highest irradiance, is reliable to correctly represent the sky conditions. The clearness index obtained using the Reindl model is well above 0.95. Therefore, the heatmap shown in the document is the one obtained using the Reindl model, as can be seen in Figure 5.40.

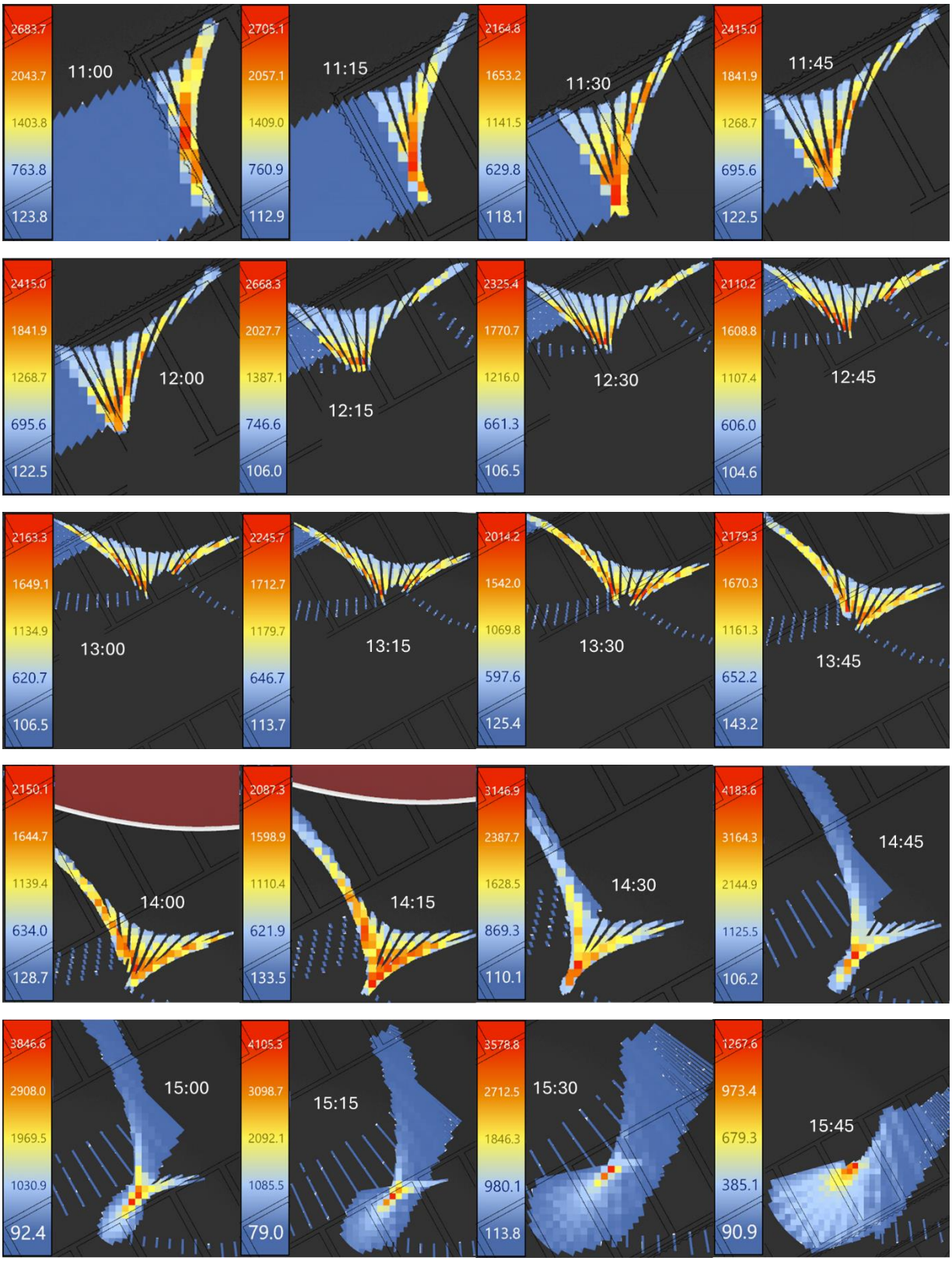

Figure 5.40 Irradiance map as a result of the 3D model for 8 March 2024

Figure 5.40 shows that the focal point reaches the highest intensity of irradiance at 14:45 and 15:15 CEST, with peaks around 4183.6 W/m^2 and 4105 W/m^2, respectively, according to the Reindl model. At these times, the sun's azimuth is 147.335 degrees and 139.535 degrees, respectively, from the north. Note that from the simplified two-dimensional model, for a quarter-circle, the angle with respect to the optical axis at which the maximum normalized convergence occurs is 22 degrees. When these solar azimuths are converted into the local coordinate system of the quarter-circle mirror (as a simplification of the 3D model), they correspond to 15.24 degrees and 23.038 degrees, respectively, from the optical axis, as shown in Figure 5.41. This indicates that the maximum solar convergence in the 3D model is influenced by the behavior of the quarter-circle mirror in the 2D model, especially remembering that neither GHI, BNI, BHI, DNI, nor DHI at 14:45 and 15:15 is at its highest by looking at Figure 4.16. In other words, apart from the magnitude of the irradiance, the worst effect of solar convergence in this building will likely occur when the solar azimuth is around 139 degrees to 148 degrees from the north for any given day corresponds to a range of around 15 degrees to 25 degrees with respect to the optical axis of the façade.

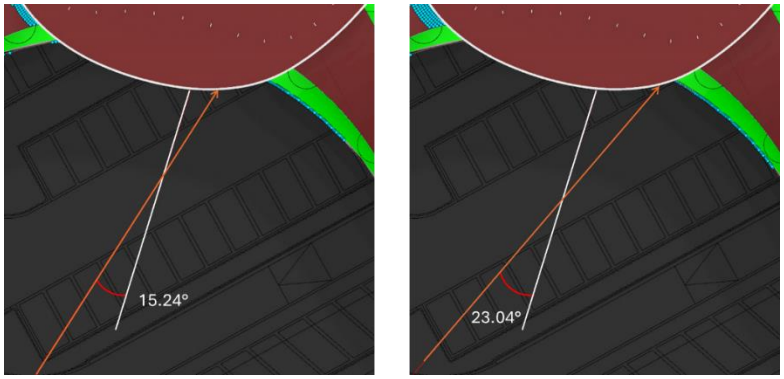

Figure 5.41 Angle from optical axis at 14:45 and 15:15

5.4.3. Solar Irradiance from Isotropic and Anisotropic Sky Models

After the heatmap is obtained from the Reindl model, the changes in the intensity of the focal points as time progresses is shown in Figure 5.42. It can be seen that during the first 1.5 hours of the inspection (10:47:00 to 12:15:00), the intensity of the focal points fluctuated from 2144.3 W/m^2 to 2668.3 W/m^2. And for the next 2 hours (12:15:00 to 14:15:00), the intensity of the focal points plateau steadily. Comparing the irradiance of the focal points over time with the Global Horizontal Irradiance, it is then obvious that the times in which the maximum intensity of the focal points occur do not necessarily have to be close to the time when the global horizontal irradiance is at its max.

About an hour later, the intensity of the focal point increases sharply, and at its peak, it roughly doubles to 4183.6 W/m^2 because the solar vector from the sun hits the façade at around 15 to 25 degrees with respect to the optical axis, as mentioned earlier. Similar to the behavior of a quarter circle, the intensity of the focal points decreases sharply after 15:30 because the number of intersections between the reflected rays dissolves into different directions after 25 degrees is reached.

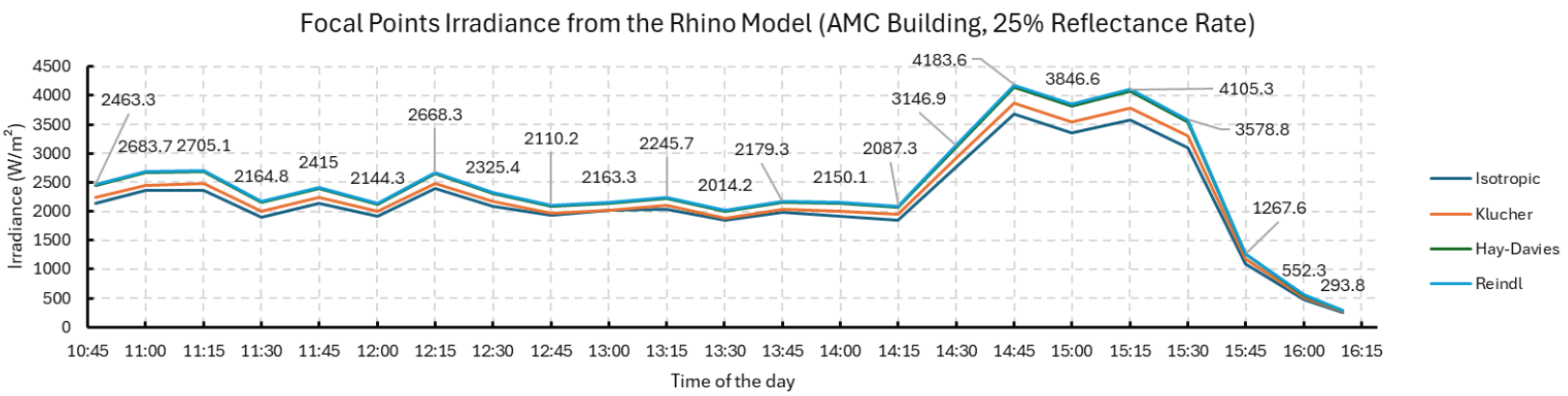

Figure 5.42 Irradiance of The Focal Points from 4 Models

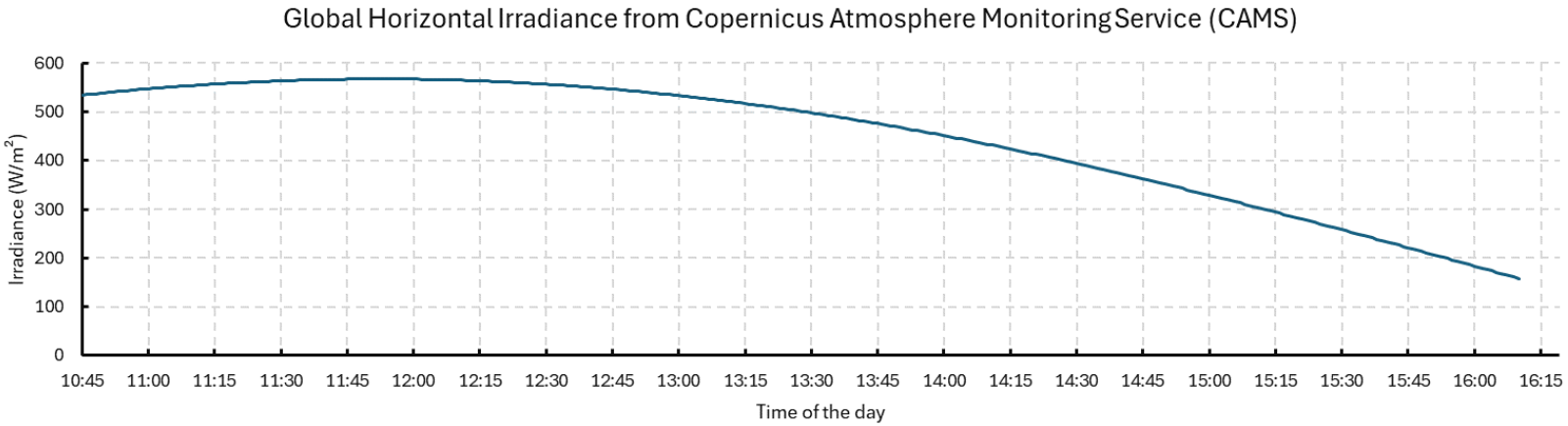

Figure 5.43 Global Horizontal Irradiance of the Amsterdam UMC on 8 March 2024

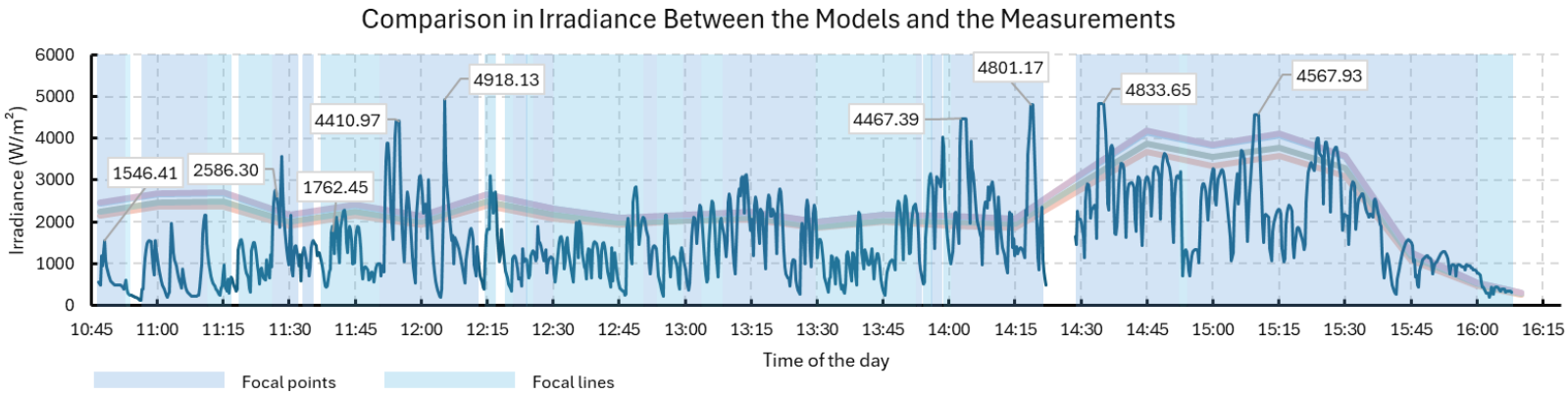

Figure 5.44 Comparison in Irradiance between the 3D Models and the Measurements

Notice that from Figure 5.42, it is clear that the influence of anisotropy in the three sky models generally increases the irradiance of the reflection that falls on the ground level. As shown in the theory, the irradiance produced from the Reindl model is always the highest as the time progresses, this is because Reindl model consider all of the parameters which Klucher and Hay-Davies model do. The increases from each of the anisotropic sky models compared to the isotropic model within this period of inspection is:

- Klucher model : -0.01% to 7.66%
- Hay-Davies model : 5.90% to 15.39%
- Reindl model : 6.77% to 16.40%

The complete dataset of the irradiance from the four sky models will be shown in Appendix F.

5.4.4. Comparison of the 3D Models with The Measurement Data

As seen in Figure 5.44, it is evident that the changes in the irradiance value in the 3D model closely relate to the measurement, not taking into account the noise from the measurement data. Both graphs show a plateau at the start of the measurement and an increase after 13:45. At the tail of the measurement data, the changes in the intensity of the focal points are captured accurately by the 3D model.

However, as can be seen in the same figure, between 11:45 and 12:15, there is an increase in the measurement data that is not captured by the 3D model. This discrepancy is most likely because, during this time, the inspection began to utilize a filter to tone down the readings and needed some time to get accustomed to it.

This filter, although helping in reading the irradiance of focal points well above 4000 W/m^2 because it is the maximum measuring range of the pyranometers, might have caused overscaling, as can be seen from 14:15 to 15:15. Around that time, the irradiance value from the 3D models considering the anisotropy of the sky are still below the measurement data. Overscaling due to the filter might have occurred since the filter rate value changes over time due to heat absorption. Therefore, from the same figure, it can be seen that the highest intensity of the focal point recorded in the measurement data is 1.15 times higher than the highest intensity of the focal point from the 3D model, which starts only 7.5 minutes differently.

5.4.5. Uncertainty from the Setting of the Measuring Mesh Size

As mentioned earlier, in the algorithm scheme, the solar irradiance measured on the ground is calculated by dividing the radiant power from the reflection by the corresponding landing area, which was obtained from the distorted shape of the sky dome, merged together, and then discretized. Therefore, presumably, the size of each discretized surface is important because too small measuring surfaces will result in overscaled irradiance, and vice versa. Additionally, since the sun rays shooting from the sky dome represent a finite amount of a limited area of the sky, a relationship between the two can be established. This relationship ensures that the algorithm is well-calibrated and can be implemented not only specifically for this model but also for other models and other cases.

First of all, certain locations on the ground within the 3D model, denoted with red dots in Figure 5.45, are chosen to check for changes in irradiance as the mesh size of the measuring plane changes. In this case, two different epochs for which the irradiance is known are chosen, and then the mesh size is increased from 225×225 mm^2 to 375×375 mm^2.

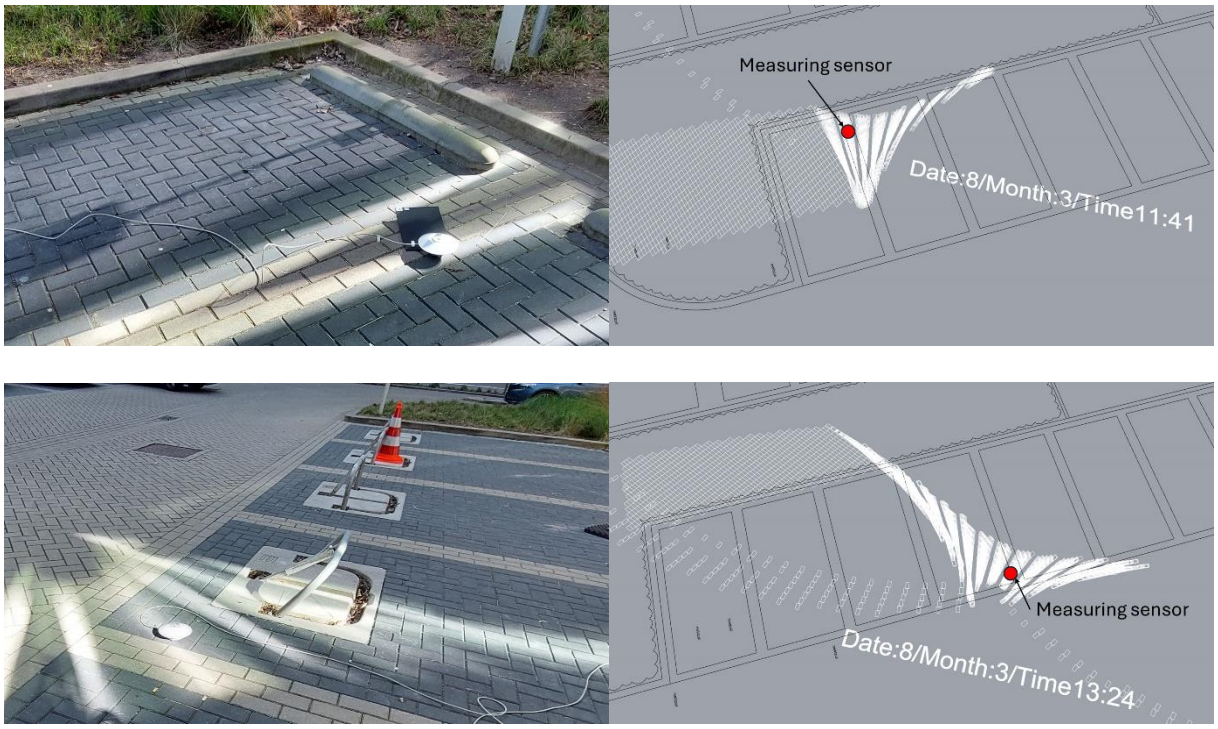

Figure 5.45 Location and epoch to check for mesh size uncertainty

From the measurements, the irradiance at 11:41 AM and at 1:24 PM at the two locations is 1238.03 W/m^2 and 1100.38 W/m^2, respectively. As shown in Figure 5.46, in the 3D model, the irradiance at 11:41 AM changes as the mesh sizes change. Figure 5.47 demonstrates that the fluctuation of the irradiance ranges from as low as 734.26 W/m^2 (mesh size 270×270 mm^2) to as high as 931.82 W/m^2 (mesh size 255×255 mm^2). Even though the mesh size is changed from 225 to 375 mm, from the smallest to the largest, the irradiance from the 3D model at 11:41 AM is still much lower than the collected data, with a standard deviation for different mesh sizes of 64.83 W/m^2.

However, at another epoch, 1:24 PM, as seen in Figure 5.48 and Figure 5.49, the deviation of solar irradiance from one mesh size to another is smaller compared to the previous epoch, with the minimum irradiance being 887.95 W/m^2 (mesh size 330×330 mm^2) and the highest being 1112.12 W/m^2 (mesh size 240×240 mm^2). In this epoch, the irradiance from the collected data and the 3D model is now in the same order of magnitude with a lower standard deviation, which is 62.06 W/m^2.

For both cases, the coefficients of variation are 8.44% and 6.4%, respectively, indicating that there is some variability due to the changes in the mesh size. However, from the analysis of variance (ANOVA) test, for both datasets, these fluctuations are not statistically significant, since the p-values of the first and second epochs are 0.883907 and 0.451065, respectively.

In conclusion, for the sake of avoiding computationally expensive algorithms, a mesh size of the measuring grid of approximately 300×300 mm^2 is used for this script, which still yields satisfactory results. Since the size of the mesh of the sky dome used is 100×100 mm^2, roughly, as a rule of thumb, to use the algorithm scheme properly, the size of the measuring plane should be three times the size of the mesh of the sky dome.

Lastly, from Figure 5.47 and Figure 5.49, there is no evidence showing a trend where the irradiance increases as the mesh of the measuring plane gets smaller, as was previously assumed. From the two epochs, increasing the mesh size results in an increase at the first location and a decrease at another location. Therefore, it is safe to say that the model will not diverge into unstable conditions when choosing different sizes of meshes.

However, it is also not possible to suggest that the irradiance value from the Grasshopper script will yield extremely accurate results, as the bandwidth between the highest and lowest predictions of irradiance is proportionally quite large, with the ratio being 1.27 and 1.25 for the first and second epochs, respectively. Further studies need to be conducted to understand why the bandwidth shares similar values and whether the inaccuracy is a coincidence or a systematic error emerging from the logic of the script.

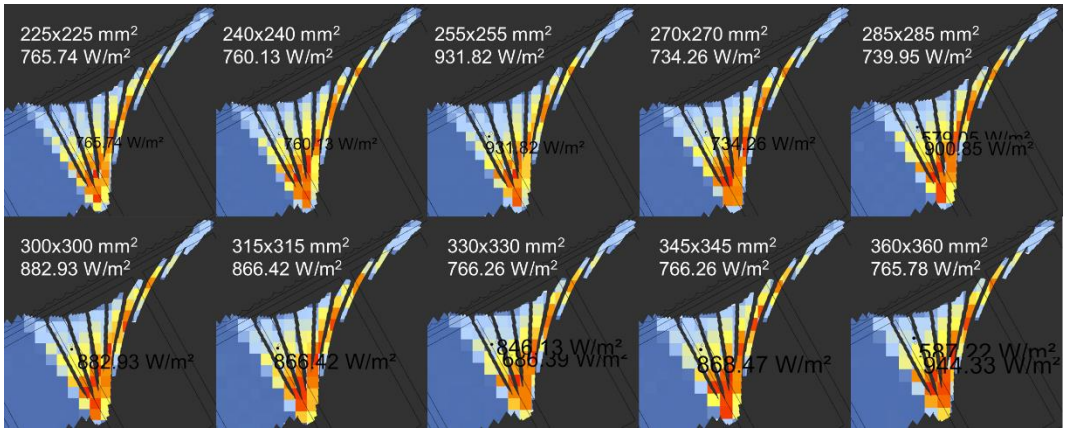

Figure 5.46 Changes of irradiance corresponding to the mesh size (11:41 AM)

Mesh length	Irradiance (W/m^2)
225	765.74
240	760.13
255	931.82
270	734.26
285	739.95
300	882.93
315	866.42
330	766.26
345	868.47
360	765.775
375	783.695
Minimum	734.26
Mean	805.95
Maximum	931.82
Std. Deviation	64.83

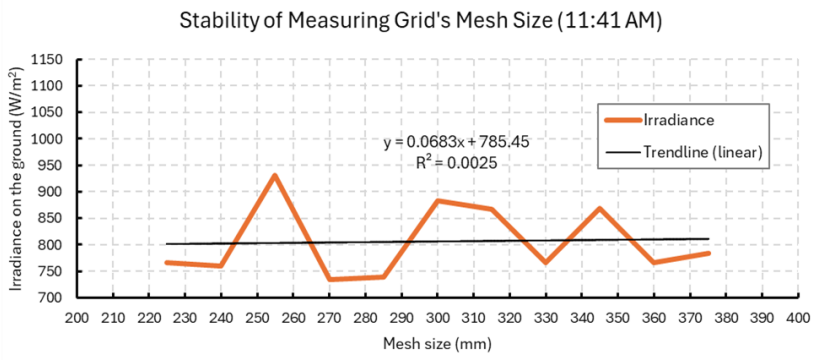

Figure 5.47 Fluctuation of irradiance corresponding to the mesh size (11:41 AM)

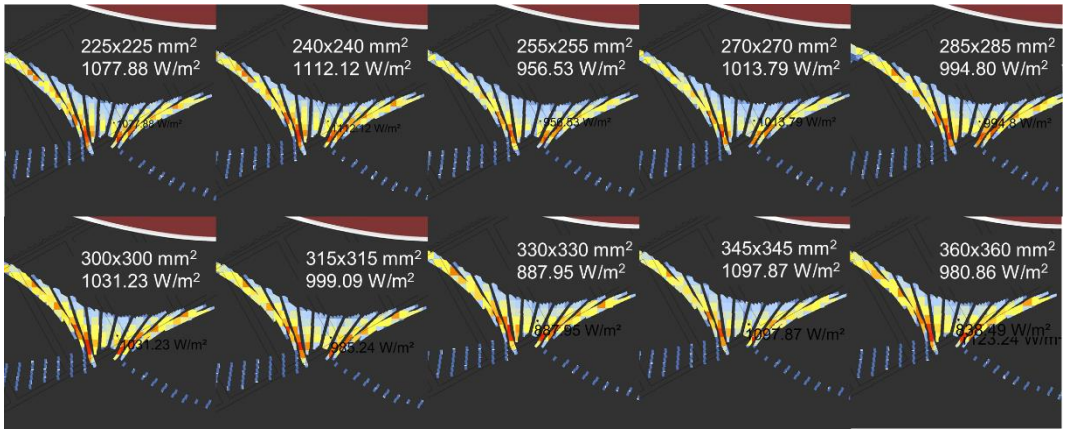

Figure 5.48 Changes of irradiance corresponding to the mesh size (13:24 PM)

Mesh length	Irradiance (W/m^2)
225	1077.88
240	1112.12
255	956.53
270	1013.79
285	994.8
300	1031.23
315	999.09
330	887.95
345	1097.87
360	980.865
375	1037.89
Minimum	887.95
Mean	1017.274091
Maximum	1112.12
Std. Deviation	62.06

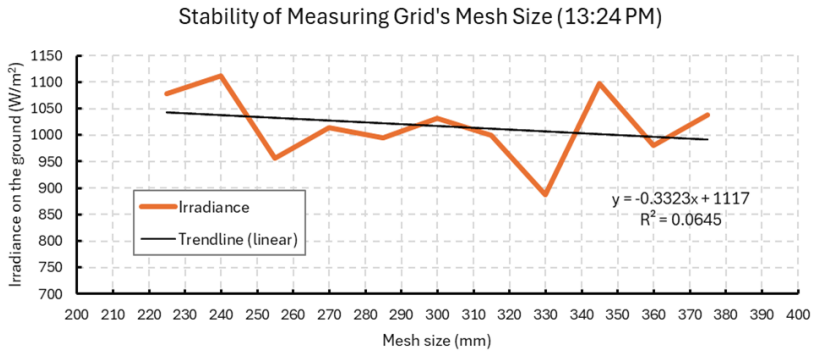

Figure 5.49 Fluctuation of irradiance corresponding to the mesh size (13:24 PM)

5.4.6. Application on Another Building

To further prove that the script works for any given building in which the Rhino model is available, the solar convergence replication of the 20 Fenchurch St "Walkie Talkie" building was done. Due to the limited access to the accurate 3D model of the building itself, two types of models were remade: Walkie Talkie building with one way curved front façade (indicated with 0 Gaussian curvature) and Walkie Talkie building with two way curved synclastic façade (indicated with Gaussian curvature > 0) as can be seen in Figure 5.50.

The similar simulation conducted by Zhu, Jahn, and Rein in 2019 will be used as the basis of information input and for comparison. From the paper, it is known that the façade is solar coated with double glazing and assumed to have low emissivity film layer on the glass. From the same paper, the calculated REE is found to be 27% after calculating it in accordance to the BSI Standards EN:410, 2011. Geometrically, the shape of the front façade itself is similar to that of a parabolic

mirror, the albedo value taken from the environment is 0.1, and lastly, the day in which the simulation is run through is in 29 August 2013 from 10:45 to 15:45 local time (Zhu et al., 2019).

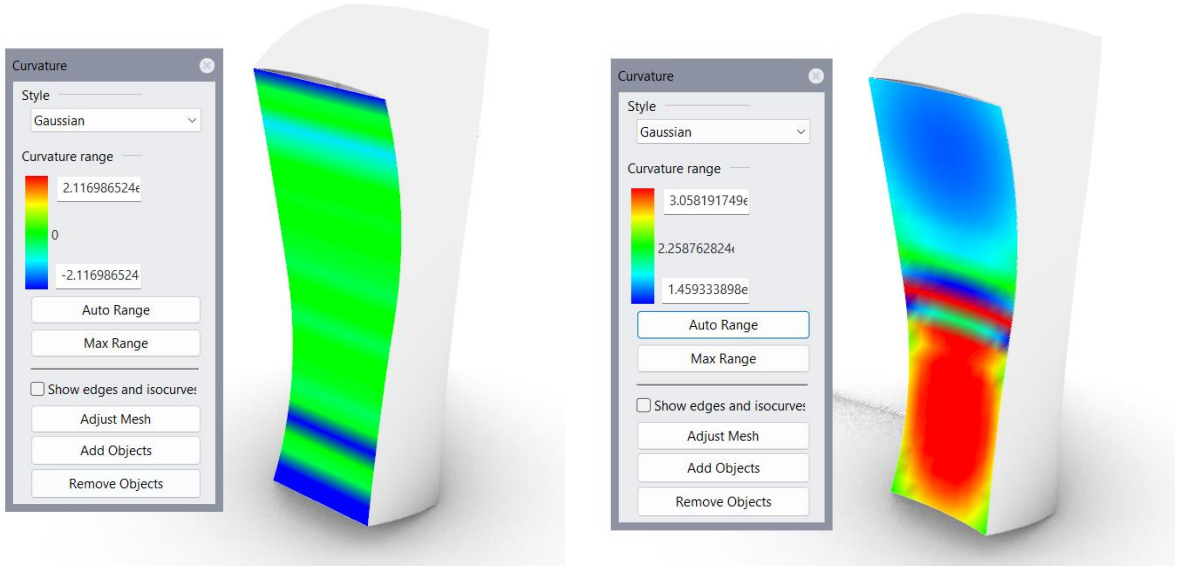

(a) (b)

Figure 5.50 Two remakes of the Walkie Talkie buildings: (a) monocurvature (b) synclastic double curvature

It is important to note that in this simulation, the Reindl model is employed, meaning that the worst case scenarios are expected to happen. The result from the program for the monocurvature building and the synclastic double curved building is shown in Figure 5.51 and Figure 5.52, respectively.

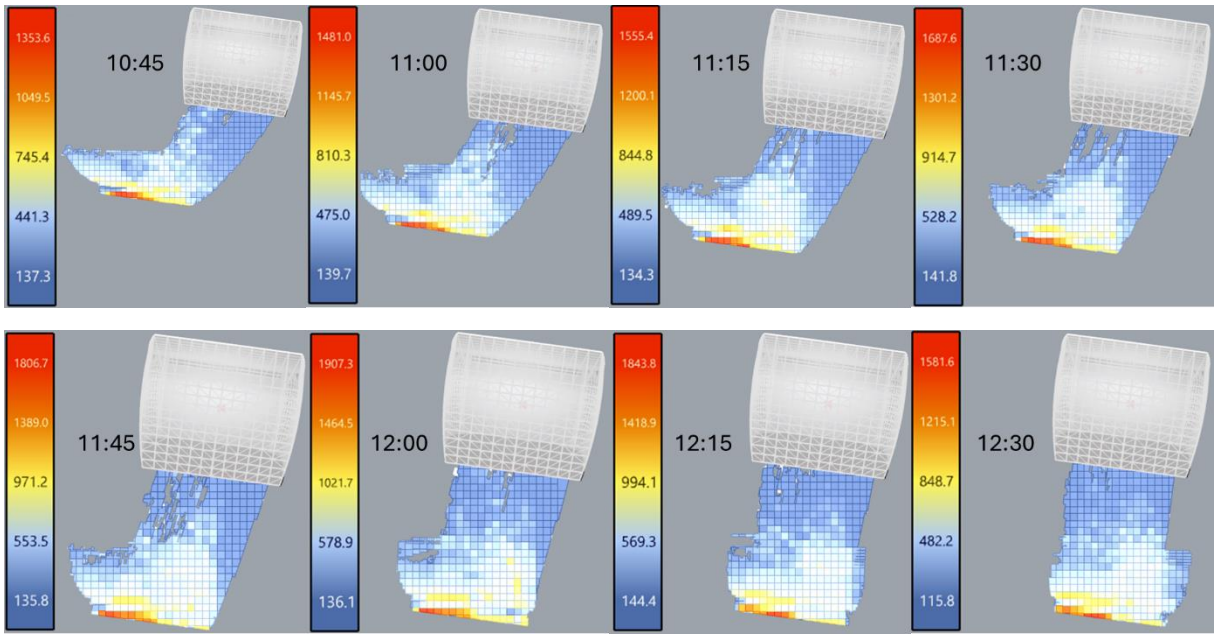

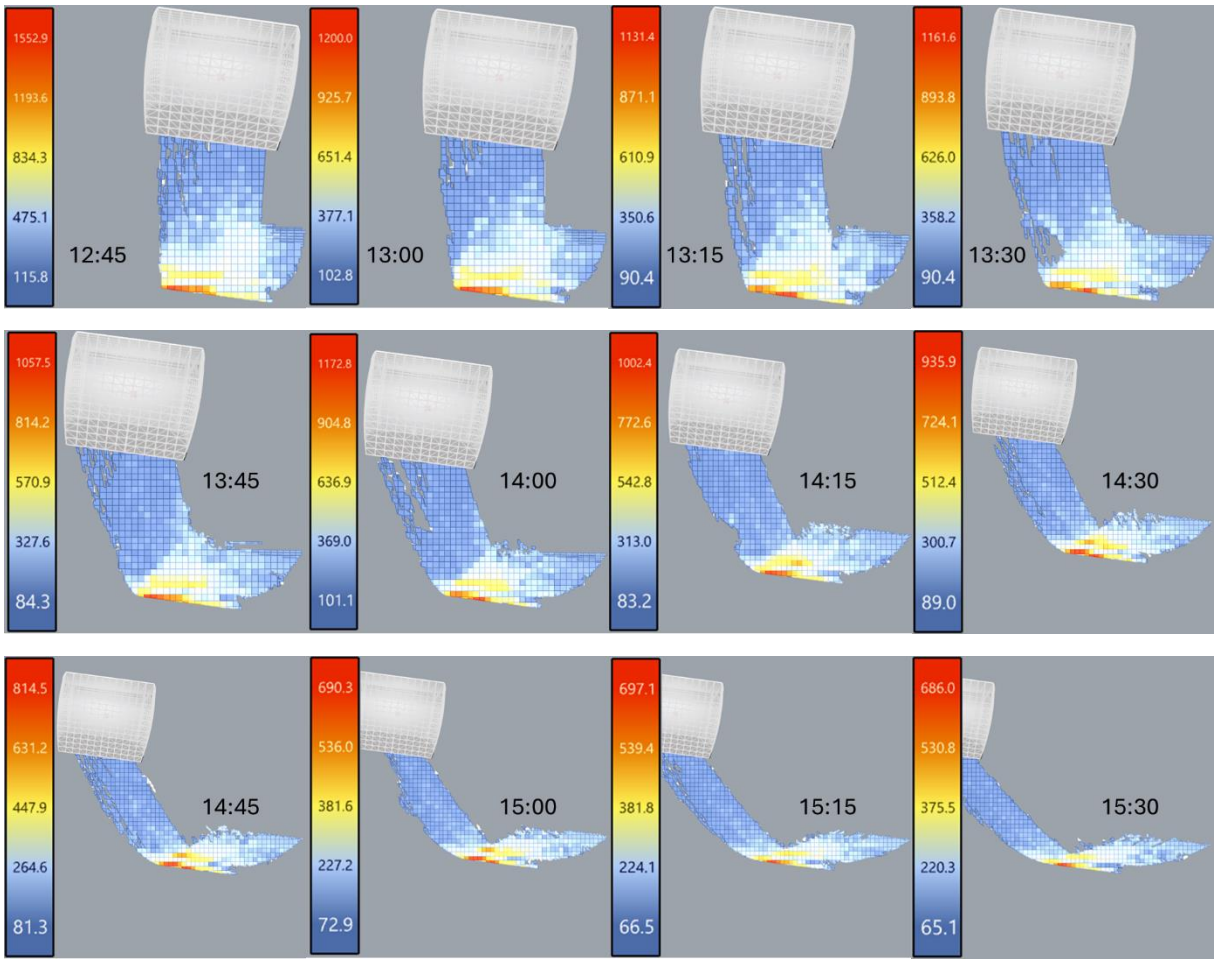

Figure 5.51 Irradiance prediction for 29th of August 2013 for monocurvature façade

The irradiance measured at ground level without any obstructions for both geometries is compiled in Figure 5.53. It is found that the highest irradiance for the monoclastic front façade is 1907.3 W/m^2, which occurs at 12:00. Meanwhile, for a synclastic front façade, the maximum irradiance at the focal point can reach 6270.7 W/m^2. The latter case is significantly higher than what was predicted by Zhu et al., who estimated a maximum irradiance of 3320 W/m^2 occurring at the rooftop of 20 Eastcheap, near the Fenchurch Street. In conclusion, the correct detail of the geometry being studied, along with the buildings in the vicinity that act as both blockages and the landing surface for the reflected rays, plays an important role in obtaining accurate results of solar irradiance on the ground. Additionally, although cloud conditions was taken into account, the paper by Zhu et al. did not consider the effects of anisotropy in the sky and the nonlinear reflectance rate of the glass façade, which can explain the significant discrepancy between the results.

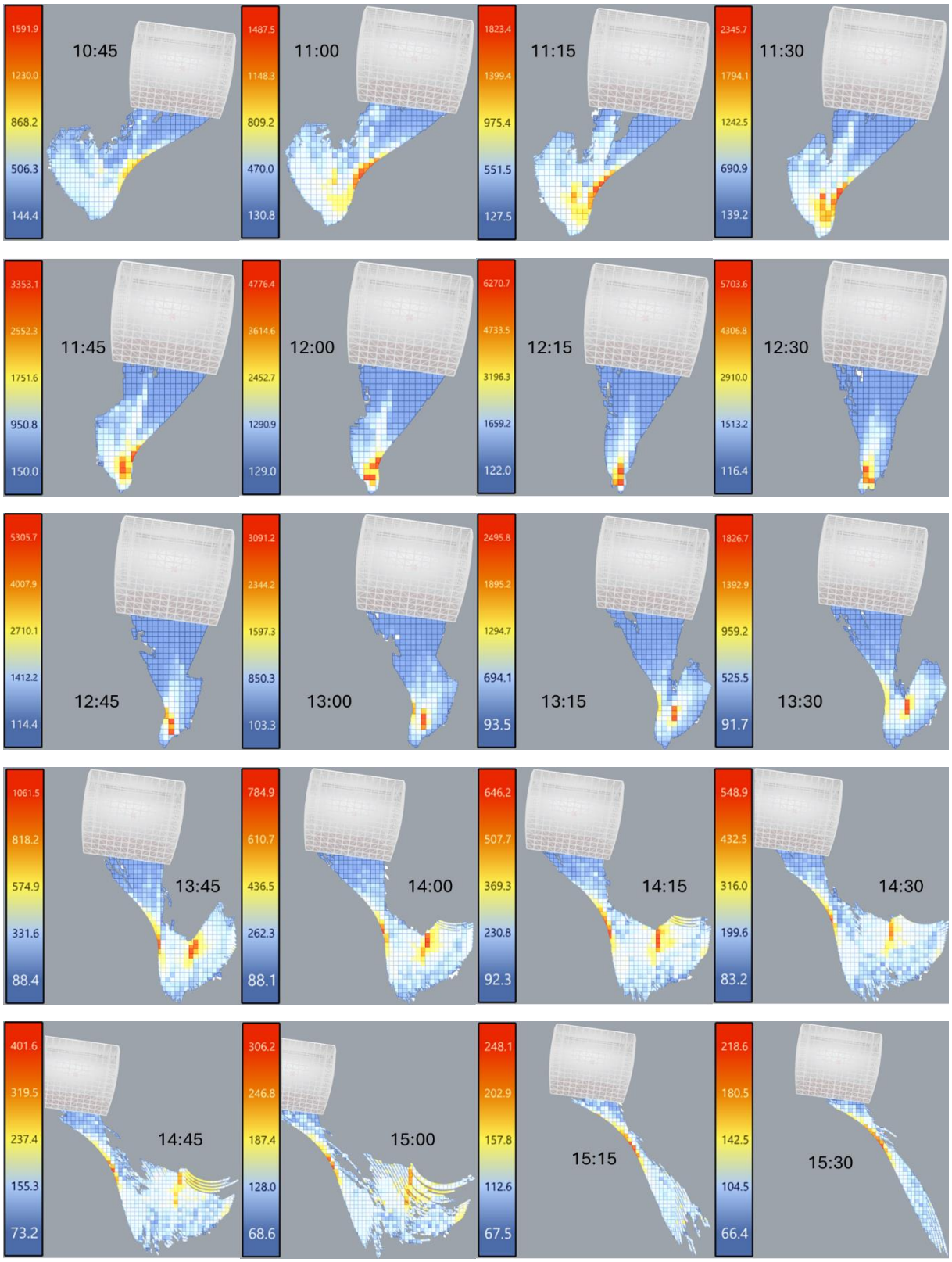

Figure 5.52 Irradiance prediction for 29th of August 2013 for synclastic façade

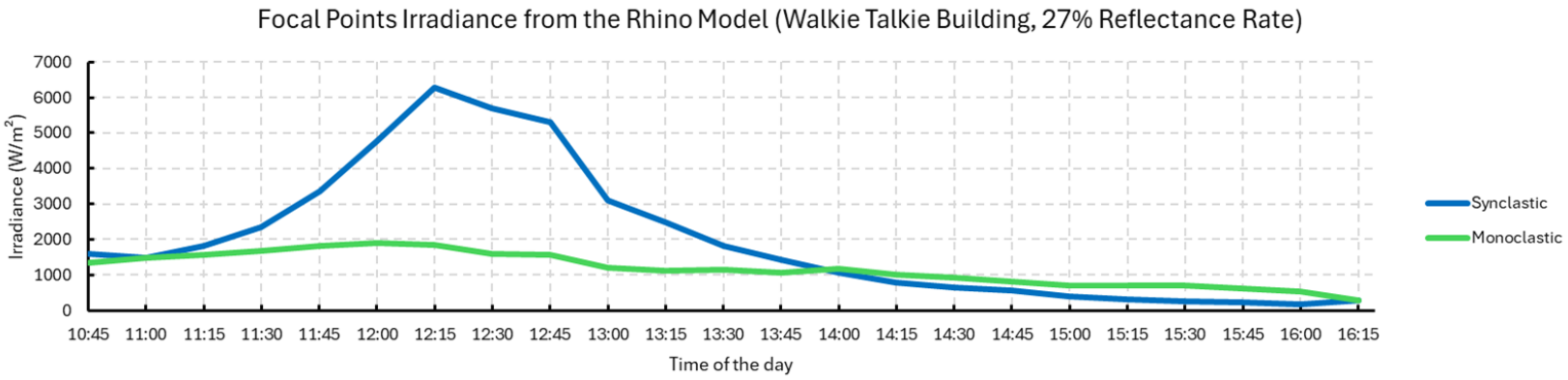

Figure 5.53 Focal points irradiance from the Rhino model (Walkie Talkie Building, 27% reflectance rate), 29th August 2013

6 | Conclusions and Recommendations

In this chapter, conclusions regarding the outcomes of the thesis are compiled, and recommendations for further work are laid out. This thesis started with exploring the behavior of several types of two-dimensional mirrors concerning the intensity of the created focal points. After that, the possibility of creating an algorithm using Grasshopper script as the virtual programming language to recreate the solar convergence phenomenon in the Amsterdam University Medical Center and the 20 Fenchurch St "Walkie Talkie" building has been explored. Solar measurement data collected on 8 March 2024 in the parking lot of Amsterdam UMC was used to calibrate the model. In this thesis, the lesser-known effective reflectance rate of façades due to differences in refractive indices of air and glass, and the effect of the anisotropic skies on the intensity of the solar convergence, have been automated into the algorithm.

6.1. Conclusion

This subchapter answers the subquestions and the main research question which have been written in Chapter 1. The answers are derived from the findings in Chapter 5 Results and Discussion

SRQ1: What are the parameters that cause the problem of converged solar reflection, and how can a model be developed to capture the physics behind the phenomenon?

To avoid the converged solar reflection phenomenon from a curved façade, building practitioners must consider a sufficient number of parameters that influence the severity of the problem, as this issue primarily arises from a combination of unwise design choices and does not occur instantly. In particular, it is important for architects and engineers to have an imagination to break down the problem step-by-step correctly. Starting by understanding the behavior of focal point intensity in a two-dimensional world as was described in Chapter 5.4 will be one of the easiest approaches to consider.

a. **Concave Quarter-circle mirror**

   This type of mirror will intensify the focal point if the energy/solar rays are shot at angles between 5 degrees and 25 degrees from the optical axis. Within that range, the intensity of the focal point is approximately 1.2 times (which can go up to 1.25 times) the intensity of the quarter-circle mirror at a 0-degree angle from the optical axis. Between 25 to 50 degrees, the intensity reduces linearly from 1.25 to 0.15. After 50 degrees, the intensity reduces to less than 10%.

b. **Concave Half-circle mirror**

   Under the same denominator as previously (the intensity of the focal point of the quarter-circle mirror at a 0-degree angle from the optical axis), this type of mirror, if it has the same arc length as the quarter-circle mirror, will only converge up to 0.6 times at 45 and 70 degree angles from the optical axis. Between 70 and 90 degrees, the intensity reduces linearly from 0.6 to 0.1. For the rest of the angles, the intensity will average around 0.55 times.

c. **Concave Half-elliptical mirror symmetric to the minor axis**
   Under the same denominator and arc length, this type of mirror will have a steady intensity of around 0.38 under angles ranging from 0 to 70 degrees. The intensity increases to 0.45 at an angle of 75 degrees and then reduces linearly from 0.45 to 0.075 between 75 degrees and 90 degrees.
d. **Concave Half-elliptical mirror symmetric to the major axis**
   Under the same denominator and arc length, the intensity of the focal point of this type of mirror will fluctuate between 0.45 and 0.3 at angles from 0 degrees to 65 degrees. Above 65 degrees, the intensity will decrease linearly until it reaches 0.05 at a 90-degree angle.
e. **Concave quarter elliptical mirror**
   This type of mirror will have the worst effect when the light rays shine on the mirror parallel to the longitudinal direction, and under the same arc length, the intensity will be the same as that of the quarter-circle mirror at a 0-degree angle from the optical axis.
f. **Concave parabolic mirror**
   Under the same denominator and arc length, this type of mirror is the worst cross-section an architect can choose for the shape of the façade because it can concentrate the focal point up to 5 times the intensity of the focal point of a quarter-circle mirror. It happens when the rays are shot parallel to the optical axis. However, if the angle is tilted even just 20 degrees, then the intensity goes down to 11.7% and practically diminish afterwards
g. **Concave hyperbolic mirror**
   Just like parabolic mirror, the most intensive focal point happens at an angle of 0 degrees from optical axis. However, under the same denominator and arc length, the intensity is only 0.4 than that of a quarter circle mirror. And it will reduce to 0.025 from 0 degree angle to 40 degree angle.

In the case of the Amsterdam UMC building, which can be approximated as a quarter-circle mirror, the peak irradiance of solar reflection on the parking lot occurs when the solar azimuth is at 147.37 and 139.59 degrees from the north, corresponding to angles from the optical axis of 15.24 and 23.04 degrees, respectively. This indicates a strong connection between the intensity of the focal point in the 2D model and the 3D model.

Without understanding the parameters above, knowing the effective reflectance rate from Fresnel's equation or simulating the model using anisotropy in the sky will not suffice. However, those are the next steps to model the solar convergence phenomenon accurately.

Another parameter to consider when studying converged solar reflection is that the reflectance rate of glass façades is not linear and changes as a function of the angle of incidence and the refractive indices between the two materials at the interface, as described by Fresnel's equation. However, for practicality, engineers and architects can approximate the function very accurately using parabolic or circular arc functions based on the normal effective reflectance and omit the refractive index parameter. By applying the boundary conditions mentioned in the paper, the replication of these functions yields coefficients of determination well above 0.961 for the four types of glass being checked, indicating negligible discrepancies between the actual function and the replication.

By considering the anisotropy parameters in the sky (horizon brightening, circumsolar diffuse radiation, and reflection from the ground), higher peaks of solar convergence have been obtained.

After all the parameters are known, the model in this thesis was fundamentally developed with the primary concept of transferring solar power from the sky to the ground, as shown in Figure 4.20 and extensively discussed in the Chapter on Methodology.

SRQ2: What constitutes the acceptable limits for both human safety (e.g., sunburn) and temperature-related problems (e.g., melting objects)? And do the simulation results reflect this concerning irradiation?

As mentioned earlier in Chapter 3.10, several objects that could potentially be located at the focal points are assessed in terms of how well they handle heat flux. Both the Amsterdam UMC building and the "Walkie Talkie" have concerning levels of irradiation from the solar convergence phenomenon. For the Amsterdam UMC building, simulations recorded heat flux above 2500 W/m^2 occurring from 11:00 to 11:15, around 12:15, and from 14:30 to 15:30, totaling approximately 1.5 hours of harmful heat flux. This level of irradiation, as noted last year, melted the body of a car but is not sufficient to ignite a fire if, for example, pieces of wood were lying at the focal point. However, this irradiation can induce cracks in wired glass, as their limit for cracking is around 2000 W/m^2. Furthermore, considering that people in the parking lot would not expect to get sunburned, the short-term exposure limit for human skin should be around 1500 W/m^2, as stated by Danks et al. (Danks et al., 2016a). Consequently, throughout the day, the heat will cause a nuisance and temporary visual impairment for drivers entering and exiting the Amsterdam UMC building complex from approximately 10:45 to 15:37.

For the "Walkie Talkie," before the façade was improved to mitigate the problem, the solar convergence issue was much worse than that of the UMC building. Zhu predicted that the focal point during the day of simulation could reach as high as 3320 W/m^2 (Zhu et al., 2019). However, from the simpler model used in this thesis, under the same plane where all reflection rays can converge, considering the anisotropy of the sky and the nonlinear changes in the reflection rate, an irradiance of 6271 W/m^2 can be reached. Both of these levels are dangerous for human skin, as evidenced by several goods in a nearby store and several bike saddles being scorched to melting.

SRQ3: What is the expected error of the developed model compared to the measured data?

For the case of the Amsterdam UMC building, there are indeed discrepancies between the highest peak values of focal point irradiance between the on-site measurement and the three anisotropic sky models. The highest peak value from the measurement was recorded to be around 4833.65 W/m^2, occurring at approximately 14:35 local time. Meanwhile, the highest peak values of irradiance from the isotropic and three anisotropic sky models (Klucher, Hay-Davies, and Reindl) at 14:45 were recorded to be 3689, 3875, 4147, and 4184 W/m^2, respectively. The differences between the irradiance of the measurement and the 3D model are 23.68%, 19.83%, 14.21%, and 13.44%, with the Reindl sky model providing the closest estimation to the measured data.

SRQ4: What is the effect of input uncertainties?

In this thesis, not all uncertainties are investigated, except for systematic uncertainties such as the effect of mismatch (incompatibility) in curvature between the façade and the glass panels, and the effect of setting different measuring mesh sizes on the result of irradiance at ground level. Random errors, such as random bulges in the glass panels caused by differences in air pressure in the cavity of the façade system, which create less flat or flatter surfaces, are neglected due to the limited time to test if such defects exist and to what extent these "bulges" from air pressure differences occur.

The effect of mismatched glass panel curvatures was investigated. While each glass panel should have had a radius of 24.6 m, a radius of 22.0 m was installed instead, possibly to match the façade on the west side of the building and to simplify the casting process. This incompatibility resulted in the reflection shapes being jaggier at the edges and showing more apparent focal lines. One thing to note is that the shape of the reflection is reciprocal to the intensity of the irradiation. In this case, the effect of curvature incompatibility caused the focal points to increase by 23.52% at one time and decrease by 13.09% at another time, compared to if the mismatch did not exist. Therefore, even though the increase in intensity is significant due to the mismatch, there is no strong tendency for the resulting irradiance to be consistently higher or lower compared to a situation without this mismatch in curvature.

Other than the effect from the uncertainty in the physical model, uncertainty due to the setting of the numerical model, in this case, the setting of the size of the measuring mesh was also investigated. The simulation was run at two different locations and epochs with different mesh sizes increasing from 225×225 mm^2 to 375×375 mm^2. The irradiance readings fluctuate from one mesh size to the next, but there is no evidence showing a trend where the irradiance increases as the mesh of the measuring plane gets smaller, or vice versa. Therefore, it is safe to say that the algorithm will not diverge into unstable conditions when choosing different sizes of meshes.

However, at the same time, it is also not possible for the current algorithm to suggest that the irradiance values from the model are very accurate because the ratio between the highest and lowest irradiance values from the two epochs and locations when the mesh sizes are changed is consistently around 1.25. Further study needs to be done with this algorithm to understand if there is a logical error in building the model.

6.2. Recommendations

6.2.1. Recommendations for Building Practitioners

To avoid the converged solar reflection phenomenon from a curved façade, one must consider a sufficient number of parameters that influence the severity of the problem, as this issue primarily arises from a combination of unwise design choices and does not occur instantly. In particular, it is important for architects and engineers to have an imagination to break down the problem step-by-step correctly.

From Chapter 5.3 of this thesis, architects and building engineers need to first understand the relationship between optics and the geometry of the façade of the building they are designing. A working hypothesis from this thesis is that understanding the changes in the intensity of the focal point of the reflected irradiation in a two-dimensional world is a good starting point.

After understanding the behavior described above from simple 2D geometry, architects and building engineers need to consider their building as if it will act as a mirror. They need to be aware of the shape their building will form when a horizontal cross-section is cut through it, asking questions such as “What type of curve will the façade make? Will it create a half-circle cross section? Or hyperbolic? Or other shapes?” Additionally, architects need to translate and adjust the local axis system of this "mirror" to the geographic position of the building (global axis system). This is crucial to avoid aligning the angle at which the maximum intensity of the focal point will occur with the solar azimuth where the highest beam normal irradiance will strike during a certain time of the year.

If the building's façade has double-curvature, a vertical cross-section should also be considered. Designers need to ask similar questions about the curve created. In this case, designers can make decisions about the shape of the vertical cross-section to avoid high-intensity focal points under certain angles from the optical axis converge at the ground level or within 1.5 to 2.0 meters above the ground level (typical chest height for a pedestrian or face height of a seated driver).

As a rule of thumb, try to avoid creating a façade that will form a parabolic cross-section, either in the horizontal or vertical direction. Generally, try to do the opposite of what good antenna makers or opticians would do. There is a reason why parabolic antennas and telescopes are popular, whereas hyperboloid or half-ellipsoidal antennas or telescopes are much less common. The reason is simple: as stated in the previous chapter, when collimated rays hit the parabolic cross-section parallel to the optical axis, regardless of whether the incoming light or signal falls within the cross-section, it all focuses into a single point.

The second worst choice is to create a façade with a circular cross-section. Although a circular cross-section does not converge rays as effectively as a parabolic cross-section, it functions similarly to omnidirectional antennas: it can receive rays or signals from all directions and reflect them adequately in multiple directions. But the severity from the façade with this type of cross section relies on how big is the façade and the central angle of the circle defining the arc.

At the same time, however, categorizing the intensity of the irradiance from solar reflection solely based on the dimensions or area of the façade is tricky. For example, the Walkie Talkie building has an area of at least 7,264 m^2, while the southern façade of Amsterdam UMC has an area of only

106.59 m^2 (the Walkie Talkie façade area is 68 times larger than that of the Amsterdam UMC's). However, the maximum irradiance for both cases from this paper is 6,270 W/m^2 and 4,183.6 W/m^2, respectively (the converged solar irradiance from the Walkie Talkie building is 1.5 times greater than that of the Amsterdam UMC's). This occurs because the problem is not just a matter of façade area, although it plays a role; the parameters are simply much more complex.

From this thesis, it was also confirmed that the isotropic sky model is not suitable for checking the worst-case conditions of converged solar reflection as it assumes all parts of the sky dome have the same intensity of radiation, which is not the case. Especially during a very sunny day with a clearness index close to 1, it is clear that around the circumference of the sun disk, the radiation from the sun should be brighter.

Therefore, the author firmly believes that architects, engineers, and building practitioners need to spend some time studying Solar Energy Engineering or work closely with photovoltaic experts, climate scientists, urban planners, etc., to unravel the problem because there are many more fundamental or underlying principles by interdisciplinary experts.

6.2.2. Recommendations for Future Research

Some of the recommendations the author suggests to improve the understanding of the solar convergence phenomenon for future research are:

1. Creation of a script or method that accommodates the solar rays being projected onto the façade and ground as areas, not as lines/rays. This will ensure a uniform distribution of solar and reflection power on the ground, yielding more accurate readings when converted into irradiation.
2. Creation of a script or method to convert the irradiation that falls onto the ground into temperature by considering the duration of irradiation, environmental conditions, and the thermal material properties of the surface on which the irradiation falls.
3. Creation of a script or method that can automatically generate the mesh centered at the highest focal point to avoid the possibility of overscaling or underscaling from incorrectly placing or sizing the mesh. In this algorithm, the mesh location is stationary and predetermined by discretizing the overall shape of the reflection.
4. Creation of a script or method that can automatically generate finer mesh in the critical coordinates (e.g., focal point, focal lines) and larger mesh further away from it to reduce the computational time.
5. Creation of guidelines that consider not only the shape of the façade acting as a mirror in 2D cross-section but also mirrors in the 3D world, including synclastic, anticlastic, and monoclastic shapes.
6. Consideration of the effects of random errors in the placement of glass façades, and the effect of random bulges/random curvature due to varying cavity pressure of the façade system on the intensity of the solar convergence phenomenon.

Bibliography

3rdFlix. (2021, April 14). *Light—Practically Study Material*. https://www.practically.com/studymaterial/blog/docs/class-8th/physics/light/

ABC News. (2010, September 27). *Vegas Hotel Pool 'Death Ray' Burns Tourists*. ABC News. https://abcnews.go.com/Travel/las-vegas-hotel-pool-sunlight-swimming-tourists/story?id=11739234

Acharya, T., Riehl, B., & Fuchs, A. (2021). Effects of Albedo and Thermal Inertia on Pavement Surface Temperatures with Convective Boundary Conditions—A CFD Study. *Processes*, *9*(11), Article 11. https://doi.org/10.3390/pr9112078

Ågren, A. R. (2024, January 1). *Properties of softwood*. Swedish Wood. https://www.swedishwood.com/wood-facts/about-wood/from-log-to-plank/properties-of-softwood/

booking.com. (2024, July 23). *StripViewSuites at Vdara, Las Vegas, USA*. Booking.Com. https://www.booking.com/hotel/us/stripviewsuites-at-vdara-las-vegas12.html

Borgart, A. (2023, May 10). *Spatial Structures—Structural Geometry*. Delft University of Technology. https://brightspace.tudelft.nl/d2l/le/content/594953/viewContent/3658492/View

Brembilla, E. (2023, May 10). *Fundamentals of Daylight Design*. Delft University of Technology. https://brightspace.tudelft.nl/d2l/le/content/594953/viewContent/3656847/View

Brzezicki, M. (2012). The Influence of Reflected Solar Glare Caused by the Glass Cladding of a Building: Application of Caustic Curve Analysis. *Computer-Aided Civil and Infrastructure Engineering*, *27*(5), 347–357. https://doi.org/10.1111/j.1467-8667.2011.00751.x

CAMS Radiation Service. (2020, February 6). *CAMS solar radiation time-series*. CAMS Solar Radiation Time-Series. https://ads.atmosphere.copernicus.eu/cdsapp#!/dataset/cams-solar-radiation-timeseries?tab=overview

CAMS Radiation Service. (2024, May 27). *CAMS radiation service—SoDa*. https://www.soda-pro.com/web-services/radiation/cams-radiation-service

Danks, R., Good, J., & Sinclair, R. (2016a). Assessing reflected sunlight from building facades: A literature review and proposed criteria. *Building and Environment*, *103*, 193–202. https://doi.org/10.1016/j.buildenv.2016.04.017

Danks, R., Good, J., & Sinclair, R. (2016b). *Avoiding The Dreaded Death Ray: Controlling Facade Reflections Through Purposeful Design*.

Dasari, H. P., Desamsetti, S., Langodan, S., Attada, R., Kunchala, R. K., Viswanadhapalli, Y., Knio, O., & Hoteit, I. (2019). High-resolution assessment of solar energy resources over the Arabian Peninsula. *Applied Energy*, *248*, 354–371. https://doi.org/10.1016/j.apenergy.2019.04.105

DeKay, M., & Brown, G. Z. (2013). *Sun, Wind, and Light: Architectural Design Strategies*. John Wiley & Sons.

Dereniak, E. L., & Dereniak, T. D. (2008). *Geometrical and Trigonometric Optics*. Cambridge University Press. https://doi.org/10.1017/CBO9780511755637

Dincer, I., Colpan, C. O., Kizilkan, O., & Ezan, M. A. (Eds.). (2015). *Progress in Clean Energy, Volume 2: Novel Systems and Applications*. Springer International Publishing. https://doi.org/10.1007/978-3-319-17031-2

Enomoto, A., Uede, K., & Wakamatsu, T. (1999). An Experimental Study on Glass Cracking and Fallout by Radiant Heat Exposure. *International Association for Fire Safety Science*, *6*, 1063–1074.

Federal Aviation Administration. (2021, May 11). *Federal Aviation Administration Policy: Review of Solar Energy System Projects on Federally-Obligated Airports*. Federal Register. https://www.federalregister.gov/documents/2021/05/11/2021-09862/federal-aviation-administration-policy-review-of-solar-energy-system-projects-on-federally-obligated

Ferreol, R. (2017, January 1). *Dupin indicatrix*. https://mathcurve.com/surfaces.gb/indicatricededupin/indicatricededupin.shtml

Garfield, L. (2015, March 28). *The 'death ray hotel' burning Las Vegas visitors came up with a simple fix*. Business Insider. https://www.businessinsider.com/the-vdara-death-ray-hotel-is-still-burning-people-in-las-vegas-2016-6

Google Earth. (2022, February 6). https://earth.google.com/web/@52.29524945,4.95744937,1.6590324a,98.40396313d,35y,13.70718205h,49.0062441t,0r/data=MikKJwolCiExakZQNTBMMkliYWZzV0tORzVnSVc2UUxlWV9WMFdfUG0gAToDCgEw

Gurupira, T. (2018). *EVALUATION AND OPTIMISATION OF PHOTOVOLTAIC (PV) PLANT DESIGNS*.

Hess, M., & Koepke, P. (2008). Modelling UV irradiances on arbitrarily oriented surfaces: Effects of sky obstructions. *Atmospheric Chemistry and Physics*, *8*(13), 3583–3591. https://doi.org/10.5194/acp-8-3583-2008

Janssen, C. (2023, June 8). *CIEM5250 LU-1 The Sun (B5 Building Engineering Module)*. Delft University of Technology. https://brightspace.tudelft.nl/d2l/le/content/594953/viewContent/3445074/View

Kalogirou, S. A. (2009). Chapter two—Environmental Characteristics. In S. A. Kalogirou (Ed.), *Solar Energy Engineering* (pp. 49–762). Academic Press. https://doi.org/10.1016/B978-0-12-374501-9.00002-9

Klucher, T. M. (1978). *Evaluation of Models to Predict Insolation on Tilted Surfaces*. NASA.

Kuhn, J. R., Bush, R. I., Scheick, X., & Scherrer, P. (1998). The Sun's shape and brightness. *Nature*, *392*(6672), 155–157. https://doi.org/10.1038/32361

Lawrence Berkeley National Laboratory. (2023, June 10). *IGDB Release Notes*. https://windows.lbl.gov/sites/default/files/software/IGDB/IGDBReleaseNotes-92.htm

Ling, S. J., Sanny, J., & Moebs, W. (2016). *Spherical Mirrors*. *3*. https://pressbooks.online.ucf.edu/osuniversityphysics3/chapter/spherical-mirrors/

Liu, B. Y. H., & Jordan, R. C. (1960). The interrelationship and characteristic distribution of direct, diffuse and total solar radiation. *Solar Energy*, *4*(3), 1–19. https://doi.org/10.1016/0038-092X(60)90062-1

Liu, J., & Zhang, W. (2015). The Influence of the Environment and Clothing on Human Exposure to Ultraviolet Light. *PLOS ONE*, *10*(4), e0124758. https://doi.org/10.1371/journal.pone.0124758

LSI LASTEM. (2024a, January 1). E-Log. *LSI LASTEM*. https://www.lsi-lastem.com/products/data-loggers/e-log/

LSI LASTEM. (2024b, January 1). Global solar radiation. *LSI LASTEM*. https://www.lsi-lastem.com/products/meteorological-sensors/solar-radiation/global-solar-radiation/

Martínez-Rubio, A., Sanz-Adan, F., Santamaría-Peña, J., & Martínez, A. (2016). Evaluating solar irradiance over facades in high building cities, based on LiDAR technology. *Applied Energy*, *183*, 133–147. https://doi.org/10.1016/j.apenergy.2016.08.163

MINES ParisTech / Vaisala. (2024, January 1). *Decomposition models*. SoDa. https://www.soda-pro.com

NASA Science Mission Directorate. (2010, January 1). *Visible Light—NASA Science*. Visible Light. https://science.nasa.gov/ems/09_visiblelight/

National Aeronautics and Space Administration. (2018, July 26). *Solar Irradiance | Sun Climate*. https://sunclimate.gsfc.nasa.gov/article/solar-irradiance

National Service Center for Environmental Publications (NSCEP). (2008, May 28). *Handbook of Chemical Hazard Analysis Procedures (Includes Computer Disk)*. Handbook of Chemical Hazard Analysis Procedures (Includes Computer Disk). https://nepis.epa.gov/Exe/ZyNET.exe/10003MK5.txt?ZyActionD=ZyDocument&Client=EPA&Index=1986%20Thru%201990&Docs=&Query=&Time=&EndTime=&SearchMethod=1&TocRestrict=n&Toc=&TocEntry=&QField=&QFieldYear=&QFieldMonth=&QFieldDay=&UseQField=&IntQFieldOp=0&ExtQFieldOp=0&XmlQuery=&File=D%3A%5CZYFILES%5CINDEX%20DATA%5C86THRU90%5CTXT%5C00000003%5C10003MK5.txt&User=ANONYMOUS&Password=anonymous&SortMethod=h%7C-&MaximumDocuments=1&FuzzyDegree=0&ImageQuality=r75g8/r75g8/x150y150g16/i425&Display=hpfr&DefSeekPage=x&SearchBack=ZyActionL&Back=ZyActionS&BackDesc=Results%20page&MaximumPages=1&ZyEntry=1&slide

NOAA Earth System Research Laboratories. (2024, May 28). *DOY Calendar*. https://www.esrl.noaa.gov/gmd/grad/neubrew/Calendar.jsp

Ourraoui, I., & Ahaitouf, A. (2022). Investigation of the feasibility and potential use of sun tracking solutions for concentrated photovoltaic Case study Fez Morocco. *Energy Reports*, *8*, 1412–1425. https://doi.org/10.1016/j.egyr.2022.08.071

Ravenscroft, T. (2013, September 4). In pictures: Crowds gather to feel Walkie Talkie 'death rays'. *The Architects' Journal*. https://www.architectsjournal.co.uk/archive/in-pictures-crowds-gather-to-feel-walkie-talkie-death-rays

SAMSUNG. (2021, January 1). *Samsung Galaxy A72 | Samsung Latin*. Samsung Latin_en. https://www.samsung.com/latin_en/smartphones/galaxy-a/galaxy-a72-awesome-black-128gb-sm-a725mzkacgu/

Schipper, H. R., & Brembilla, E. (2023). Bundeling van zonlicht door gekromde gevels: Een concreet probleemgeval onderzocht met parametrische tools, simulatie en controlemetingen. *Bouwfysica Blad*, *1*(34). https://repository.tudelft.nl/islandora/object/uuid%3A2b463d3e-1c40-4ccc-9d18-38ba4f2a6254

Schipper, R., hordijk, truus, Turrin, M., mureau, michou, Fransen, E., & Rhijn, A. (2018). Parametrisch-geometrische modellen voor beoordeling van zonreflecties en andere bouwfysica-vraagstukken. *Bouwfysica*, *29*.

Shilston, R., & Danks, R. (2018, April 12). *Simulation of urban solar reflections and their impact on building performance*.

Spearpoint, M. J., & Quintiere, J. G. (2000). Predicting the burning of wood using an integral model. *Combustion and Flame*, *123*(3), 308–325. https://doi.org/10.1016/S0010-2180(00)00162-0

Speroni, A., Mainini, A. G., Zani, A., Paolini, R., Pagnacco, T., & Poli, T. (2022). Experimental Assessment of the Reflection of Solar Radiation from Façades of Tall Buildings to the Pedestrian Level. *Sustainability*, *14*(10), Article 10. https://doi.org/10.3390/su14105781

Stewart, J. (2012). *Calculus: Early transcendentals*. Cengage Learning. https://thuvienso.hoasen.edu.vn/handle/123456789/8936

The British Standard Institution. (2021, January 31). *Application of fire safety engineering principles to the design of buildings—Probabilistic risk assessment*. https://knowledge.bsigroup.com/products/application-of-fire-safety-engineering-principles-to-the-design-of-buildings-probabilistic-risk-assessment-1?version=standard&tab=preview

The Globe Program. (2024, January 1). *Cloud Cover*. Cloud Cover. https://www.globe.gov/web/s-cool/home/observation-and-reporting/observing-cloud-cover

The Grimes Teacher (Director). (2023, August 29). *Waves—Reflection & Mirrors—Intro & Laws* [Video recording]. https://www.youtube.com/watch?app=desktop&v=j0ut7iylNcg&ab_channel=TheGrimesTeacher

University of Oregon Solar Radiation Monitoring Laboratory: Sun chart program. (2024, April 9). http://solardata.uoregon.edu/SunChartProgram.php

van Bommel, W. (2019). Luminaires. In W. van Bommel (Ed.), *Interior Lighting: Fundamentals, Technology and Application* (pp. 329–350). Springer International Publishing. https://doi.org/10.1007/978-3-030-17195-7_13

Wainwright, O. (2013, September 4). Walkie Talkie developers build screen to stop 'death ray'. *The Guardian*. https://www.theguardian.com/artanddesign/2013/sep/04/walkie-talkie-screen-death-ray

Weather Underground. (2024, March 8). *Schiphol, Netherlands Weather History | Weather Underground*. https://www.wunderground.com/history/daily/nl/schiphol/EHAM/date/2024-3-8

Wen, J., Wong, N. H., Ignatius, M., & Chen, X. (2020). Impacts of Highly Reflective Building Façade on the Thermal and Visual Environment of an Office Building in Singapore. In R. Roggema & A. Roggema (Eds.), *Smart and Sustainable Cities and Buildings* (pp. 467–478). Springer International Publishing. https://doi.org/10.1007/978-3-030-37635-2_33

Zhu, J., Jahn, W., & Rein, G. (2019). Computer simulation of sunlight concentration due to façade shape: Application to the 2013 Death Ray at Fenchurch Street, London. *Journal of Building Performance Simulation*, *12*(4), 378–387. https://doi.org/10.1080/19401493.2018.1538389

Appendix A

No.	Authors	Year of Publication	Title	Methodology	Keywords	Limitation	Conclusion
1	Roel Schipper, Eleonora Brembilla	2023	Bundeling van Zonlicht Door Gekromde Gevels (H. R. Schipper & Brembilla, 2023)	Built a numerical model using parametric tools and software for insolation simulation, then compared and calibrated the model with real-world measurements.	-	The model only takes into account perfectly cylindrical (single) curved double glazing units without any error in placement, and there is only one model. Other possible deviations, such as those from double-glazing materials, are outside the scope.	During peak moments, the calculation model underestimated the result by 300-500 W/m² compared to the real model, due to changes in façade specifications for economic feasibility without advance knowledge of the risks
2	Alberto Speroni, Andrea Giovanni Mainini, Andrea Zani, Riccardo Paolini, Tommaso Pagnacco, Tiziana Poli	2022	Experimental Assessment of the Reflection of Solar Radiation from Façades of Tall Buildings to the Pedestrian Level (Speroni et al., 2022)	Experiment measured sunlight reflection from 3 x 1:100 scale models mimicking typical tall buildings with varying facades: classic vertical, 10% tilted, and curved concave. Used diverse finishing materials showcasing extremes in reflectance properties: Specular surfaces for high incidence solar angles and light-diffusing materials for plaster finishing	Reflective materials, mitigation, urban heat island, outdoor comfort, visual comfort, heat stress, optimization, skyscrapers	The prototypes are made of highly specular non-planar (perfectly curved) façade without randomness factor or imperfection	The tool for preliminary assessment of solar reflectance risks in generic complex building shapes is stated from all 3 prototypes, caustic curve formation is the source of high irradiance in the street level. Despite the materials used, in high solar angle of incident, façade behaviour becomes similar to that of 100% specular
3	Jianxiu Wen, Nyuk Hien Wong, Marcel Ignatius	2020	Impacts of Highly Reflective Building Façade on the Thermal and Visual Environment of an Office Building in Singapore (Wen et al., 2020)	Comparative study based on data collected from the on-site measurement	Reflective building façade, reflected sunlight, thermal performance, visual performance	The researchers did not make any models or prototype. But their approach in considering weather conditions could be used as an insight	Weather condition plays a vital role in both in indoor thermal and in visual environment of the impacted building. Affected area directly facing the reflective façade experienced the worst effect

No.	Authors	Year of Publication	Title	Methodology	Keywords	Limitation	Conclusion
4.	Jiajie Zhu, Wolfram Jahn, Guillermo Rein	2019	Computer Simulation of Sunlight Concentration due to Façade Shape: Application to the 2013 Death Ray at Frenchurch Street, London (Zhu et al., 2019)	Created a representative geometry numerical model of the Walkie Talkie building and its immediate vicinity. Taking into account the corresponding weather situations in the location at a certain season	Glare, lighting simulations, sunlight, urban environment	Limited information regarding the geometry model and surface parameters of the façade (reflectivity of double glazing façade, etc)	An extensive overview of how much irradiance was transferred to the ground on the 29th of August 2013, where the incident of plastic parts on a nearby parked car was melted
5.	Ruth Shilston, Ryan Danks	2018	Simulation of urban solar reflections and their impact on building performance (Shilston & Danks, 2018)	Reviewed two case studies: 1) Focused reflections from a concave façade 2) Reflections from concave façades in a dense urban location, using a custom simulation tool. The primary object of study is high-performance glazing system with low emissivity coatings	Solar, glare, reflected heat, glazing, simulation	Unique features such as details on the façade are omitted	The authors emphasize that a simulation results are as good as its input data, thus having good understanding of assumptions and limitations are crucial.
6.	Roel Schipper, Truus Hordijk, Michela Turrin, Michou Mureau, Edward Fransen, Arthur van Rhijn	2018	Parametrisch-geometrische modellen voor beoordeling van zonreflecties en andere bouwfysica-vraagstukken (R. Schipper et al., 2018)	Introduce using Grasshopper as parametric and graphical programming language to assess the reflection of the Walkie Talkie building	-	Reflection properties of the façade is assumed constant and no error in placement or randomness factor is taken into consideration	The paper validated the reliability of modelling such problems with Rhino-GH, but extensive cases to push the limit of the worst-case scenario are yet to be done

No.	Authors	Year of Publication	Title	Methodology	Keywords	Limitation	Conclusion
7.	Ryan Danks, Joel Good, Ray Sinclair	2016	Assessing reflected sunlight from building facades: A literature review and proposed criteria (Danks et al., 2016a)	Review of existing regulations and metrics related to the impact of visible light and thermal energy on people and property. Provide quantitative criteria	Glare, solar reflection, built environment, regulation, façade performance	The literature on which the criteria are based is still limited in breadth. Schematization of the façade is limited to only one model	The proposed criteria has been made and the author believe it is suitable for both the design purposes and post-construction assessment. Some of the criteria is based on interpretation on sparse research and author's opinion and experience
8.	Ryan Danks, Joel Good, Ray Sinclair	2016	Avoiding the Dreaded Death Ray Controlling façade reflections through purposeful design (Danks et al., 2016b)	Providing the practical ways to mitigate solar reflectance by showcasing the already implemented method such as surface modification, applying anti-reflective coating, obstructing the reflections using mashrabiya, sudare, brise-soleil, and vertical mullions	Façade, glare, computational design, design processes, glass, education	The issue of limited tools available in which they require steep learning curves to model solar convergence is understood but solution was not found	Different materials of the façade, façade form, and surface area of the façade are some of the most prominent parameters that dictate the temperature increase due to the solar convergence phenomenon. By understanding these parameters, costly planned mitigation can be avoided
9.	Marcin Brzezicki	2012	The Influence of Reflected Solar Glare Caused by the Glass Cladding of a Building: Application of Caustic Curve Analysis	The study investigates the effects of glare reflection from different glossy facades (rectangular, angular, concave, convex) in a two-stage approach. The second stage focuses on concave facades, using mathematical analysis and custom software to analyze caustic curves and geometrical conditions.	-	The study assumes uniform sunlight intensity and does not account for factors like cloud coverage or exact temperature increases due to glare. It also cannot predict the glare intensity in W/m^2 accurately and instead uses a new unit called multiplicative factor (MF) and reflection glare area (RGA)	Designers can use the findings to avoid caustic curve formation or predict its position, thereby preventing glare-related hazards in building surroundings. The study provides intuitive tools and simple mathematical formulas to estimate glare effects based on facade geometry.

Appendix B

Below is the GHPython Script code snippet to measure the irradiance on ground level

```
"""Provides a scripting component.
    Inputs:
        x: The x script variable
        y: The y script variable
    Output:
        a: The a output variable"""

__author__ = "satri"
__version__ = "2024.03.29"

import Rhino.Geometry as rg
import rhinoscriptsyntax as rs
from scriptcontext import *
import Rhino
import System.Collections.Generic as scg
import System as s
import ghpythonlib.treehelpers as th

# Assuming 'fragments' is a list of Brep geometries representing fragments
# and 'lines' is a list of LineCurve geometries representing lines
# tolerance is the intersection tolerance, which could be the document's absolute
tolerance

def check_intersections(fragments, lines):
    intersection_tree = []

    for i, fragment in enumerate(fragments):
        intersecting_lines_indices = []

        for j, line in enumerate(lines):
            # Ensure line is a curve for intersection
            if not isinstance(line, rg.Curve):
                line = line.ToNurbsCurve()

            # Check for intersection
            intersection = rs.CurveBrepIntersect(line, fragment)

            if intersection:  # If there is an intersection
                intersecting_lines_indices.append(j)

        # If no intersections found for this fragment, use None as placeholder
        if not intersecting_lines_indices:
            intersecting_lines_indices = [None]

        intersection_tree.append(intersecting_lines_indices)

    return intersection_tree

# Flatten the inputs if they are trees
# flat_fragments = flatten_tree_input(fragments)
# flat_lines = flatten_tree_input(lines)

# Call the intersection check function
intersection_results = check_intersections(fragments, lines)
```

Appendix C

Below is the GHPython Script code snippet to show the irradiance at arbitrary location on the ground

```
"""Provides a scripting component.
    Inputs:
        x: The x script variable
        y: The y script variable
    Output:
        a: The a output variable"""

__author__ = "satri"
__version__ = "2024.03.29"

import Rhino

#retrieve the currently active Rhino document
active_doc = Rhino.RhinoDoc.ActiveDoc

#create a new instance of the TextEntity class and set its attributes
txt = Rhino.Geometry.TextEntity()

#set attributes
txt.FontIndex = Rhino.RhinoDoc.ActiveDoc.Fonts.FindOrCreate(TextFont, FontOptions[0], FontOp-
tions[1])
txt.Text = InputText
txt.Plane = TextPlane
txt.TextHeight = TextHeight

#decompose the text entity into curves
txtCrvs = txt.Explode()

#assign the curves to the output variable
a = txtCrvs
```

Appendix D

Calumen

SAINT-GOBAIN

66.2 FT (14 Argon 90) 66.2 FT

Coating: COOL-LITE SKN 165 II #4

Computed by: Satria Galih Nugraha Computed on: 15/05/2024 Product catalog: Netherlands Norms: EN410 (2011-04)

Glazing type

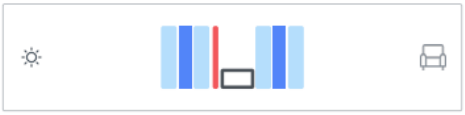

Glazing 1
PLANICLEAR (6mm) - Tempered
PVB STANDARD (0.76mm)
PLANICLEAR (6mm) - Tempered
COOL-LITE SKN 165 II

Cavity 1
Argon 90% 14 mm

Glazing 2
PLANICLEAR (6mm) - Tempered
PVB STANDARD (0.76mm)
PLANICLEAR (6mm) - Tempered

Simulated performance datas

Luminous Factors	**CIE (15-2004)**
Light Transmittance (TL)	58%
Outdoor Reflectance (RLe)	16%
Indoor Reflectance (RLi)	18%
Energy Factors	**EN410 (2011-04)**
Transmittance (TE)	27%
Outdoor Reflectance (Ree)	25%
Indoor Reflectance (Rei)	30%
Absorptance A1 (AE1)	45%
Absorptance A2 (AE2)	2%
Solar Factors	**EN410 (2011-04)**
Solar Factor (g)	0.31
Shading Coefficient (SC)	0.36
Thermal Transmission	**EN673-2011**
Ug	1.0 W/(m2.K)
Angle relative to the vertical	0°
Acoustics	**EN 12758**
Acoustic simulated values	
Rw (C;Ctr)	40 (-1; -6) dB
Ra	39 dB
Ra,tr	34 dB
STC (ASTM E413)	41
OITC (ASTM E1332)	32
Color Rendering	**CIE (15-2004)**
Transmission (Ra)	91.2
Reflection (Ra)	82.3
Safety Class	**EN 12600**
Pendulum Body Resistance	1B1/1B1
Anti-Burglary	**EN 356**
Burglar Resistance	P2A/P2A
Manufacturing Sizes	
Nominal Thickness	39.5 mm
Weight	62 kg/m²
Sustainability	
Carbon footprint	
The value is calculated regarding the composition computed based on the standard EN 15804+A2 (2019)	
Global Warming Potential (GWP) – A1-A3	**EN 15804+A2 (2019)**
(kg, CO_2 eq./m²) European average	111

Appendix E

Angle of incidence	WINDOW data AMC Glass	WINDOW data CLEAR GLASS 6 mm	WINDOW data SOLARBAN 70XL	WINDOW data PLANICLEAR 6 mm
0	0.376	0.07	0.507	0.075
1	0.3756	0.07	0.5066	0.075
2	0.3752	0.07	0.5062	0.075
3	0.3748	0.07	0.5058	0.075
4	0.3744	0.07	0.5054	0.075
5	0.374	0.07	0.505	0.075
6	0.3736	0.07	0.5046	0.075
7	0.3732	0.07	0.5042	0.075
8	0.3728	0.07	0.5038	0.075
9	0.3724	0.07	0.5034	0.075
10	0.372	0.07	0.503	0.075
11	0.3718	0.07	0.5029	0.075
12	0.3716	0.07	0.5028	0.075
13	0.3714	0.07	0.5027	0.075
14	0.3712	0.07	0.5026	0.075
15	0.371	0.07	0.5025	0.075
16	0.3708	0.07	0.5024	0.075
17	0.3706	0.07	0.5023	0.075
18	0.3704	0.07	0.5022	0.075
19	0.3702	0.07	0.5021	0.075
20	0.37	0.07	0.502	0.075
21	0.37	0.0702	0.5022	0.0752
22	0.37	0.0704	0.5024	0.0754
23	0.37	0.0706	0.5026	0.0756
24	0.37	0.0708	0.5028	0.0758
25	0.37	0.071	0.503	0.076
26	0.37	0.0712	0.5032	0.0762
27	0.37	0.0714	0.5034	0.0764
28	0.37	0.0716	0.5036	0.0766
29	0.37	0.0718	0.5038	0.0768
30	0.37	0.072	0.504	0.077
31	0.3706	0.0725	0.5045	0.0776
32	0.3712	0.073	0.505	0.0782
33	0.3718	0.0735	0.5055	0.0788
34	0.3724	0.074	0.506	0.0794
35	0.373	0.0745	0.5065	0.08
36	0.3736	0.075	0.507	0.0806
37	0.3742	0.0755	0.5075	0.0812

38	0.3748	0.076	0.508	0.0818
39	0.3754	0.0765	0.5085	0.0824
40	0.376	0.077	0.509	0.083
41	0.3776	0.0786	0.51	0.0847
42	0.3792	0.0802	0.511	0.0864
43	0.3808	0.0818	0.512	0.0881
44	0.3824	0.0834	0.513	0.0898
45	0.384	0.085	0.514	0.0915
46	0.3856	0.0866	0.515	0.0932
47	0.3872	0.0882	0.516	0.0949
48	0.3888	0.0898	0.517	0.0966
49	0.3904	0.0914	0.518	0.0983
50	0.392	0.093	0.519	0.1
51	0.3956	0.0971	0.5208	0.1044
52	0.3992	0.1012	0.5226	0.1088
53	0.4028	0.1053	0.5244	0.1132
54	0.4064	0.1094	0.5262	0.1176
55	0.41	0.1135	0.528	0.122
56	0.4136	0.1176	0.5298	0.1264
57	0.4172	0.1217	0.5316	0.1308
58	0.4208	0.1258	0.5334	0.1352
59	0.4244	0.1299	0.5352	0.1396
60	0.428	0.134	0.537	0.144
61	0.4362	0.1445	0.5417	0.1552
62	0.4444	0.155	0.5464	0.1664
63	0.4526	0.1655	0.5511	0.1776
64	0.4608	0.176	0.5558	0.1888
65	0.469	0.1865	0.5605	0.2
66	0.4772	0.197	0.5652	0.2112
67	0.4854	0.2075	0.5699	0.2224
68	0.4936	0.218	0.5746	0.2336
69	0.5018	0.2285	0.5793	0.2448
70	0.51	0.239	0.584	0.256
71	0.5265	0.2635	0.5967	0.2815
72	0.543	0.288	0.6094	0.307
73	0.5595	0.3125	0.6221	0.3325
74	0.576	0.337	0.6348	0.358
75	0.5925	0.3615	0.6475	0.3835
76	0.609	0.386	0.6602	0.409
77	0.6255	0.4105	0.6729	0.4345
78	0.642	0.435	0.6856	0.46
79	0.6585	0.4595	0.6983	0.4855
80	0.675	0.484	0.711	0.511

81	0.7075	0.5356	0.7399	0.5599
82	0.74	0.5872	0.7688	0.6088
83	0.7725	0.6388	0.7977	0.6577
84	0.805	0.6904	0.8266	0.7066
85	0.8375	0.742	0.8555	0.7555
86	0.87	0.7936	0.8844	0.8044
87	0.9025	0.8452	0.9133	0.8533
88	0.935	0.8968	0.9422	0.9022
89	0.9675	0.9484	0.9711	0.9511
90	1	1	1	1
Average	0.467010989	0.200824176	0.571192308	0.210137363

Angle of incidence	Replicated data AMC Glass	Replicated data CLEAR GLASS 6 mm	Replicated data SOLARBAN 70XL	Replicated data PLANICLEAR 6 mm
0	0.376	0.072	0.504	0.077
1	0.376	0.072	0.504	0.077
2	0.376	0.072	0.504	0.077
3	0.376	0.072	0.504	0.077
4	0.376	0.072	0.504	0.077
5	0.376	0.072	0.504	0.077
6	0.376	0.072	0.504	0.077
7	0.376	0.072	0.504	0.077
8	0.376	0.072	0.504	0.077
9	0.376	0.072	0.504	0.077
10	0.376	0.072	0.504	0.077
11	0.376	0.072	0.504	0.077
12	0.376	0.072	0.504	0.077
13	0.376	0.072	0.504	0.077
14	0.376	0.072	0.504	0.077
15	0.376	0.072	0.504	0.077
16	0.376	0.072	0.504	0.077
17	0.376	0.072	0.504	0.077
18	0.376	0.072	0.504	0.077
19	0.376	0.072	0.504	0.077
20	0.376	0.072	0.504	0.077
21	0.376	0.072	0.504	0.077
22	0.376	0.072	0.504	0.077
23	0.376	0.072	0.504	0.077
24	0.376	0.072	0.504	0.077
25	0.376	0.072	0.504	0.077
26	0.376	0.072	0.504	0.077
27	0.376	0.072	0.504	0.077
28	0.376	0.072	0.504	0.077
29	0.376	0.072	0.504	0.077
30	0.376	0.072	0.504	0.077
31	0.376	0.072	0.504	0.077
32	0.376	0.072	0.504	0.077
33	0.376	0.072	0.504	0.077
34	0.376	0.072	0.504	0.077
35	0.376	0.072	0.504	0.077
36	0.376	0.072	0.504	0.077
37	0.376	0.072	0.504	0.077
38	0.376	0.072	0.504	0.077
39	0.376	0.072	0.504	0.077
40	0.376	0.072	0.504	0.077

41	0.376	0.072	0.504	0.077
42	0.376	0.072	0.504	0.077
43	0.376	0.072	0.504	0.077
44	0.376	0.072	0.504	0.077
45	0.376	0.072	0.504	0.077
46	0.376	0.072	0.504	0.077
47	0.376	0.072	0.504	0.077
48	0.376	0.072	0.504	0.077
49	0.376	0.072	0.504	0.077
50	0.376	0.072	0.504	0.077
51	0.37639	0.07258	0.50431	0.077577
52	0.37756	0.074319	0.50524	0.079306
53	0.37951	0.077217	0.50679	0.082189
54	0.38224	0.081275	0.508959	0.086225
55	0.38575	0.086492	0.511749	0.091414
56	0.39004	0.092869	0.515158	0.097757
57	0.39511	0.100405	0.519188	0.105252
58	0.40096	0.109101	0.523837	0.113901
59	0.40759	0.118956	0.529106	0.123703
60	0.415	0.129971	0.534996	0.134659
61	0.42319	0.142145	0.541505	0.146768
62	0.43216	0.155479	0.548634	0.16003
63	0.44191	0.169973	0.556383	0.174445
64	0.45244	0.185626	0.564752	0.190015
65	0.46375	0.20244	0.573741	0.206738
66	0.47584	0.220413	0.58335	0.224614
67	0.48871	0.239546	0.593579	0.243644
68	0.50236	0.259839	0.604428	0.263828
69	0.51679	0.281293	0.615897	0.285166
70	0.532	0.303906	0.627986	0.307658
71	0.54799	0.32768	0.640695	0.331304
72	0.56476	0.352615	0.654024	0.356104
73	0.58231	0.378709	0.667973	0.382058
74	0.60064	0.405965	0.682542	0.409167
75	0.61975	0.434381	0.697732	0.43743
76	0.63964	0.463958	0.713541	0.466848
77	0.66031	0.494696	0.729971	0.49742
78	0.68176	0.526595	0.747021	0.529147
79	0.70399	0.559655	0.764691	0.562029
80	0.727	0.593877	0.782981	0.596067
81	0.75079	0.62926	0.801892	0.631259
82	0.77536	0.665805	0.821422	0.667607
83	0.80071	0.703511	0.841573	0.70511

84	0.82684	0.74238	0.862345	0.743769
85	0.85375	0.78241	0.883736	0.783584
86	0.88144	0.823603	0.905748	0.824554
87	0.90991	0.865958	0.928381	0.866681
88	0.93916	0.909476	0.951633	0.909964
89	0.96919	0.954157	0.975506	0.954404
90	1	1	1	1

SS_{tot} AMC Glass	SS_{tot} CLEAR GLASS 6 mm	SS_{tot} SOLARBAN 70XL	SS_{tot} PLANICLEAR 6mm
0.0083	0.0171	0.0041	0.0183
0.0084	0.0171	0.0042	0.0183
0.0084	0.0171	0.0042	0.0183
0.0085	0.0171	0.0043	0.0183
0.0086	0.0171	0.0043	0.0183
0.0087	0.0171	0.0044	0.0183
0.0087	0.0171	0.0044	0.0183
0.0088	0.0171	0.0045	0.0183
0.0089	0.0171	0.0045	0.0183
0.0090	0.0171	0.0046	0.0183
0.0090	0.0171	0.0047	0.0183
0.0091	0.0171	0.0047	0.0183
0.0091	0.0171	0.0047	0.0183
0.0091	0.0171	0.0047	0.0183
0.0092	0.0171	0.0047	0.0183
0.0092	0.0171	0.0047	0.0183
0.0093	0.0171	0.0047	0.0183
0.0093	0.0171	0.0047	0.0183
0.0093	0.0171	0.0048	0.0183
0.0094	0.0171	0.0048	0.0183
0.0094	0.0171	0.0048	0.0183
0.0094	0.0171	0.0048	0.0182
0.0094	0.0170	0.0047	0.0182
0.0094	0.0170	0.0047	0.0181
0.0094	0.0169	0.0047	0.0180
0.0094	0.0169	0.0047	0.0180
0.0094	0.0168	0.0046	0.0179
0.0094	0.0168	0.0046	0.0179
0.0094	0.0167	0.0046	0.0178
0.0094	0.0166	0.0045	0.0178
0.0094	0.0166	0.0045	0.0177
0.0093	0.0165	0.0044	0.0176
0.0092	0.0163	0.0044	0.0174
0.0091	0.0162	0.0043	0.0172
0.0090	0.0161	0.0043	0.0171
0.0088	0.0160	0.0042	0.0169
0.0087	0.0158	0.0041	0.0168
0.0086	0.0157	0.0041	0.0166
0.0085	0.0156	0.0040	0.0165
0.0084	0.0155	0.0039	0.0163
0.0083	0.0153	0.0039	0.0162

0.0080	0.0149	0.0037	0.0157
0.0077	0.0146	0.0036	0.0153
0.0074	0.0142	0.0035	0.0149
0.0072	0.0138	0.0034	0.0145
0.0069	0.0134	0.0033	0.0141
0.0066	0.0130	0.0032	0.0137
0.0064	0.0127	0.0030	0.0133
0.0061	0.0123	0.0029	0.0129
0.0059	0.0120	0.0028	0.0125
0.0056	0.0116	0.0027	0.0121
0.0051	0.0108	0.0025	0.0112
0.0046	0.0099	0.0024	0.0103
0.0041	0.0091	0.0022	0.0094
0.0037	0.0084	0.0020	0.0086
0.0033	0.0076	0.0019	0.0078
0.0029	0.0069	0.0017	0.0070
0.0025	0.0063	0.0016	0.0063
0.0021	0.0056	0.0014	0.0056
0.0018	0.0050	0.0013	0.0050
0.0015	0.0045	0.0012	0.0044
0.0009	0.0032	0.0009	0.0030
0.0005	0.0021	0.0006	0.0019
0.0002	0.0012	0.0004	0.0011
0.0000	0.0006	0.0002	0.0005
0.0000	0.0002	0.0001	0.0001
0.0001	0.0000	0.0000	0.0000
0.0003	0.0000	0.0000	0.0002
0.0007	0.0003	0.0000	0.0006
0.0012	0.0008	0.0001	0.0012
0.0018	0.0015	0.0002	0.0021
0.0035	0.0039	0.0007	0.0051
0.0058	0.0076	0.0015	0.0094
0.0086	0.0125	0.0026	0.0150
0.0119	0.0185	0.0040	0.0219
0.0157	0.0258	0.0058	0.0301
0.0202	0.0343	0.0079	0.0395
0.0251	0.0440	0.0103	0.0503
0.0306	0.0548	0.0131	0.0624
0.0367	0.0669	0.0162	0.0758
0.0433	0.0802	0.0195	0.0905
0.0578	0.1121	0.0285	0.1223
0.0745	0.1493	0.0390	0.1589
0.0933	0.1918	0.0513	0.2003

0.1142	0.2397	0.0652	0.2465
0.1373	0.2929	0.0808	0.2974
0.1624	0.3514	0.0981	0.3531
0.1897	0.4152	0.1170	0.4137
0.2190	0.4844	0.1376	0.4790
0.2505	0.5589	0.1599	0.5490
0.2841	0.6387	0.1839	0.6239
2.2589	4.6859	1.2792	4.8019

SS_{res} AMC Glass	SS_{res} CLEAR GLASS 6 mm	SS_{res} SOLARBAN 70XL	SS_{res} PLANICLEAR 6mm
0	4E-06	9E-06	4E-06
1.6E-07	4E-06	6.76E-06	4E-06
6.4E-07	4E-06	4.84E-06	4E-06
1.44E-06	4E-06	3.24E-06	4E-06
2.56E-06	4E-06	1.96E-06	4E-06
4E-06	4E-06	0.000001	4E-06
5.76E-06	4E-06	3.6E-07	4E-06
7.84E-06	4E-06	4E-08	4E-06
1.02E-05	4E-06	4E-08	4E-06
1.3E-05	4E-06	3.6E-07	4E-06
1.6E-05	4E-06	0.000001	4E-06
1.76E-05	4E-06	1.21E-06	4E-06
1.94E-05	4E-06	1.44E-06	4E-06
2.12E-05	4E-06	1.69E-06	4E-06
2.3E-05	4E-06	1.96E-06	4E-06
0.000025	4E-06	2.25E-06	4E-06
2.7E-05	4E-06	2.56E-06	4E-06
2.92E-05	4E-06	2.89E-06	4E-06
3.14E-05	4E-06	3.24E-06	4E-06
3.36E-05	4E-06	3.61E-06	4E-06
3.6E-05	4E-06	4E-06	4E-06
3.6E-05	3.24E-06	3.24E-06	3.24E-06
3.6E-05	2.56E-06	2.56E-06	2.56E-06
3.6E-05	1.96E-06	1.96E-06	1.96E-06
3.6E-05	1.44E-06	1.44E-06	1.44E-06
3.6E-05	0.000001	0.000001	0.000001
3.6E-05	6.4E-07	6.4E-07	6.4E-07
3.6E-05	3.6E-07	3.6E-07	3.6E-07
3.6E-05	1.6E-07	1.6E-07	1.6E-07
3.6E-05	4E-08	4E-08	4E-08
3.6E-05	1.93E-34	0	0
2.92E-05	2.5E-07	2.5E-07	3.6E-07
2.3E-05	0.000001	0.000001	1.44E-06
1.76E-05	2.25E-06	2.25E-06	3.24E-06
1.3E-05	4E-06	4E-06	5.76E-06
9E-06	6.25E-06	6.25E-06	9E-06
5.76E-06	9E-06	9E-06	1.3E-05
3.24E-06	1.23E-05	1.22E-05	1.76E-05
1.44E-06	1.6E-05	0.000016	2.3E-05
3.6E-07	2.03E-05	2.03E-05	2.92E-05
0	0.000025	0.000025	3.6E-05

2.56E-06	4.36E-05	3.6E-05	5.93E-05
1.02E-05	6.72E-05	4.9E-05	8.84E-05
2.3E-05	9.6E-05	6.4E-05	0.000123
4.1E-05	0.00013	8.1E-05	0.000164
6.4E-05	0.000169	0.0001	0.00021
9.22E-05	0.000213	0.000121	0.000262
0.000125	0.000262	0.000144	0.00032
0.000164	0.000317	0.000169	0.000384
0.000207	0.000376	0.000196	0.000454
0.000256	0.000441	0.000225	0.000529
0.000369	0.000601	0.000272	0.000719
0.000468	0.000723	0.000301	0.00087
0.000542	0.000789	0.00031	0.000962
0.000584	0.000791	0.000297	0.000984
0.000588	0.000729	0.000264	0.000936
0.000555	0.000612	0.000214	0.00082
0.000488	0.000453	0.000154	0.000653
0.000394	0.000279	9.15E-05	0.000454
0.000283	0.00012	3.71E-05	0.000253
0.000169	1.62E-05	4.02E-06	8.73E-05
0.000169	5.55E-06	3.8E-08	7.11E-05
0.00015	2.29E-07	4.99E-06	4.06E-05
0.000114	2E-05	2.79E-05	9.95E-06
6.99E-05	9.27E-05	8.01E-05	1.48E-06
2.76E-05	0.000254	0.000175	4.54E-05
1.85E-06	0.000548	0.000329	0.00018
1.1E-05	0.001027	0.000561	0.000451
7.67E-05	0.001751	0.00089	0.000914
0.000225	0.002787	0.001339	0.001629
0.000484	0.004213	0.001935	0.002669
0.000462	0.004119	0.001936	0.00248
0.000473	0.004175	0.001991	0.002411
0.00052	0.004384	0.002104	0.002456
0.000607	0.004756	0.002279	0.002618
0.000743	0.005312	0.002523	0.002908
0.000939	0.006077	0.002845	0.003346
0.001212	0.007089	0.003257	0.003959
0.001581	0.00839	0.003773	0.004781
0.002069	0.010031	0.004408	0.005857
0.002704	0.012073	0.005181	0.007236
0.001874	0.008772	0.003843	0.005092
0.00125	0.006179	0.002769	0.003458
0.000796	0.004188	0.001925	0.002248

0.000477	0.002702	0.001278	0.001382
0.000264	0.001633	0.000797	0.000789
0.000131	0.0009	0.000456	0.000406
5.49E-05	0.000431	0.000227	0.000179
1.73E-05	0.000161	8.9E-05	6.03E-05
2.86E-06	3.31E-05	1.94E-05	1.09E-05
0	0	0	0
0.02371867	0.109523329	0.050333148	0.06725473

Appendix F

Recorded irradiation from the 3D Model on Amsterdam UMC building simulating the day of measurement took place: 8th March 2024

Timestamp	Irradiation (W/m^2)			
	Isotropic	Klucher	Hay-Davies	Reindl
10:47:00	2144.9	2239	2444.6	2463.3
11:00:00	2355.6	2452.2	2663.4	2683.7
11:15:00	2360	2481.8	2684.9	2705.1
11:30:00	1893.8	1994.8	2148.8	2164.8
11:45:00	2143.8	2235.5	2397	2415
12:00:00	1922.3	1992.2	2128.3	2144.3
12:15:00	2387	2481.7	2648.1	2668.3
12:30:00	2086.3	2167	2307.7	2325.4
12:45:00	1925.9	1971.6	2093.8	2110.2
13:00:00	2026.2	2025.9	2145.7	2163.3
13:15:00	2042.6	2099.8	2228	2245.7
13:30:00	1852.2	1885.5	1998.2	2014.2
13:45:00	1991.1	2038.6	2161.7	2179.3
14:00:00	1914.8	2004.9	2132.7	2150.1
14:15:00	1853.8	1943.8	2070.2	2087.3
14:30:00	2779.9	2920.9	3119.9	3146.9
14:45:00	3688.9	3874.7	4146.7	4183.6
15:00:00	3349.7	3552.6	3812	3846.6
15:15:00	3572.7	3785.8	4068.1	4105.3
15:30:00	3101.8	3298.9	3546.7	3578.8
15:45:00	1089	1169.4	1256.6	1267.6
16:00:00	475	511.4	547.7	552.3
16:10:00	256	273.9	291.5	293.8

Recorded irradiance from the 3D model on 20 Fenchurch St "The Walkie Talkie" building simulating the day of death-ray happened: 29th August 2024

Timestamp	Irradiance from Reindl sky model (W/m^2)	
	Monoclastic	Synclastic
10:47:00	1591.9	1591.9
11:00:00	1487.5	1487.5
11:15:00	1823.4	1823.4
11:30:00	2345.7	2345.7
11:45:00	3353.1	3353.1
12:00:00	4776.4	4776.4
12:15:00	6270.7	6270.7
12:30:00	5703.6	5703.6
12:45:00	5305.7	5305.7
13:00:00	3091.2	3091.2
13:15:00	2495.8	2495.8
13:30:00	1826.7	1826.7
13:45:00	1418.8	1418.8
14:00:00	1061.5	1061.5
14:15:00	784.9	784.9
14:30:00	646.2	646.2
14:45:00	548.9	548.9
15:00:00	401.6	401.6
15:15:00	306.2	306.2
15:30:00	248.1	248.1
15:45:00	218.6	218.6
16:00:00	157.7	157.7
16:10:00	276.5	276.5